

**The importance of Low-Mass Clusters for the
Quenching of Star Formation**

Diego Pallero Astargo



**UNIVERSIDAD
DE LA SERENA
CHILE**



**DEPARTAMENTO
ASTRONOMÍA**

The importance of Low-Mass Clusters for the Quenching of Star Formation

Diego Pallero Astargo



UNIVERSIDAD DE LA SERENA

CHILE

Doctoral Thesis

To fulfill the requirements for the degree of
Doctor of Philosophy in Astronomy
at Universidad de La Serena under the supervision of
Prof. dr. Facundo A. Gómez (Astronomy, Universidad de La Serena)

Diego Pallero Astargo

August 23rd, 2021

*A journey of a thousand miles,
begins with a single step.*

Cover Image: A composite image of gas (gray) and stars (magenta) within 5 virial radii of one of the low-mass clusters from the C-EAGLE simulation. Galaxies can be seen populating the filamental structure of the cosmic web, in isolation, pairs and groups. Slowly and within these structures, galaxies will be accreted by the cluster at the centre of the image.

Credit: The image was made using Py-SPHViewer v1.0.0 (Benitez-Llambay, 2015).

Contents

	Page
1 Introduction	7
1.1 Galaxy formation and evolution: The state of the art	7
1.2 Galaxies in the Universe	10
1.2.1 Elliptical Galaxies (E):	12
1.2.2 Spiral galaxies (S):	12
1.2.3 Lenticular galaxies (S0):	13
1.3 Galaxy Clusters and its Components	13
1.3.1 Cluster catalogues	14
1.3.2 Distribution of Galaxies	15
1.4 Nature vs Nurture	17
1.4.1 Mass quenching	19
1.4.2 Environmental quenching	21
1.5 This Thesis	23
2 Numerical models of Galaxy Formation	29
2.1 EAGLE Simulation	31
2.2 Cluster-EAGLE project	34
2.2.1 The role of simulations on this Thesis	35
3 Tracing the Quenching History of Cluster Galaxies in the EAGLE Simulation	40
3.1 Introduction	41
3.2 Galaxy formation model	43
3.3 The end of the star forming phase: Definitions	44
3.3.1 SFR Strongest Drop	45
3.3.2 Critical sSFR criterion	46
3.4 Results	46
3.4.1 Strongest Drop Selection Criterion	47
3.4.2 Critical sSFR Selection Criterion	50
3.5 Discussion and Conclusions	56
4 Too dense to go through: The importance of low-mass clusters in satellite quenching	63
4.1 Introduction	64
4.2 Simulations	65
4.2.1 C-EAGLE simulations	65
4.2.2 Halo Identification	66
4.2.3 Ram Pressure and Restoring Force models	67
4.3 Properties of clusters: Quenched population and gas density profiles	68
4.3.1 Quenching of the star formation	68
4.3.2 Clusters at different times	72
4.3.3 Gas density of the intracluster medium	75
4.4 Discussion	78
4.4.1 Ram pressure as the main culprit	78

4.4.2	Over-quenching in C-EAGLE	79
4.5	Summary and Conclusions	81
5	Galaxy Quenching in Modified Gravity	87
5.1	Introduction	88
5.2	Galaxy formation in alternative Gravities	89
5.2.1	Modified Gravity Models	89
5.2.2	SHYBONE Simulations	92
5.3	Comparing haloes from different models	93
5.4	Galaxy population on different models	101
5.4.1	Quenched fraction	101
5.4.2	Colour distribution	105
5.5	Discussion and Future work	108
6	Summary and Conclusions	112
6.1	Future Work	115
	Acknowledgements	117

1 Introduction

The main goal of this thesis is to understand how galaxies in clusters cease their star formation activity. To do so, we will discuss how galaxies evolve as they pass through different environments. In this Chapter we discuss how the star formation activity of galaxies can be disturbed by several mechanisms, including those related to the environment in which galaxies reside.

By studying the evolution of galaxies, we can understand the growth of structures in the Universe. Therefore, we will start this Thesis by reviewing the current state of galaxy formation theory, and the cosmological model in which our current model of the Universe is constructed.

1.1 Galaxy formation and evolution: The state of the art

How, when and where galaxies form are key questions to be addressed in any galaxy formation theory. Understanding how galaxies form has been a hot topic in astronomy since the discovery of extragalactic nebulae by Edwin Hubble (Hubble, 1929). To shed some light on the processes that govern the growth of galaxies and structures, astronomers have been gathering information for decades. One result of these efforts is what is now known as the “*standard cosmological model*”, a physical paradigm in which our Universe can be reconstructed. Figure 1.1 shows a schematic representation of the evolution of the Universe in the current standard model “Lambda Cold Dark Matter”(Λ CDM). In this model, the density field of the Universe is composed of three components: 1) A dark energy component (Ω_Λ) responsible for the current accelerated expansion of the universe; 2) A cold dark matter component (Ω_c), that only interact with matter gravitationally and glues structures together; and 3) A baryonic matter component (Ω_b) that comprises all things that we can see, and is made by protons and neutrons.

The Λ CDM model is well supported by a combination of observations from different sources. Studies from the *Cosmic Microwave Background Radiation* (CMB) (Bogges et al., 1992; Komatsu et al., 2009, 2011; Planck Collaboration et al., 2014, 2020), Type Ia Supernovae magnitude-redshift relation (Riess et al., 1998; Perlmutter et al., 1999; Kowalski et al., 2008), abundance and scaling relations of galaxy clusters (Vikhlinin et al., 2009; Rozo et al., 2010) and the overall distribution of galaxies and quasars through galaxy surveys (Tegmark et al., 2004; Cole et al., 2005; Tegmark et al., 2006; Percival et al., 2007; Reid et al., 2010), have proven the success of this model on reproducing the Universe at different scales. These observations have allowed us to strongly constrain the dark energy density (Ω_Λ), the matter density (Ω_m), the baryonic density (Ω_b), the Hubble parameter (H_0), the power-law index of the primordial power spectrum (n_s) and the linear variance of the matter distribution (σ_8). These six key parameters of the model are known as *cosmological parameters*. Most current studies, in particular in this Thesis, have considered the following values obtained by the Planck mission on 2013 (Planck Collaboration et al., 2014): $\Omega_\Lambda = 0.693$; $\Omega_m = 0.307$; $\Omega_b = 0.04825$; $H_0/(100 \text{ km s}^{-1}\text{Mpc}^{-1}) = 0.6777$; $n_s = 0.9611$; $\sigma_8 = 0.8288$.

The basic picture behind this paradigm proposes that, around 13.7 billion years ago, the Universe was in a hot and dense state and, since then, has been expanding and cooling down. The moment when its expansion started from a singularity has received the name of “Big Bang”. Right after the Big Bang, and during an extremely short timescale ($\sim 10^{-30}\text{s}$), the Universe underwent an inflationary state. During this phase, the Universe exponentially expanded and the primordial quantum fluctuations on its otherwise uniform density field grew to cosmological scales. As dark matter only interacts gravitationally, these small perturbations were able to collapse under the effect of gravity, leading to their continuous growth after the initial inflationary phase. Linear perturbation theory can successfully be applied to describe the early growth of these perturbations. However, as time goes by, the

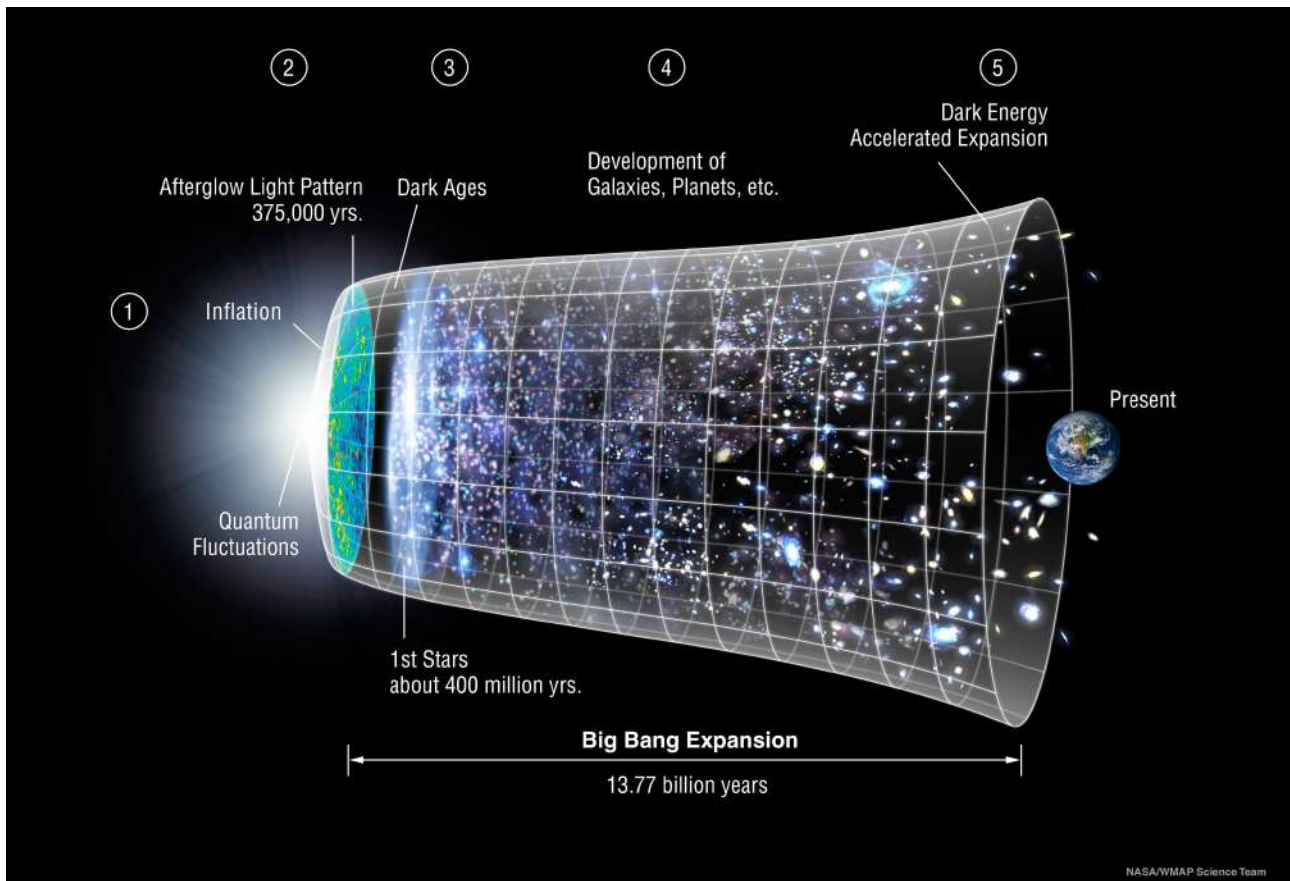


Figure 1.1: Illustrative image explaining the history of the Universe separated into five stages. 1) The Big Bang occurs and the inflation takes place, the Universe undergo exponential growth. 2) The hot plasma that composes the Universe gets cold enough for the photons to decouple from the baryons. Most of the matter is in form of neutral hydrogen, and the photons from the CMB are emitted. 3) Most of the universe is in a neutral state, and under the influence of gravity, structures start to grow. The first stars form. 4) Structures keep growing under the influence of gravity forming the cosmic web. Big structures as galaxies, filaments and galaxy clusters are formed. 5) The negative pressure associated to dark energy dominates and the expansion of the universe starts to accelerate. Image Credit: NASA/ LAMBDA Archive / WMAP Science Team

perturbations start to grow in a nonlinear fashion, making the description of the time evolution of such substructures significantly more complicated. Some analytical approximations can be applied to provide some insight into their evolution, as shown in Gunn (1977). However, most studies of the evolution of perturbations in the non-linear regime have been done with the aid of N-body simulations such as the MILLENIUM Simulation (Springel, 2005). These simulations have shown that, as it collapses, the matter distribution in the Universe takes the form of a filamentary structure known as *the cosmic web*. This indeed has been observed thanks to measurements of galaxies and quasar clustering in big galaxy surveys (Tegmark et al., 2004; Cole et al., 2005; Tegmark et al., 2006; Percival et al., 2007; Reid et al., 2010).

White & Rees (1978) for the first time, presented a model that fully coupled the growth of structures with the formation of luminous galaxies, using the formalism presented in Press & Schechter (1974) for the non-linear regime. In this pioneering work, they proposed that first, dark small objects form at early time. These objects grow by hierarchical clustering, becoming bound self-similar haloes. Regarding the luminous counterpart, the trapped gas within the potential well of these haloes started cooling down and fragmenting, giving rise to the first stars and galaxies as shown in Rees & Ostriker (1977). The model proposed in these works set the foundations of all modern galaxy formation theories. The subsequent mass growth of galaxies within this paradigm advances hierarchically. Briefly, after the formation of the first galaxies, mergers between galaxies of similar mass (referred to as major mergers) were a frequent phenomenon given the high density that the Universe had at that time. As time goes by, major mergers become less frequent and mergers between galaxies with different masses (referred to as minor mergers) become more relevant. These interactions play a key role in determining the morphological, kinematic and chemical properties of present-day galaxies. Nevertheless, other mechanisms contribute to the growth and evolution of galaxies throughout time as well.

To fully understand how galaxies evolve, we need a description of how galaxies form stars and the physics that regulates this phenomenon. As previously mentioned, the gas clouds trapped within dark matter haloes cools down and fragment. These fragmented clouds are converted into stars. The ratio between the gas mass converted into stars and the time passed is known now as *star formation rate*. As galaxies form stars, several physical mechanisms act on different scales. The medium surrounding the star-forming regions is heated by winds from massive stars or by supernovae feedback. When stars die they eject the synthesized material chemically enriching the surrounding medium. New stars are born from this now enriched gas, changing the properties of these newer generations and, thus, of the overall galaxy. The first galaxy formation models were obliged to use purely parametric recipes to reproduce the star formation histories in galaxies, due to the lack of a theoretical description of the star formation at the time (White & Frenk, 1991; Cole et al., 1994). Nevertheless, in the last decades, several advances have been made in the subject. This has been done thanks to a deeper understanding of the relation between the gas surface density and the star formation rate of a galaxy, which resulted in the development of *star formation laws*. Nowadays, thanks to galaxy surveys devoted to understanding the gas content of nearby galaxies (eg. Helfer et al., 2003; Walter et al., 2008), astronomers have been able to study the gas galactic component with unprecedented accuracy. Also, with the addition of better-calibrated methods to estimate the star formation rate in extra-galactic sources (Calzetti et al., 2007), evidence of star formation law in which the star formation rate correlates linearly with the amount of molecular gas available in galaxies have arisen (Kennicutt, 1998; Kennicutt et al., 2007).

The process of star formation is an extremely complex phenomenon and, even though some insights into the field have been obtained in the last decades, there is much work to do.

In the following sections, we will discuss how not only the intrinsic properties of galaxies could stop or enhance the star formation of a galaxy, but also how the environment in which a galaxy

resides could also affect their overall properties. In particular, in this thesis, we will focus on how the different physical mechanisms acting inside galaxy clusters could affect the star formation of their satellites galaxies.

1.2 Galaxies in the Universe

As stated, the purpose of this thesis is to shed light on some on the physical mechanisms that play a significant role on shaping galaxy properties, specially within galaxy clusters. As such, we yet to define “galaxies” as structures. What are galaxies? Galaxies are gravitationally bound structures composed of baryonic and dark matter. Within these structures, planets, dust, gas, and stars are embedded within a dark matter halo. These structures can be found in low-density environments such as voids or the field, but are typically found in pairs, groups, or clusters of galaxies.

Briefly after their discovery by Hubble, classification schemes were developed. As galaxies can be found in a wide variety of shapes and forms, using as a proxy their shape (or morphology) Hubble (1936) introduced in his book, *The Realm of Nebulae*, a scheme referred to as *The Hubble Sequence*. This sequence, also referred to as “tuning-fork diagram”, orders galaxies from the ones dominated by prominent bulges and an ovoid-like shape (elliptical), without complex features at first sight, to disk-like galaxies (spirals) with some prominent features such as spiral arms or bars. Figure 1.2 shows a representation of the Hubble sequence using galaxies from the “SIRTF Nearby Galaxies Survey” (SINGS). The survey is composed by infrared spectroscopy and imaging of 75 nearby galaxies, taken with the Spitzer Infrared Telescope Facility (SIRTF). In this figure we can see, from left to right, how galaxies are ordered by morphology, ranging from “elliptical” to “spirals”. Irregular galaxies are displayed separately given that they do not have a definite shape. Conventionally, those galaxies in the left-hand end of the sequence are referred to as “early-type” galaxies, while those towards the right-hand end as “late-type” galaxies. This is due to an initial misconception in which galaxies were thought to evolve from one end to the other.

	S0	cD	E	dE	dSph	BCD
M_B	-17 to -22	-22 to -25	-15 to -23	-13 to -19	-8 to -15	-14 to -17
$\log_{10}M(M_{\odot})$	10 - 12	13-14	8-13	7-9	7-8	~ 9
$D_{25}(\text{kpc})$	10-100	300-1000	1-200	1-10	0.1-0.5	< 3
(M/L_B)	~ 10	> 100	10-100	1-10	5-100	0.1-10

Table 1.1: Summarizing table for some key properties for early-type galaxies, extracted from Carroll & Ostlie (2007). In the table, we can see the typical absolute magnitude, size, stellar mass and mass to light ratio for different early type galaxies.

Even though this classification may seem simple, it has remained valuable up to this day since some galaxy properties strongly correlate with their morphology. Within this context, in what follows, we will briefly summarize the main properties of the most typical galaxies classified by Hubble. A general description of the general galaxy properties for early- and late-type galaxies can be found in Tables 1.1 and 1.2 respectively. For a detailed description of these galaxies, please refer to Carroll & Ostlie (2007).

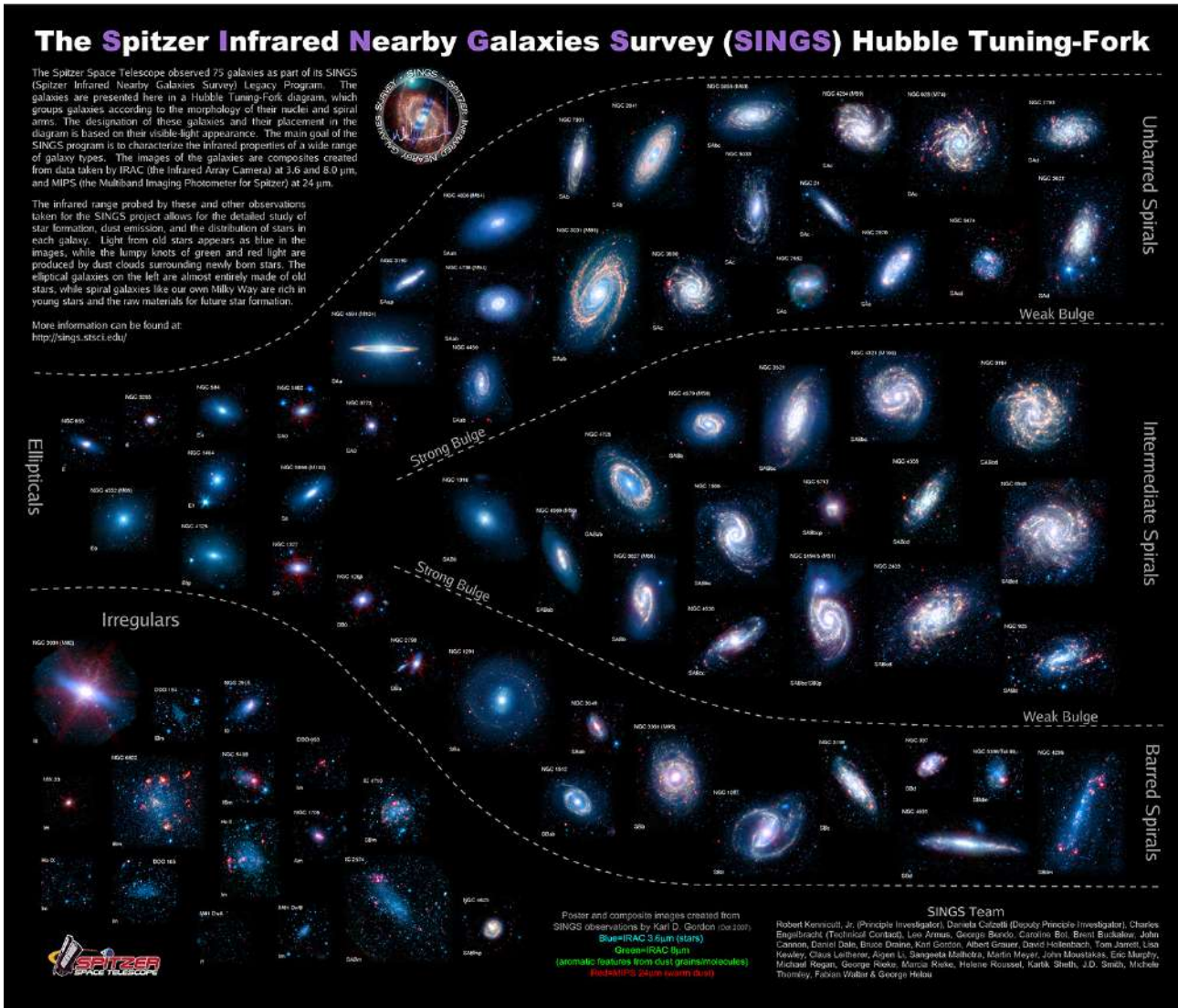


Figure 1.2: Galaxies from the “SIRTF Nearby Galaxies Survey”, ordered by their morphology to reproduce the Hubble Sequence. The survey is composed by 75 nearby galaxies from different morphologies, from elliptical to spirals, with the goal to characterize the infrared emission across a broad range of galaxy properties and environments. Credit: NASA/JPL-Caltech/K. Gordon (STScI) and SINGS Team

	Sa	Sb	Sc
M_B	-17 to -23	-17 to -23	-16 to -22
$\log_{10}M(M_\odot)$	9-12	9-12	9-12
(L_{bulge}/L_{tot})	0.3	0.13	0.05
Diam. (D_{25} ,kpc)	5-100	5-100	5-100
$(M/L_B)(M_\odot/L_\odot)$	6.2 ± 0.6	4.5 ± 0.4	2.6 ± 0.2
V_{max} range(km s $^{-1}$)	163-367	144-330	99-304
Opening angle	$\sim 6deg$	$\sim 12deg$	$\sim 18deg$
$\mu_{0,B}$ (mag arcsec $^{-2}$)	21.52 ± 0.39	21.52 ± 0.39	21.52 ± 0.39
(B-V)	0.75	0.64	0.52
(M_{gas}/M_{tot})	0.04	0.08	0.16
(M_{H2}/M_{HI})	2.2 ± 0.6	1.8 ± 0.3	0.73 ± 0.13

Table 1.2: Table summarizing the main properties of different late-type galaxies, extracted from Carroll & Ostlie (2007). In the table, are summarized the typical absolute magnitude, stellar mass, bulge to total luminosity ratio, size, mass to light ratio, maximum circular velocity, pitch angle, surface brightness, colour, gas to total mass, and HII to HI mass ratio.

1.2.1 Elliptical Galaxies (E):

Elliptical Galaxies show an oblate shape with little or no structural features in their brightness profile. They cover a wide range of stellar masses and absolute magnitude, ranging from the most massive galaxies in the Universe, such as the Brightest Cluster Galaxies (BCG), to dwarf elliptical galaxies which can be found in the local Universe, such as M32. Ellipticals, referred to with the letter E, are subdivided in the Hubble classification based on their ellipticity, $10 \times (a - b)/a$, where a and b correspond to the major and minor axis of the galaxy. This means that an E0 galaxy corresponds to the most spheroidal galaxy, while the E7 are to the more elliptical ones.

With the exception dwarf ellipticals, these galaxies typically show little or no star formation activity. They are sustained by the velocity dispersion of their stellar components and have lower gas mass fractions than their spiral counterparts. Elliptical galaxies are dominated by an old stellar population, which gives them their characteristic intrinsic redder colours. This type of galaxy can be found in any kind of environment and are widely dominant inside the dense cores of galaxy clusters.

1.2.2 Spiral galaxies (S):

Spiral galaxies are located on the other end of the Hubble sequence. Contrary to Elliptical galaxies, their main characteristic is to have a very flattened disk shape, typically displaying spiral like features emerging from their central region. These spiral patterns are often double and symmetric with respect to the centre, but more complex configurations can be also seen. In general, the light distribution of spiral galaxies can be split between an inner spheroidal component, referred to as bulge and similar in shape and properties to an elliptical galaxy, and a flattened and extended disk component within which spiral perturbations can be observed. Besides the spiral arms, this type of galaxy usually display ‘‘bar-like’’ perturbations, located in their inner central regions. Spiral galaxies which exhibit this feature are referred to as ‘‘barred spirals’’ and are denoted by a B after the classical S received by spirals

(SB). Barred spirals are as common as regular spirals, and both can be sub-classified as Sa, Sb and Sc (SBa, SBb, SBc), based on three aspects: 1) the openness of their spiral arms, 2) how well defined are their spiral arms and 3) the relation between their bulge and disk. In this sense Sa galaxies possess tightly wound not well resolved arms with a very prominent bulge, Sb galaxies possess slightly more opened, better resolved arms and a less prominent bulge, while Sc galaxies possess widely opened, well-defined arms with a small bulge component.

Regarding their intrinsic properties, compared to elliptical, spiral galaxies tend to have a higher star formation rate and higher stellar gas fractions. Contrary to elliptical galaxies, spirals are rotationally supported and have intrinsic bluer colours, a product of their active star formation. They also possess a mixture of old and young stellar populations, and are mainly found in low-density environments such as the field.

1.2.3 Lenticular galaxies (S0):

Lenticular galaxies (or S0), are early-type galaxies that show a disk-like structure but no spiral arms. Similar to spiral galaxies, S0 light profiles can also be separated between a predominant bulge in the centre and an extended disk emerging from the bulge. Lenticular galaxies appear to be an intermediate type of galaxy, between elliptical and spirals. They show similar properties to elliptical galaxies while maintaining a disk like shape, similar to spirals. Moreover, S0 galaxies can also show bars in the centre of their bulges. Generally, they possess redder colours than spirals and little or no star formation. They can be found in different environments, from the field to galaxy clusters.

1.3 Galaxy Clusters and its Components

Galaxies in the universe are often found in associations, from pairs or small groups to giant clusters containing thousands of galaxies. The transition between groups and clusters is smooth and is often defined by its number of members, being $N < 50$ and $N \geq 50$ for groups and clusters respectively, with a typical transition mass used to distinguish them around $M_{200} \sim 10^{14} M_{\odot}$. Their mass range, when combined, goes from $10^{12} M_{\odot} \lesssim M_{200} \lesssim 10^{15} M_{\odot}$. There are even more massive structures, known as “*Superclusters of galaxies*”, which usually correspond to an association of several Galaxy clusters. The main difference between clusters and superclusters, other than their mass, is their virialization state. In this sense, “*Rich Galaxy clusters*” correspond to the most massive gravitationally bound structures in the universe.

Even though galaxies dominate the optical appearance of galaxy clusters, it is now well established that they only represent just a small percentage of the total cluster mass. Thanks to the advances in X-ray detectors, we know now that clusters possess a strong X-ray emission, produced by a hot gas component located in the space within galaxies, which is known as “*intracluster medium*” (ICM). The ICM comprises the greatest fraction of their total baryonic mass. Yet, by combining the dynamics of their galaxy population, observations of X-ray emission, and gravitational effects such as weak lensing, we know that the mass of galaxy clusters is dominated by the presence of an extended dark matter component.

In this sense, the main components of galaxy clusters are defined as follows (for details see Kravtsov & Borgani, 2012):

- Galaxies: from hundreds to thousands depending on the mass of the clusters.
- Intracluster stars, also known as intracluster light: They are the debris stars from disrupted satellites accreted by clusters.

- Gas: principally hot gas. Is the main constituent of the intracluster medium and the baryonic component, and corresponds to roughly 15% of the total mass of the cluster.
- Dark Matter: the main constituent of galaxy clusters. Around 80% of the mass of a cluster belongs to dark matter alone.

Given their large mass, a significant fraction is composed of accreted material from very large distances (up to 10 cMpc). Clusters are expected to possess a representative sample of the mean matter content of the universe. All these characteristics place galaxy clusters as an important laboratory in the field of structure formation and observational cosmology.

One implication of the aforementioned condition, i.e., the most massive virialized structures in the Universe, is that they trace the most prominent density peaks of the large-scale structure. Therefore, their growth is directly related to the growth of cosmic structures. In addition, given the high galaxy density found within clusters, they also represent an ideal laboratory to study the evolution of galaxies in well-defined environments. From interactions among galaxies to the interaction between galaxies and the cluster itself, many different physical processes are taking place simultaneously within the context of galaxy evolution. For those reasons, galaxy clusters have been a subject of study since the second half of the twentieth century.

1.3.1 Cluster catalogues

In 1958 George Abell published the first catalogue of Galaxy Clusters (Abell, 1958). Visually inspecting data from the *Palomar Observatory Sky Survey*, Abell catalogued all those galaxy associations that were undoubtedly bound, covering from the north celestial pole ($+90^\circ$) down to -29° in declination. The following criteria were implemented:

- *Richness Criterion:* Clusters must contain at least 50 members brighter than 2 magnitudes fainter than the third brightest member ($m_3 + 2$). The number of galaxies within this range is later used to classify clusters by their richness, as a proxy for the total number of galaxies in the cluster.
- *Compactness Criterion:* All the associated members should be inside a radius $r \leq 1.5h^{-1}\text{Mpc}$ of the cluster centre. This value corresponds to an angular radius of $1.7/z$ arcmin, where the redshift was measured from the apparent magnitude of its 10^{th} brightest galaxy member.
- *Distance Criterion:* Clusters should be far enough so that all its members can be counted within one plate or, at most, as part of an adjacent plate. Moreover, an upper limit is set by the requirement that members cannot be counted at magnitudes lower than 20mag, so a limit was established for the third brightest member as $m_3 \geq 17.5\text{mag}$ ($z \sim 0.2$).

This catalogue contained 1682 clusters that fulfilled all the aforementioned criteria. Additionally, a richness class 0 was defined by Abell for clusters with less than 50 members ($30 \leq N < 50$) but the sample is not complete for these structures. A total of 1030 clusters are classified as richness class 0. Following this work, a new cluster catalogue was released by Abell et al. (1989) in which a sample of clusters from the Southern hemisphere was added. This new work, combined with the previous one, generated a sample of 4073 clusters fulfilling all the aforementioned criteria. The pioneering work of Abell set the bases to study galaxy clusters. Using more sophisticated techniques, several

Richness Class R	N	Number of clusters from the northern sample	Number of clusters from the southern sample
1	50 - 79	1224	656
2	80 - 129	383	273
3	130 - 199	68	41
4	200 - 299	6	1
5	>300	1	0

Table 1.3: Richness classes and the number of clusters per hemisphere as defined by Abell on its work (Abell, 1958; Abell et al., 1989). Here, N correspond to the number of clusters between m_3 and $m_3 + 2$ per Richness bin.

surveys have focused entirely on this topic to expand the sample of available clusters in both, mass and redshift.

As previously discussed, given the large mass and deep potential well of galaxy clusters, these structures can be studied using different techniques. For example, X-rays produced by the Bremsstrahlung emission of the hot gas component have been the focus of some space telescopes from the last decades. Surveys such as ROSAT (Voges et al., 1999), Chandra (Weisskopf et al., 2000) and XMM-Newton (Jansen et al., 2001), had as one of their primary goals to make all-sky cluster catalogues. With the arrival of eROSITA (Predehl et al., 2021) the sample of clusters is expected to grow even more. The same hot gas component can be detected by decrements in the Cosmic Microwave Background produced by the Sunyaev-Zeldovich effect (Sunyaev & Zeldovich, 1972). The South Pole Telescope (Carlstrom et al., 2011; Benson et al., 2014), The Atacama Cosmology Telescope (Orlowski-Scherer et al., 2021) and the Planck Mission (Planck Collaboration et al., 2016) have mapped the CMB of a large part of the sky, making large catalogues of galaxy clusters, using the Sunyaev-Zeldovich effect as a tool to identify them. Finally, a more complex and recent technique, based on gravitational lensing, have been used to measure the mass of rich galaxy clusters. As light from background sources passes through the deep potential well of these massive structures is deflected. The arcs produced by this effect can be used to deconstruct the potential and thus, the mass distribution of the deflector (eg. Koopmans, 2005; Koopmans et al., 2006; Bolton et al., 2006; Suyu et al., 2017). This phenomenon nowadays is one of the more studied techniques to measure the properties of clusters.

1.3.2 Distribution of Galaxies

In 1962, Abell presented an additional classification for clusters using their galaxy distribution as a proxy (Abell, 1962). In his work, he classified clusters as regulars if their galaxy members show a radially symmetric distribution, with the galaxy density growing towards the centre; similar in structure to stars in globular clusters. Generally, this case corresponds to the richest galaxy clusters in his sample, with the population being widely dominated by early-type galaxies. All those clusters that show a less defined structure were classified as irregular. They usually possess several sub-condensations, as if they were many clusters interacting. On this kind of cluster, spiral galaxies can often be found at their outskirts. Following this work, Oemler studied a sample of 15 representative clusters from different richness, classes and morphology (Oemler, 1974). He distinguished three principal types of clusters according to their galaxy content.

- cD clusters: They have a unique dominant central cD galaxy, which are giant elliptical galaxies with a more extender stellar halo. The ratio between elliptical, lenticular and spiral galaxies is roughly 3:4:2. These clusters are widely dominated by early-type galaxies.
- Spiral-rich clusters: These clusters does not have a well-defined shape and are dominated by late-type galaxies. The ratio between elliptical, lenticular and spiral galaxies is roughly 1:2:3.
- Spiral-poor clusters: These clusters does not have a well-defined shape either and are dominated by early-type galaxies. The ratio between elliptical, lenticular and spiral galaxies is roughly 1:2:1.

Oemler also studied the correlation between the cluster structures and their galaxy content. Some of his main findings can be summarized as follows:

- cD clusters possess a galaxy distribution that rapidly grows towards the centre, are spherically symmetric and its mass distribution can be modelled by an isothermal gas sphere. On the other hand, spiral rich clusters do not show any symmetry in the galaxy distribution and are not as concentrated as cD clusters. In general, their galaxy distribution is roughly uniform towards the central region. Spiral poor clusters possess an intermediate distribution between the previous two.
- For cD and poor spiral clusters, Oemler found that galaxy members are segregated by mass. This means that massive galaxies form a core in the inner region of clusters, while less massive galaxies are located throughout the entire cluster without any particular location. This is only relevant for the most massive galaxies ($m < m_1 + 2$), where m_1 correspond to the brightest galaxy in the cluster. In the case of spiral-rich clusters, no evidence for mass segregation was found.
- For cD and poor spiral galaxy clusters, morphological segregation also was found. The fraction of spiral galaxies decreases rapidly towards the centre of clusters, forming a halo around a core of elliptical and lenticular galaxies. This segregation was not found in spiral-rich clusters, where elliptical, lenticular and spiral galaxies were found uniformly throughout the whole clusters.

The latter item was further studied by Dressler (1980), who found a clear relation between the morphology of galaxies and the galaxy number density. Here the galaxy number density corresponds to the number of galaxies within a surface projected in the sky ($N_{\text{gal}}\text{Mpc}^2$). In general, galaxy clusters possess a different mixture of galaxy types when comparing with the distribution of field galaxies. He showed that the fraction of early-type galaxies is higher in the denser cluster environment. Indeed Dressler showed that, while the fraction of elliptical galaxies rises toward higher density environments, the fraction of spirals steadily decreases. In the case of lenticular galaxies, the number fraction grows towards dense environments, but in a less pronounced fashion. On the other hand, Brandy Whitmore and Diane Gilmore argued that this morphology-density relation found by Dressler is the reflection of another, more fundamental relation between galaxy morphology and its distance to the cluster centre (Whitmore & Gilmore, 1991). Their study showed that cluster cores not only play a key role in regulating the morphology of their galaxy members but also in disrupting some of the spiral satellites as well.

Nowadays, thanks to the big databases provided by galaxy surveys, a deeper understanding of the relation between the cluster environment and morphological transformations have developed. In particular, using photometric data from the early data release of the Sloan Digital Sky Survey (SDSS,

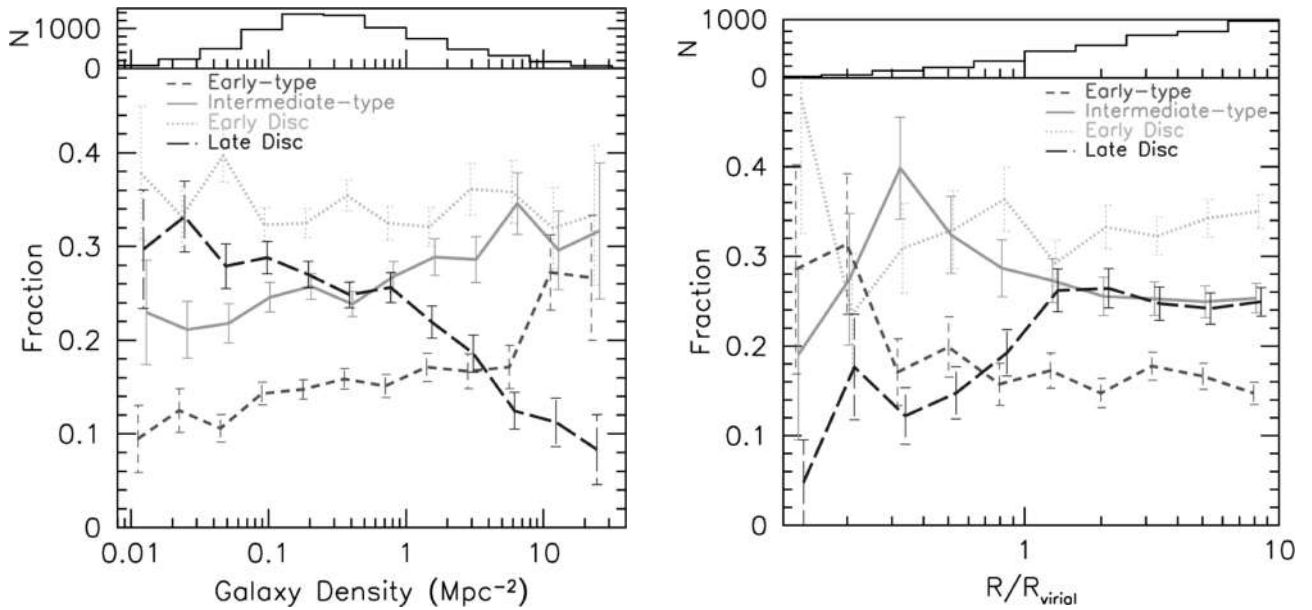


Figure 1.3: Number fraction of galaxies as a function of the *left panel*: local galaxy density and *right panel*: the cluster-centric distance. Galaxies were separated according to their morphology as early-type representing elliptical galaxies; intermediate-type, composed mainly by lenticular galaxies; early disc for Sa spirals, and late-type disc for Sc spiral galaxies. Histograms in the upper panel represent the number of galaxies per density/radial bin from the total sample. From Goto et al. (2003)

York et al., 2000), Goto et al. (2003) revisited the analysis previously performed by Dressler. To define their galaxy sample, and as an improvement with respect to the visual classification performed by Dressler, they used two different automated galaxy morphology classification criteria, capable of separating galaxies into *early-type* (E, mostly elliptical), *intermediate-type* (I, mostly S0), *early-disc* (ED, mostly Sa) and *late-disc* (LD, mostly Sc). Additionally, all studied galaxies possessed confirmed spectroscopic redshift, which allowed the authors to measure the three-dimensional local galaxy density. Finally, they extended the morphology–density relation into the field region, to understand the impact that dense environments have on morphological transformations. Their results can be seen in Figure 1.3, where the morphology–density and morphology–clustercentric distance relations are plotted. As the figure shows, early-type galaxies such as elliptical and lenticular, are widely dominant in very crowded regions as cluster cores. Late type galaxies (such as Sc spirals), instead, are rarely found in these dense regions, representing less than 5% of the total sample inside cluster cores. These results highlight what was previously proposed by both authors. Environment plays a key role in shaping the evolution of galaxies. To understand how galaxies evolve in dense environments, and which is the impact that it has on its stellar population, is key to understand how galaxies form and evolve.

1.4 Nature vs Nurture

A key aspect in galaxy evolution, as previously stated, is to understand how galaxies form stars, and what mechanisms regulate their efficiency. Throughout the history of a typical galaxy, its cold gas reservoir is gradually consumed as it is turned into new stellar populations. The resulting star formation history of a galaxy is closely related to galaxy’s integrated colours, luminosity, metallicity and morphology. Regarding their environmental conditions, once their gas content is completely con-

sumed, they are not able to keep forming stars and are finally catalogued as *passive galaxies*. Given the short lifespan of massive stars, the luminosity of passive galaxies is dominated by old red stars, such as F+G population (Morgan & Mayall, 1957). Since the twentieth century, it has been well established, that the colour of a galaxy reflects its predominant stellar population (Humason, 1936; Morgan & Mayall, 1957). Moreover, it is known that the morphology of a galaxy is also related to its condition of star-forming or passive. Within this context, the colour-morphology (Roberts & Haynes, 1994) and the colour-magnitude relations (Chester & Roberts, 1964; Faber, 1973) have been widely used to characterize galaxies by their properties. It was usual to split galaxies based on their morphology; this is, between spirals and ellipticals. However, after the early data release from SDSS, Strateva et al. 2001 showed that the colour distribution of galaxies in the universe was strongly bimodal. As the colour represents the predominant stellar population of galaxies, in addition to separate galaxies by their morphology, one can split a sample between *red* and *blue* galaxies. By doing this, we can take into account not just the morphology of the galaxy, but also their star formation history, their dust content and metal-enrichment history.

How galaxies transform from star-forming blue galaxies to passive red galaxies is a very intricate process, so the dominant mechanism behind this transformation is still an open question. Several works have tried to shed some light on the subject. Faber et al. 2007 showed a very simplistic representation of the different pathways that galaxies could follow from the blue star-forming region to the red sequence. This image is shown in Figure 1.4 and uses the colour stellar mass relation to exemplify the process. This representation assumes that galaxies cease their star formation due to a gas-rich major merger. However, these authors argue that the representation is insensitive to the mechanism producing the cease of the star formation. They discuss that once that galaxies reach the red sequence, they can keep growing in stellar mass via gas-poor or “dry” mergers. Track A shows the evolution undergone by galaxies that cease their star formation early in time, followed by its subsequent mass growth due to dry mergers; track B shows the path followed by galaxies if their star formation ceases late and does not undergo any dry merger; track C shows the path followed by galaxies if they undergo a mixed model. Their work shows that track C better represents the properties of elliptical galaxies in the local and distant universe, being the most accepted model nowadays. Nevertheless, there is still much work to do in the subject.

In the literature, the processes behind the cease of the star formation are referred to as “quenching”. When a galaxy is considered quenched, however, varies between authors. Some have used galaxy colours to define whether it is star-forming or not (e.g Peng et al., 2010). Others have chosen to use a threshold in the specific Star Formation Rate (*sSFR*), which is the ratio between the gas mass converted into stars and the stellar mass that the galaxy possesses at a given time ($sSFR \equiv SFR/M_*$). Using the later criteria, a galaxy is defined as quenched if the *sSFR* become negligible (e.g. Wetzell et al., 2012). Among the physical mechanisms that can be affecting the star formation history of galaxies, there is a dichotomy regarding the character of the quenching process. It relates to whether the mechanisms are internally or externally triggered. Is the cease of galaxy star formation activity related to the environment in which it resides, or is it related to internal properties such as its mass? Is it *nature or nurture*?

The morphological segregation that we review in the previous section was one of the first pieces of evidence that the environment plays a key role in galaxy evolution. Understanding how the morphology of galaxies changes as they experience the transition from low-density environments as the field, to the more dense environments as galaxy clusters have been a subject of study since the work of Abell came to light. On the other hand, it has been widely reported that the efficiency of the internal physical processes that can significantly affect the star formation activity is correlated with its mass. For dwarf galaxies, supernovae feedback and stellar winds can deplete their gas content thus ceasing

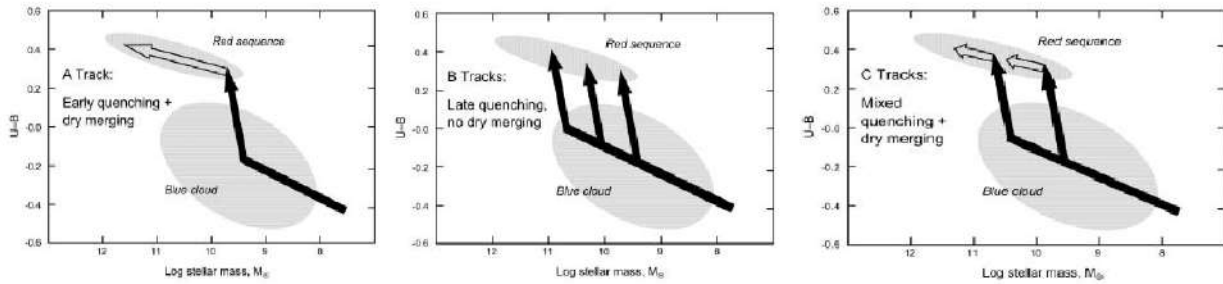


Figure 1.4: Schematic representation of the different paths that galaxies could follow in their transition from the blue star-forming region to the red sequence, represented on the colour stellar-mass diagram. Nearly vertical lines show the quenching tracks, where it is assumed that galaxy quenching is produced by a major merger between star-forming galaxies with the same mass. Galaxies could keep evolving once they reach the red sequence by a series of gas-poor or “dry” mergers. The following evolution is represented by the white arrows. Three different paths for the population of the red-sequence are shown. On the left panel, is shown the evolutionary track in which galaxies are early quenched and then slowly evolves by dry mergers (A Track). In this model, most of the mass assembly of the galaxy is produced on the red sequence. The opposite case is shown in the middle panel (B Track), in which galaxies suffer a late quenching and little or no mass assembly is produced in the red sequence. Finally, a mixed contribution process is shown in the right panel (C Track). Credit: Image extracted from Faber et al. 2007

their star formation. For massive galaxies, feedback from their super massive black hole starts to gain relevance, heating the medium and halting the accretion of cold gas needed to form new stars. Each mechanism leaves different imprints on the properties of galaxies. In Peng et al. 2015 the differences in the mean stellar metallicity of galaxies that undergo different quenching mechanisms are discussed. Particularly, Figure 1.5 shows a schematic representation of the stellar metallicity enrichment undergone by galaxies that suffer sudden gas stripping and those that slowly decrease their star formation by stopping their gas accretion. The latter process is known as strangulation. The quenching time on this image represents the moment when some mechanism that intervenes the gas of a galaxy takes place, either when their gas is stripped or when the galaxy cannot accrete new gas. Galaxies that are violently depleted from their gas, by ram pressure stripping or outflows as a product of energetic feedback, rapidly get quenched. As their gas reservoirs are stripped, there is no available material to keep forming stars. As a result, the mean stellar metallicity of their stellar population stops evolving after their quenching time. On the other hand, if the galaxy undergoes starvation it can keep forming stars until all its gas content is consumed. As the galaxy does not accrete new gas, the metallicity of the medium is constantly enhanced, and the new stellar populations are formed from this enriched gas. Consequently, its mean stellar metallicity is expected to be higher than for galaxies that suffer severe stripping. The following subsections review some of the mechanisms that can produce the quenching of the star-formation and summarize their importance and main characteristics.

1.4.1 Mass quenching

We will refer as “*mass quenching*” or “*internal quenching*” to any physical mechanism that can stop or reduce the star formation of a galaxy that is not externally triggered. These mechanisms are directly related to the stellar mass of the galaxy and are usually related to gravitational instabilities or energetic feedback effects.

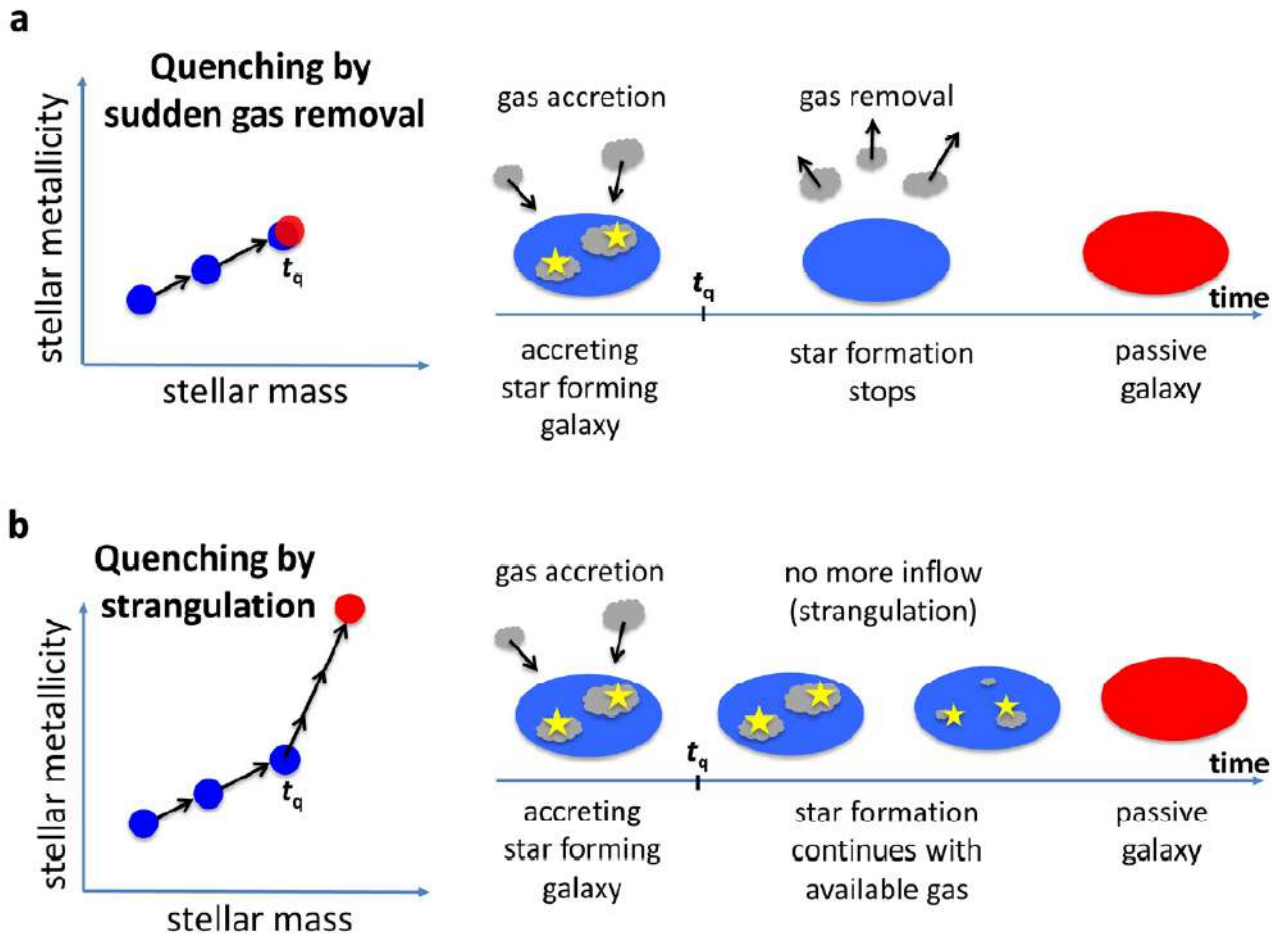


Figure 1.5: Schematic representation of the imprints that different quenching mechanisms produce on the properties of galaxies. Panel a) shows the evolution of a galaxy stellar metallicity when it suffers a severe gas removal, associated with processes such as ram pressure stripping or gas outflows by energetic feedback. Panel b) shows the variation of a galaxy stellar metallicity that gets quenched via strangulation. If the gas of a galaxy is suddenly stripped, it rapidly stops its star formation. Since the galaxy cannot continue forming stars, the medium is no longer enriched and the mean stellar metallicity cannot keep rising. Instead, if a galaxy slowly stops forming stars the medium keeps getting enriched. When a galaxy suffers strangulation, it stops accreting gas from the cosmic web. Thus, the metallicity of the gas grows and, subsequently, increases the stellar metallicity. Credit: Image extracted from Peng et al. 2015.

Some of the first insights on the subject were given by Avishai Dekel and Joseph Silk (Dekel & Silk, 1986). They discussed the impact that stellar winds and supernovae feedback could have on the overall star formation of dwarf galaxies. They found that a substantial amount of gas loss is needed to replicate the metallicity and surface brightness profiles measured on their observational sample. Given that dwarf galaxies possess shallow potential wells, feedback from supernovae or stellar winds could be strong enough to remove or heat their gaseous component. In particular, they attribute this gas loss to supernovae explosions produced by the starburst episodes suffered by galaxies throughout their history. These mechanisms allowed them to explain the different types of elliptical dwarf galaxies that exist in the Universe.

Even though this work shed some light on the importance that energetic feedback has on regulating the star formation of a galaxy and the imprints on galaxy properties, its model still needed refinement to reproduce the sequence of galaxies observed by surveys. In this sense, to be able to reproduce realistic galaxies, two factors should be taken into account. First, to reproduce dwarf (and intermediate-mass galaxies) as observed, a better feedback model for the supernovae and stellar winds that could regulate the gas cooling mechanisms was needed. Second, for more massive galaxies, the impact that active galaxy nuclei (AGN) feedback has on the regulation of the cooling mechanisms of galaxies had to be taken into account. This becomes especially relevant for massive galaxies, as the stellar origin heating mechanisms does not have much influence in the high mass end. Regarding the first issue, Cantalupo (2010) presented a well-calibrated model of self-regulated feedback in which not just supernovae and stellar winds are taken into account, but also photoionization by local sources. Cantalupo argued that local photoionization produced by star-forming galaxies could play a key role in halo gas cooling and accretion. Energetic photons emitted during the star formation activity could remove from the gas important coolant ions via direct photoionization. This produced a reduction in the cooling rate and an increase in the photoheating of the sources, making the timescales needed for cooling to take place much longer for the accreted gas. In this sense, the star formation and cooling rates for dwarf and intermediate-mass galaxies are dependants on the star formation rate of the galaxy itself, as starburst activities could produce the quenching of star formation due to strong photoionization sources, supernovae feedback from massive stars and strong winds.

On the other hand, it is well known that massive galaxies host at their centre SMBHs. This SMBH can eject energy to the medium as a consequence of episodes of intense accretion. This accreting/emitting phase is known as Active Galaxy Nuclei (AGN) and is amongst the most energetic phenomena in the universe. Now, it is well established that the evolution and growth of the AGN is closely related to the evolution of the host galaxy, but the physical mechanism that links their evolution is still a subject of debate. Fabian (2012) reviewed the impact that feedback has on the overall properties of an AGN and its host galaxy. Fabian discuss how the feedback from the AGN is efficient enough to stop the star formation by heating the surrounding gas and destroying molecular clouds where the star formation could take place. Also, the energetic feedback could prevent the accretion of cool gas from the circumgalactic medium and maintain the galaxy “quenched”. Nevertheless, as AGN are a transient phenomenon, this quenched status may last just as long as the SMBH remains active.

1.4.2 Environmental quenching

The environment in which a galaxy resides plays a key role in determining its overall properties. Many different processes can affect the star formation efficiency of a galaxy. Which process prevails depends on the host halo mass, the galaxy-number density and the gas density of the host halo, among other environmental characteristics.

In this sense, we will refer as “environmental quenching” to any externally triggered physical mech-

anism that can cease the star formation of galaxies. In particular, in this thesis, we will focus on those processes that act within galaxy clusters. Given their condition of “biggest bound structures in the universe”, many different environmentally triggered mechanisms are likely to take place simultaneously inside these structures (for a review, see Boselli & Gavazzi, 2006; Cortese et al., 2021). Which one dominates over the other, however, remains an open question. Within the potential well of a cluster, satellite galaxies can experience strong tidal forces, can interact hydrodynamically with the hot gas component of the intracluster medium, and gravitationally with other satellites from the cluster itself. In what follows, I review the most important phenomena taking place within clusters, to understand the impact that each of these processes could have on the star formation activity of a galaxy.

Once a galaxy becomes a satellite of a cluster, the deep potential well of the host starts affecting its properties. It has been reported that rapidly changing tidal forces can disturb the morphology of galaxies in clusters by inducing bars, lopsidedness, spirals structure and warps (Valluri, 1993; Yoon et al., 2019). Also, tidal interactions could detonate nuclear or disk star formation by gas inflows and by compressing the already available gas (Miller, 1986; Byrd & Valtonen, 1990; Yoon & Im, 2020). Even though these mechanisms could hardly remove the gas content of galaxies, they accelerate the gas consumption. In this way, tidal interactions with the potential well could indirectly produce an acceleration of the satellites star formation quenching. Galaxies within a cluster also interact hydrodynamically with their environment. Gunn & Gott (1972) proposed that the interstellar medium of galaxies could be removed if they are travelling through a dense medium at high velocities, as in the case of galaxies accreted by galaxy clusters. This mechanism was called “ram pressure”. It becomes efficient when the ram pressure exerted by the cluster is greater than the restoring force per unit of area exerted by the mass of the galaxy itself. Mathematically, this relation can be expressed as follows:

$$\rho_{\text{ICM}} V_{\text{gal}}^2 > 2\pi G \Sigma_{\text{star}} \Sigma_{\text{gas}},$$

where ρ_{ICM} correspond to the local density of the intracluster medium, V_{gal}^2 the relative velocity of the galaxy with respect to the local environment, G is the gravitational constant, Σ_{star} the stellar surface density and Σ_{gas} the gas surface density. Depending on the efficiency of the ram pressure, this phenomenon could quench the star formation of a galaxy in a “*rapid-*” or a “*delayed-fashion*”. If the ram pressure is high enough, it can be able to strip the cold gas of the inner galactic region, quenching their star formation activity in a rapid fashion within a very short time scale ($\lesssim 0.8 \text{Gyr}$) (Wetzell et al., 2012; Jaffé et al., 2015; Cora et al., 2018; Roberts et al., 2019). This could happen when galaxies cross the inner parts of galaxy clusters, where the density of the intracluster medium reaches extremely high values, in addition to the high velocities that galaxies have acquired since their infall. On the other hand, if ram pressure is not efficient enough to strip the cold gas but is high enough to strip the hot component, galaxies quench their star formation in a delayed fashion due to a process called “*starvation*” (Larson et al., 1980; Peng et al., 2015). The gas that replenishes the cold gas from the disk, in charge of the star formation, comes from the inflow of an extended hot gas reservoir in the outer halo of the galaxy. When removing the outer envelope of the halo, galaxies are left without any mechanisms to maintain their star formation after the gas from the disk is depleted. This process could take several Gyr (Treu et al., 2003; Wetzell et al., 2013; Peng et al., 2015).

Finally, as the galaxy number density is higher in clusters than in any other type of structure, encounters between the satellites are expected to take place. It has been reported that galaxy mergers play a massive role in changing the morphological properties of galaxies (Toomre & Toomre, 1972; Barnes & Hernquist, 1996) but, given the high dispersion velocity in the cluster field, major mergers between galaxies are not expected to take place. Instead, cluster galaxies are expected to be affected

by several aggressive close ($\sim 50\text{kpc}$) encounters at high velocities called “harassment” (Moore et al., 1996, 1999). The accumulation of these encounters, in addition to the interaction between galaxies and the tidal forces exerted by the potential well of the cluster, progressively heats the stellar component in galaxies, increasing their velocity dispersion and decreasing the angular momentum of the gaseous component. This phenomenon could produce fueling from the cold gas to the centre of the galaxy, leading to a short nuclear episode of star formation, and subsequently to a definitive quenching. The impact of this process on the properties of galaxies is related to the number of interactions, the strength of the interaction and the mass of the galaxies.

In general, low surface brightness galaxies are more affected by this process but, except for very dwarf galaxies, they are hardly destroyed in the process. Also it has been reported that this process becomes more effective as galaxies approach the cluster centre (Moore et al., 1999; Smith et al., 2015).

In the next section, I will discuss the methodology that I will follow to understand to which extent these processes are affecting the galaxies in our sample.

1.5 This Thesis

The objective of this thesis is to identify, separate and characterize the processes that govern the evolution of galaxies that we observe in galaxy clusters at the present day. In particular, we want to understand how, when and where the satellite population of galaxy clusters reach the quenched state in which are found at present-day. To do this, I have used state-of-the-art hydrodynamical simulations from the EAGLE and C-EAGLE projects to follow the star formation history of all the surviving satellites inside the clusters on the simulations. The EAGLE simulation counts with a periodic box with 100 comoving Mpc side length, in which 10 galaxy clusters with a $M_{200} > 10^{14}M_{\odot}$ are found at $z = 0$. On the other hand, the C-EAGLE project is composed by a set of 30 galaxy clusters ranging in mass from $10^{14} < M_{200}/M_{\odot} < 10^{15.4}$ simulated in a zoom-in fashion. Hydrodynamical simulations are a powerful tool to understand galaxy evolution in a statistical context, as they allow us to characterize the process by which galaxies are stripped of their gaseous component and its relation with their star formation activity, using a fully self-consistent cosmological model.

In Chapter 2, I summarize the different galaxy formation models implemented in the simulations analyzed in this Thesis. In particular, we will review the main characteristics of the EAGLE and the C-EAGLE projects, and discuss how the model implemented on these simulations can reproduce the most relevant overall properties of galaxy populations, thus making them suitable for our study.

In Chapter 3 we characterize the quenching history of the cluster galaxies extracted from the EAGLE simulation. We show that the strongest drop in the star formation rate of a galaxy is not necessarily related to the quenching in their star formation, but is related to a retarded growth in their stellar content. This strongest drop could happen in any kind of halo and is not related to a particular time nor mass of the host. On the other hand, for the definitive quenching of the star formation, a strong dependence on the halo mass is seen. We show that galaxies tend to get quenched inside massive haloes such as galaxy clusters and that the fraction of pre-quenched galaxies grows with the mass of the host at $z=0$. We also see that, in general, massive galaxy clusters, tend to accrete more pre-quenched galaxies, because they are accreting small clusters and massive galaxy groups with an already quenched population.

In Chapter 4 we use the C-EAGLE simulation to study in detail the main mechanisms producing this quenching of the star formation seen in Chapter 3. We find that galaxies get quenched briefly after being accreted by the first massive halo in which they reside. This usually corresponds to a low-mass cluster, regardless of the mass of their final host. This is clearer while looking at clusters at higher redshift, where the pre-quenched fraction decreases with redshift regardless of the cluster mass. This

is because galaxies are observed in the first massive halo in which reside. After crossing the virial radii of the cluster, galaxies tend to get quenched in a timescale between $0 \lesssim t_q - t_{\text{infall}} \lesssim 4$ Gyr with a dramatic increase in the quenched fraction within a timescale of $0 \lesssim t_q - t_{\text{infall}} \lesssim 1$ Gyr. This is related to a ram-pressure stripping event. For most galaxies, this mechanism becomes efficient near the R_{500} of galaxy clusters, when the intracluster medium of the cluster reaches a density of $n_{\text{H,ICM}} \sim 3 \times 10^{-5} [\text{cm}^{-3}]$. In Chapter 5, we explore the implications that different models of modified gravity have on the properties of galaxies residing in different environments. We quantify the discrepancies between the passive fractions on each model and define a protocol to fairly compare structures on different models. Finally, we set the foundations for a future work, where we will explore the different pathways followed by galaxies from their star-forming to their quenching state on different gravities. Finally, in Chapter 6 we summarize the main conclusions of this thesis and discuss future work that could be done to improve our understanding of the matter.

Bibliography

Abell G. O., 1958, , 3, 211

Abell G. O., 1962, in McVittie G. C., ed., Vol. 15, Problems of Extra-Galactic Research. p. 213

Abell G. O., Corwin Harold G. J., Olowin R. P., 1989, , 70, 1

Barnes J. E., Hernquist L., 1996, , 471, 115

Benson B. A., et al., 2014, Proc. SPIE Int. Soc. Opt. Eng., 9153, 91531P

Bogges N. W., et al., 1992, , 397, 420

Bolton A. S., Burles S., Koopmans L. V. E., Treu T., Moustakas L. A., 2006, , 638, 703

Boselli A., Gavazzi G., 2006, , 118, 517

Byrd G., Valtonen M., 1990, , 350, 89

Calzetti D., et al., 2007, , 666, 870

Cantalupo S., 2010, , 403, L16

Carlstrom J. E., et al., 2011, , 123, 568

Carroll B. W., Ostlie D. A., 2007, An Introduction to Modern Astrophysics, 2nd (international) edn

Chester C., Roberts M. S., 1964, , 69, 635

Cole S., Aragon-Salamanca A., Frenk C. S., Navarro J. F., Zepf S. E., 1994, , 271, 781

Cole S., et al., 2005, , 362, 505

Cora S. A., et al., 2018, , 479, 2

Cortese L., Catinella B., Smith R., 2021, , 38, e035

Dekel A., Silk J., 1986, , 303, 39

Dressler A., 1980, , 236, 351

Faber S. M., 1973, , 179, 731

Faber S. M., et al., 2007, , 665, 265

Fabian A. C., 2012, , 50, 455

Goto T., Yamauchi C., Fujita Y., Okamura S., Sekiguchi M., Smail I., Bernardi M., Gomez P. L., 2003, , 346, 601

Gunn J. E., 1977, , 218, 592

Gunn J. E., Gott III J. R., 1972, , 176, 1

- Helfer T. T., Thornley M. D., Regan M. W., Wong T., Sheth K., Vogel S. N., Blitz L., Bock D. C. J., 2003, , 145, 259
- Hubble E. P., 1929, , 69, 103
- Hubble E. P., 1936, Realm of the Nebulae
- Humason M. L., 1936, , 83, 10
- Jaffé Y. L., Smith R., Candlish G. N., Poggianti B. M., Sheen Y.-K., Verheijen M. A. W., 2015, , 448, 1715
- Jansen F., et al., 2001, , 365, L1
- Kennicutt Jr. R. C., 1998, , 498, 541
- Kennicutt Robert C. J., et al., 2007, , 671, 333
- Komatsu E., et al., 2009, , 180, 330
- Komatsu E., et al., 2011, , 192, 18
- Koopmans L. V. E., 2005, , 363, 1136
- Koopmans L. V. E., Treu T., Bolton A. S., Burles S., Moustakas L. A., 2006, , 649, 599
- Kowalski M., et al., 2008, , 686, 749
- Kravtsov A. V., Borgani S., 2012, , 50, 353
- Larson R. B., Tinsley B. M., Caldwell C. N., 1980, , 237, 692
- Miller R. H., 1986, , 167, 41
- Moore B., Katz N., Lake G., Dressler A., Oemler A., 1996, , 379, 613
- Moore B., Lake G., Quinn T., Stadel J., 1999, , 304, 465
- Morgan W. W., Mayall N. U., 1957, , 69, 291
- Oemler Augustus J., 1974, , 194, 1
- Orlowski-Scherer J., et al., 2021, arXiv e-prints, p. arXiv:2105.00068
- Peng Y.-j., et al., 2010, , 721, 193
- Peng Y., Maiolino R., Cochrane R., 2015, , 521, 192
- Percival W. J., Cole S., Eisenstein D. J., Nichol R. C., Peacock J. A., Pope A. C., Szalay A. S., 2007, , 381, 1053
- Perlmutter S., et al., 1999, , 517, 565
- Planck Collaboration et al., 2014, , 566, A54
- Planck Collaboration et al., 2016, , 594, A24

- Planck Collaboration et al., 2020, , 641, A1
- Predehl P., et al., 2021, , 647, A1
- Press W. H., Schechter P., 1974, , 187, 425
- Rees M. J., Ostriker J. P., 1977, , 179, 541
- Reid B. A., et al., 2010, , 404, 60
- Riess A. G., et al., 1998, , 116, 1009
- Roberts M. S., Haynes M., 1994, in Meylan G., Prugniel P., eds, European Southern Observatory Conference and Workshop Proceedings Vol. 49, European Southern Observatory Conference and Workshop Proceedings. p. 197
- Roberts I. D., Parker L. C., Brown T., Joshi G. D., Hlavacek-Larrondo J., Wadsley J., 2019, , 873, 42
- Rozo E., et al., 2010, , 708, 645
- Smith R., et al., 2015, , 454, 2502
- Springel V., 2005, , 364, 1105
- Strateva I., et al., 2001, , 122, 1861
- Sunyaev R. A., Zeldovich Y. B., 1972, *Comments on Astrophysics and Space Physics*, 4, 173
- Suyu S. H., et al., 2017, , 468, 2590
- Tegmark M., et al., 2004, , 69, 103501
- Tegmark M., et al., 2006, , 74, 123507
- Toomre A., Toomre J., 1972, in *Bulletin of the American Astronomical Society*. p. 214
- Treu T., Ellis R. S., Kneib J.-P., Dressler A., Smail I., Czoske O., Oemler A., Natarajan P., 2003, , 591, 53
- Valluri M., 1993, , 408, 57
- Vikhlinin A., et al., 2009, , 692, 1060
- Voges W., et al., 1999, , 349, 389
- Walter F., Brinks E., de Blok W. J. G., Bigiel F., Kennicutt Robert C. J., Thornley M. D., Leroy A., 2008, , 136, 2563
- Weisskopf M. C., Tananbaum H. D., Van Speybroeck L. P., O'Dell S. L., 2000, in Truemper J. E., Aschenbach B., eds, *Society of Photo-Optical Instrumentation Engineers (SPIE) Conference Series Vol. 4012, X-Ray Optics, Instruments, and Missions III*. pp 2–16 (arXiv:astro-ph/0004127), doi:10.1117/12.391545
- Wetzel A. R., Tinker J. L., Conroy C., 2012, , 424, 232

Wetzel A. R., Tinker J. L., Conroy C., van den Bosch F. C., 2013, , 432, 336

White S. D. M., Frenk C. S., 1991, , 379, 52

White S. D. M., Rees M. J., 1978, , 183, 341

Whitmore B. C., Gilmore D. M., 1991, , 367, 64

Yoon Y., Im M., 2020, , 893, 117

Yoon Y., Im M., Lee G.-H., Lee S.-K., Lim G., 2019, *Nature Astronomy*, 3, 844

York D. G., et al., 2000, , 120, 1579

2 Numerical models of Galaxy Formation

Simulations are a widely used tool in the fields of galaxy formation and cosmology. The pioneer works of Peebles 1970 and Toomre & Toomre 1972 proved that simulations were a useful tool to study the universe at different scales. From the formation of coma-like clusters to the formation of tidal arms as a product of major mergers, simulations became an appealing approach to understand some of the most complex processes of the Universe. Fueled by the need for testing and constraining a standard cosmological model, the interest in developing numerical models of the evolution of the observable Universe, with different prescriptions gained momentum. At this time, the growth of structures in the linear regime was well understood, but as we stated in the previous Chapter, when structures enter the non-linear regime the problem becomes an extremely complex one. This changed with the arrival of the formalism introduced in Press & Schechter 1974. Based on this framework, Davis et al. (1985) presented for the first time a model for the evolution of structures in the non-linear regime of a Universe dominated by Cold Dark Matter (CDM). Using N-body simulations, they studied the clustering of structures in universes constructed considering different cosmological parameters. These included a model of a Universe dominated by CDM with a positive cosmological constant. This places this work as the first simulation of the current standard cosmological model. Even though the parameters used for this simulation are not up to date, their study set the foundations of the following efforts to describe the evolution of the Universe within the current standard model, based purely on gravitational interaction. As such, N-body simulations have become the main pillar on which galaxy formation models are constructed. On these codes, the density field of a primordial volume of the Universe is discretely represented with a number of N particles. The system is then left to evolve by calculating the gravitational force exerted by each mass element over the others by solving the Poisson equation. These calculations are performed within a comoving volume, which is evolved forward in time in discrete time-steps, considering a periodic box. This latter assumption is used to represent the large-scale matter distribution.

Different methods can be employed in N-body solvers, each with its own advantages and disadvantages. In general, one can divide them between particle-based and particle-mesh based. From the particle-based methods, the most commonly used is the tree code (Barnes & Hut, 1986). Here, the volume is hierarchically subdivided into a number of cubic cells. At the lowest level of this hierarchy, each particle is enclosed within a given cell. For nearby particles, particle-particle interactions are computed. Due to the artificially coarse-grained discretisation of the system mass distribution, the gravitational force produces a singularity when the distance between two particles approaches zero. To circumvent this issue, a term is added to the calculation of force, named “force softening length”. This parameter dictates the minimum distance within which the forces can be reliably measured and is used to avoid unphysical accelerations during very close encounters. On the other hand, as the distance from a given particle significantly increases, the gravitational force from distant particles is treated collectively by merging their corresponding cubic cells into a larger unique volume element. The forces exerted from this larger and distant volume element is approximated through a multipolar expansion of its density distribution. Instead, particle-mesh methods particles the systems evolve under the influence of the potentials associated to cell grids, computed via Fast Fourier transformations of their density field. N-body particles move due to the influence of the combined gravitational potential field of all cells in the system (Hockney & Eastwood, 1988). Particle-mesh methods are considerably faster than particle-based methods but are limited to the resolution of their cell size, while particle-based methods accurately represent the forces down to the resolution of their softening length, but are more costly. Finally, a hybrid Tree-Particle-Mesh (Tree-PM) methodology have become popular in the last decades, in which the forces exerted by close particles are measured using a

tree while long-range forces are computed with a particle-mesh method (Springel, 2005).

The methods described above are meant to accurately model gravitational interactions. This type of interaction is sufficient when modelling the collisionless dark matter component of the Universe. The next step to study how galaxies evolve in a cosmological context is to consider how baryons in galaxies evolve as dark matter haloes collapse and grow. Within this context, two different approaches are commonly used to study galaxy formation. A direct multi-physics self-consistent approach in which baryons and dark matter are simulated self-consistently by solving both, hydrodynamical and gravitational equations (hydrodynamical simulations), and a serial approach in which first, only the growth of dark matter perturbations are simulated, and then the baryons are added in a phenomenological analytic fashion (semi-analytic simulations). Each method has its own advantages and limitations. In particular, the advantages in using hydrodynamical simulations reside in their attempt to reproduce the physics behind galaxy formation and evolution in a fashion as accurately as possible. Generally, hydrodynamical simulations are able to reproduce the dynamics of the gas, feedback from AGN, star formation and supernovae, radiative cooling and heating among other complex processes. Moreover, given the nature of their construction, hydrodynamical simulations directly reproduce the non-linear phenomenology experienced by the gaseous component of galaxies as some of the aforementioned processes act simultaneously. The disadvantage of this methodology lies in the computational time needed for the task. High-resolution hydrodynamical models of sections of the Universe with a box big enough to reproduce the biggest galaxy clusters could take millions of CPU hours and months to complete. For example, to simulate one of the galaxy clusters used on this Thesis, more than 10 million CPU hours were needed to reach $z = 0$. The calculation took over 10 months of total time to be completed. It is important to keep in mind that, even though with this method the dynamic of the gas can be well modelled, many physical mechanisms act on a scale below the resolution limit of the simulations. Thus, to model them, subgrid physic modules are needed.

On the other hand, semi-analytical models are, computationally, a much cheaper alternative to hydrodynamical simulations. Here, baryonic physics other than gravity is modelled using a phenomenological approach. To perform this type of modelling on galaxies, it is first needed to count with the evolutionary history of the potential well within which baryons will collapse. To do so, more recent models have used N-body dark matter only cosmological simulation to extract the growth history of a set of haloes. Then, a series of analytical prescriptions are applied over these catalogues in a post-processing fashion, to reproduce the observational properties of galaxies within and surrounding dark matter haloes. The strengths of this type of modelling reside in the low calculation times required to run these codes. This allows semi-analytical models to generate galaxy samples orders of magnitude larger than with hydrodynamical simulations. Also, it allows to change parameters of the model and rapidly see what are the effects that such changes could have on the population of galaxies, allowing an efficient parameter space exploration. Their disadvantages mainly reside in the great number of free parameters used for the model, and on how dependant observable properties of galaxies could be on the modelling of specific physical phenomena. In general, the results obtained by both models are in good agreement, at least for observables that lie above the resolution limit of the simulations. For the purpose of this Thesis, we will use hydrodynamical simulations as a tool to understand the fate of galaxies as they transition from one environment to another. We will take advantage of their sophistication level and their ability to resolve the dynamics of baryons to characterize the impact that these transitions have in the galaxies' gas and stellar content.

In the following subsections, we will discuss the models used for this purpose and why they are well suited to develop this Thesis.

Cosmological parameter	Value
Ω_m	0.307
Ω_Λ	0.693
Ω_b	0.04825
$h \equiv H_0/(100\text{km s}^{-1}\text{Mpc}^{-1})$	0.6777
σ_8	0.8288
n_s	0.9611
Y	0.248

Table 2.1: Cosmological parameters used in all the EAGLE simulation suite. Ω_m , Ω_Λ and Ω_b correspond to the matter density, dark energy density and baryonic density respectively; h is the normalized Hubble parameter; σ_8 is the square root of the linear variance of the matter distribution when smoothed with a top-hat filter of radius $8h^{-1}\text{cMpc}$ and n_s is the scalar power-law index of the power spectrum of primordial adiabatic perturbations, and Y is the primordial abundance of helium. Credit: Table 1 extracted from Schaye et al. 2015.

Name	L (cMpc)	N	$m_g(\text{M}_\odot)$	$m_{\text{dm}}(\text{M}_\odot)$	$\epsilon_{\text{com}}(\text{c kpc})$	$\epsilon_{\text{prop}}(\text{pkpc})$
L025N03767	25	376^3	1.81×10^6	9.70×10^6	2.66	0.70
L025N0752	25	752^3	2.26×10^5	1.21×10^6	1.33	0.35
L050N0752	50	752^3	1.81×10^6	9.70×10^6	2.66	0.70
L100N1504	100	1504^3	1.81×10^6	9.70×10^6	2.66	0.70

Table 2.2: Specifications from all the simulations of the EAGLE suite. From left to right the columns show the simulation name suffix; comoving box size; the number of initial baryonic and dark matter particles; initial gas-particle mass; dark matter particle mass; Plummer-equivalent gravitational softening length in comoving kiloparsec and maximum proper softening length. Credit: Table 2 extracted from Schaye et al. 2015

2.1 EAGLE Simulation

In a substantial part of this Thesis, we will analyze data from the Evolution and Assembly of GaLaxies and their Environments (EAGLE) project from the Virgo Consortium (Schaye et al., 2015). This state-of-the-art suite of hydrodynamical cosmological simulations corresponds to one of the first of its kind to be in good agreement with semi-analytic models and with observations of several observable that were not considered in the model calibration process.

The EAGLE simulation suite was run using a Smoothed-Particle-Hydrodynamics (SPH) solver called ANARCHY; a modified version of GADGET 3 which is a fairly improved version of the N-Body Tree-PM smoothed particle hydrodynamics code GADGET 2 Springel (2005). The improvements lie in the use of the pressure-entropy formulation of the SPH presented in Hopkins (2013), the time-step limiters introduced in Durier & Dalla Vecchia (2012), the artificial viscosity switch proposed in Cullen & Dehnen (2010) and a weak thermal conduction term as proposed in Price (2008).

All the simulations were ran adopting a Λ CDM cosmology, with the cosmological parameters based on the results of the Planck Mission (Planck Collaboration et al., 2014, see Chapter 1). The values

Prefix	$n_{H,0}(\text{cm}^{-3})$	n_n	C_{visc}	$\Delta T_{AGN}(\text{K})$
Ref	0.67	$2/\ln 10$	2π	$10^{8.5}$
Recal	0.25	$1/\ln 10$	$2\pi \times 10^3$	10^9
AGNdT9	0.67	$2/\ln 10$	$2\pi \times 10^2$	10^9

Table 2.3: Differences on the values of the subgrid physic that varies between the models, where $n_{H,0}$ and n_n parameters control the energetic feedback from star formation by being the dependence on the characteristic density and the power-law slope of the density dependence respectively. C_{visc} controls the sensitivity that the Black Hole accretion rate has on the angular momentum of the accreted material and ΔT_{AGN} is the temperature increase of the gas due to AGN feedback. Credit: Table 3 extracted from Schaye et al. 2015

for the parameters are listed in Table 2.1. The simulation suite was run over three cubic periodic volumes with a box-length side of 25, 50 and 100 comoving megaparsecs (cMpc) as detailed in Table 2.2. Baryonic and non-baryonic particles are followed from redshift $z = 127$ to the present day. The initial conditions were generated following a second-order Lagrangian perturbation theory, using the method stated in Jenkins (2010) and the public white noise field from *Panphasia* (Jenkins & Booth, 2013; Jenkins, 2013).

For those processes that act beyond the resolution limit of the simulation, either in mass or time, subgrid models were implemented. These only depend on the local hydrodynamic properties and are design to be as simple as possible. This factor differentiates EAGLE from other hydrodynamical simulations. By choosing subgrid models to be dependant only on the local hydrodynamics, the model is capable to develop, for example, galactic winds without any pre-determined mass loading factors and directions, and without a direct dependence on the properties of the dark matter halo. The subgrid model used in the simulation is a modification of the code developed for the Overwhelmingly Large Simulations project (Schaye et al., 2010, OWLS), used in the Galaxies-intergalactic medium interaction calculation (Crain et al., 2009, GIMIC) and the extension of the OWLS project referred to as cosmo-OWLS (Le Brun et al., 2014) as well. Among the modifications of the model are the implementation of energy feedback from star formation, the accretion of gas into black holes, and a star formation law that now depends on the metallicity as well. For a detailed description of the model, please refer to section 4 of Schaye et al. (2015).

Radiative cooling and photo-heating are implemented for eleven chemical elements: H, He, C, N, O, Ne, Mg, Si, S, Ca, and Fe, in an element-by-element fashion, following Wiersma et al. (2009a). The simulation also takes into account the time-dependant stellar mass loss due to winds from giant stars, core-collapse and type Ia supernovae following Wiersma et al. (2009b). Star formation is implemented stochastically following the methodology presented in Schaye & Dalla Vecchia (2008), which reproduces the pressure-dependent Kennicutt-Schmidt relation (Kennicutt, 1998). A metal-dependent star formation threshold was added, proposed in Schaye (2004), in order to track the transition from warm atomic gas to the unresolved cold molecular gas. Each stellar particle created during a star formation event is assumed to be a single age stellar population, with a Chabrier initial mass function in the range $0.1M_{\odot} - 100M_{\odot}$ (Chabrier, 2003). The feedback product of the star formation event is implemented stochastically following the method proposed by Dalla Vecchia & Schaye (2012). Here the amount of feedback energy injected in the medium per unit of stellar mass decreases with metallicity and increases with the gas density. Black holes are seeded at the centre of haloes with a total mass greater than $10^{10}M_{\odot}/h$ and then tracked following the methodology described in Springel et al.

(2005). Gas accretion into black holes is described using a modification of the Bondi-Hoyle accretion rate, while AGN feedback is implemented stochastically, following the methodology described in Schaye et al. (2015).

The model was calibrated against observations using a series of high and intermediate resolution simulations in boxes of 12.5 cMpc and 25 cMpc respectively. For the subgrid physics model implemented in EAGLE, the most relevant parameters to be calibrated are those related to energetic feedback. The combination of parameters that better reproduced the $z = 0$ galaxy stellar mass function was chosen as the reference model. Within the project, the prefix “Ref-” is used to identify simulations run with this subgrid model. Additionally, a 25 cMpc and a 50 cMpc boxes were run with two slightly different subgrid models. Given the stochastic implementation of thermal feedback used in EAGLE, convergence with respect to numerical resolution is not expected within this model. Thus, when changing the resolution of the simulations, a recalibration of the free parameters on the feedback implementation is needed. In particular, those related to local densities. The prefix “Recal-” is used to identify the simulations performed with the re-calibrated subgrid model used in the 25 cMpc high-resolution box. Finally, a 50 cMpc intermediate size box was re-run with a modification of the AGN feedback parameter. The gas content of massive groups and clusters in the Ref-L100N1504 simulation (following the nomenclature described in Tables 2.1 and 2.2) showed some discrepancies concerning the observed gas mass in these types of objects, inferred from X-ray observations. This discrepancy served as a motivation to perform an update of the parameter regulating AGN feedback (Schaye et al. (2015)). As a result of these modifications, a more realistic sampling of the ICM is achieved. The resulting model is referred to as “AGNdT9” and will be particularly relevant in the following sections. The main differences between the parameters chosen for each model are listed in table 2.3. In Chapter 3 of this thesis, I analyzed the Ref-L100N1504 simulation, which corresponds to the largest box available in the suite. This simulation is the only one in the suite which includes the galaxy clusters needed to understand the astrophysical processes behind cluster satellite’s quenching.

In order to create the group catalogues, the overdensities in dark matter were detected using a “Friend-of-Friends” algorithm (FoF, Davis et al., 1985), with a linking length of 0.2 times the mean inter-particle spacing. Baryonic particles are associated to a FoF halo based on the membership of their closest DM particle. Self-bound structures inside FoF selected haloes, referred to as “subhaloes” or “Sub-Groups”, are later identified using the SUBFIND algorithm (Springel et al., 2001; Dolag et al., 2009). It should be noted that particles are not shared between subhaloes, so the correspondence between particles and subhaloes is unique. As each FoF group could contain several subhaloes, a central subhalo is defined based on the subhalo that contains the dark matter particle with the lowest value of binding energy. All other subhaloes present in the FoF will be referred to as “satellites”.

Merger trees from the simulation are a key aspect in the development of this thesis, as they allow us to follow both, the evolution of the cluster and the evolution of the satellites that are accreted for the cluster and survive until $z = 0$. For each simulation of the EAGLE project 29 snapshot outputs, between redshift 20 and 0, were stored, with a time resolution ranging from 0.3 to 1Gyr. The “subhalo” catalogues obtained in the post-processing using SUBFIND are linked through time via a galaxy merger tree (Jiang et al., 2014; Qu et al., 2017). This allows us to study the evolution of individual galaxies. This algorithm looks for the descendants of the subhaloes through the identification of the subhalo in the subsequent snapshot that shares the majority of the most bound particles with the progenitor. Each galaxy could have many progenitors but only one descendant defined as above. For the most massive branch of each galaxy tree, a “main progenitor” is defined, and is treated as the evolutionary history of a particular galaxy.

2.2 Cluster-EAGLE project

An important limitation of the EAGLE simulation suite relates to the cluster sample. Even the largest simulation box has only 10 available clusters and the most massive system has a total mass $M_{200} \sim 5 \times 10^{14} M_{\odot}$; i.e. there are no massive clusters available. Within this context, and with the goal to subside this limitation, the Cluster-EAGLE simulation project is born (C-EAGLE) (Bahé et al., 2017; Barnes et al., 2017b). This is a suite of cosmological hydrodynamical zoom-in simulations of the formation of 30 galaxy clusters in a mass range between $10^{14} < M_{200}/M_{\odot} < 10^{15.4}$. The haloes selected to be re-simulated with the zoom-in technique (Katz & White, 1993; Tormen et al., 1997), were chosen from a low-resolution parent simulation. The parent simulation posses a periodic cube with a side length of 3.2 cGpc and a number $N = 2520^3$ of dark matter particles, described in Barnes et al. 2017a. The parent simulations use the cosmological parameters measured by *Planck Mission* Planck Collaboration et al. 2014, the same used in the EAGLE simulation (see Table 2.1 for the values used).

Given the large size of the box, many clusters can be found in this simulation. For example, at $z = 0$ there are 185150 clusters available with $M_{200} > 10^{14} M_{\odot}$, and 1701 with $M_{200} > 10^{15} M_{\odot}$. To select haloes to re-simulate, first, the whole sample of available clusters in the DM simulation were binned in 10 evenly spaced log mass bins within the mass range of $14.0 \leq \log_{10}(M_{200}/M_{\odot}) \leq 15.4$. This was done to avoid a bias in the sample of re-simulation cluster candidates towards lower mass structures, given the steep slope in the mass function. Secondly, each halo should fulfil an isolation criterion to ensure that selected objects are the focus of the computational resources. In that sense, all haloes with a more massive neighbour within a radius of $30Mpc$ or $20r_{200}$ (the larger value between this two) were subtracted from the sample. Finally from the remaining clusters, 3 random haloes were selected per mass bin, leaving a total sample of 30 galaxy clusters to be re-simulated. The high-resolution region was defined such that it covers at least $5r_{200}$. For 24 of the 30 clusters in the sample, a Lagrangian region of $10r_{200}$ was selected. This was done to study the impact that the environment has on galaxy evolution as its changes from the low-density field to galaxy clusters. This sub-sample was introduced in Bahé et al. 2017 as the *Hydrangea* simulation. The remaining 6 clusters were introduced in Barnes et al. 2017b and cover a high-resolution region of $5r_{200}$.

The initial conditions were generated following the same procedure explained above for the EAGLE simulation (see Section 2.1 for a detailed explanation). The mass particle in the high-resolution region was chosen to match the properties of the largest box in the EAGLE simulation (Ref-L100N1504). Each gas particles had an initial mass of $m_{gas} = 1.8 \times 10^6 M_{\odot}$ and each dark matter particle had a mass of $m_{DM} = 9.1 \times 10^6 M_{\odot}$. The gravitational softening length was set to 2.66 comoving kpc for $z > 2.8$ and then fixed to 0.70 physical kpc at $z < 2.8$.

The galaxy formation model used to run the zoom-in simulations is the same as in the EAGLE simulations (see Section 2.1 for details). As we mentioned in Section 2.1 the previous section, in Schaye et al. 2015 three slightly different subgrid models were presented (REF, AGNdT9 and Recal). Their differences are listed in Table 2.3. After testing the three models, the one that showed a better fit to the X-ray luminosity-temperature relation was chosen for the highest resolution re-simulations. Since the EAGLE simulation does not count with massive clusters, the fit to the X-ray luminosity-temperature relation was tested in the range of low-mass groups ($M_{500} < 10^{13.5} M_{\odot}$). With this in mind, the parameters associated with the ‘‘AGNdT9’’ model were selected as the fiducial set for the C-EAGLE project, including the *Hydrangea* sub-sample. The main purpose behind the EAGLE calibration of the subgrid model was to reproduce the properties of observable galaxies. Unfortunately, since the calibration was performed within a cubic box of 50c Mpc, there is no information on how well-calibrated this model is in the scale of massive galaxy clusters. Nevertheless, for the C-EAGLE simulations it was chosen

to keep the parameters as in Schaye et al. (2015), instead of re-calibrating the model. Given these considerations, the properties of the intracluster medium in the C-EAGLE simulation are a prediction from a model calibrated to produce realistic galaxies in the field.

The main outputs from each simulated cluster were stored in 30 “full” snapshots between $z = 14$ and $z = 0$. For 28 of those snapshots, a $\Delta t = 500$ Myr was chosen to keep them as equidistant as possible. Two additional snapshots were added at $z = 0.366$ and $z = 0.101$ to facilitate a direct comparisons with the EAGLE simulations. As a result, a total of 12 snapshots can be directly compared between EAGLE and C-EAGLE simulation. Additionally, several “snipshots” were stored containing only the most relevant information for each particle such as position and velocities, all in between the aforementioned snapshots with a $\Delta t = 125$ Myr. Between three different intervals in lookback time (0-1, 4-5 and 7-8 Gyr), the time resolution for these snipshots was increased to $\Delta t = 25$ Myr.

As in the EAGLE project, the outputs were post-processed by identifying substructures present at each snapshot using the *subfind* code (Springel et al., 2001; Dolag et al., 2009). This was conducted following the same procedure described in the previous Section 2.1. To trace in time the formation history of individual haloes a merger tree algorithm was implemented, in a similar fashion to what was described for the EAGLE simulation. However, to construct the trees the SPIDERWEB algorithm was applied. This algorithm was specifically designed for these simulations and works following galaxies through time by detecting subhaloes in subsequent snapshots that share the highest fraction of particles. Even though this approach is similar to what is done for other tree algorithms, SPIDERWEB was designed with the purpose of identifying descendants for as long as possible in crowded environments. It takes into account those instances when a galaxy could temporarily disappear from the SUBFIND catalogue, and attempts to reconnect those lost galaxies by looking after them for up to 2.5 Gyr. This improves the treatment of mergers in SPIDERWEB with respect to previous tree algorithms, such as Rodriguez-Gomez et al. 2015; Qu et al. 2017, as well as the detection of galaxies as they pass through the cores of galaxy clusters. In practice, SPIDERWEB considers multiple descendant candidates for each subhalo at given snapshot i . First, any subhalo in the subsequent snapshot $i + 1$ who shares at least one particle with a given subhalo in the snapshot i will be considered as a “descendant candidate”. Secondly, the candidates are sorted by priority, where the highest rank is given to the halo that shares the highest amount of particles belonging to the 5% most bound non-collisional particles with the subhalo at snapshot i . All candidates are stored as a backup, in case that the highest-ranked link leads to a subhalo in the snapshot $i + 1$ that already presents a better agreement with another galaxy at snapshot i . This becomes particularly important when galaxies are undergoing mergers where most of the core particles of a galaxy could be transferred from one subhalo to another.

2.2.1 The role of simulations on this Thesis

The goal of this thesis is to understand where, when and how the satellites of galaxy clusters cease their star formation. To do that, we analyze the catalogues provided by the EAGLE and C-EAGLE projects. In Chapter 3 of this thesis, we used the catalogues from an EAGLE public database, presented by McAlpine et al. 2016, to characterize the evolution of the satellite population of the galaxy clusters available in the simulation. We considered clusters in the largest box with an intermediate resolution, dubbed Ref-L100N1504. Clusters were defined as all those FoF haloes with a mass greater than $\log_{10}M_{200}/M_{\odot} \gtrsim 14$. In particular, in the EAGLE simulation, ten galaxy clusters massive enough to satisfy this threshold were found.

From those clusters all subhaloes that are, *i*) surviving satellites at $z = 0$, *ii*) contain a stellar mass greater than $\log_{10}M_{200}/M_{\odot} \gtrsim 8$ and *iii*) a total mass greater than $\log_{10}M_{200}/M_{\odot} \gtrsim 9$ were selected. This ensures that all studied galaxies in our work are modelled with at least 1000 DM particles. We

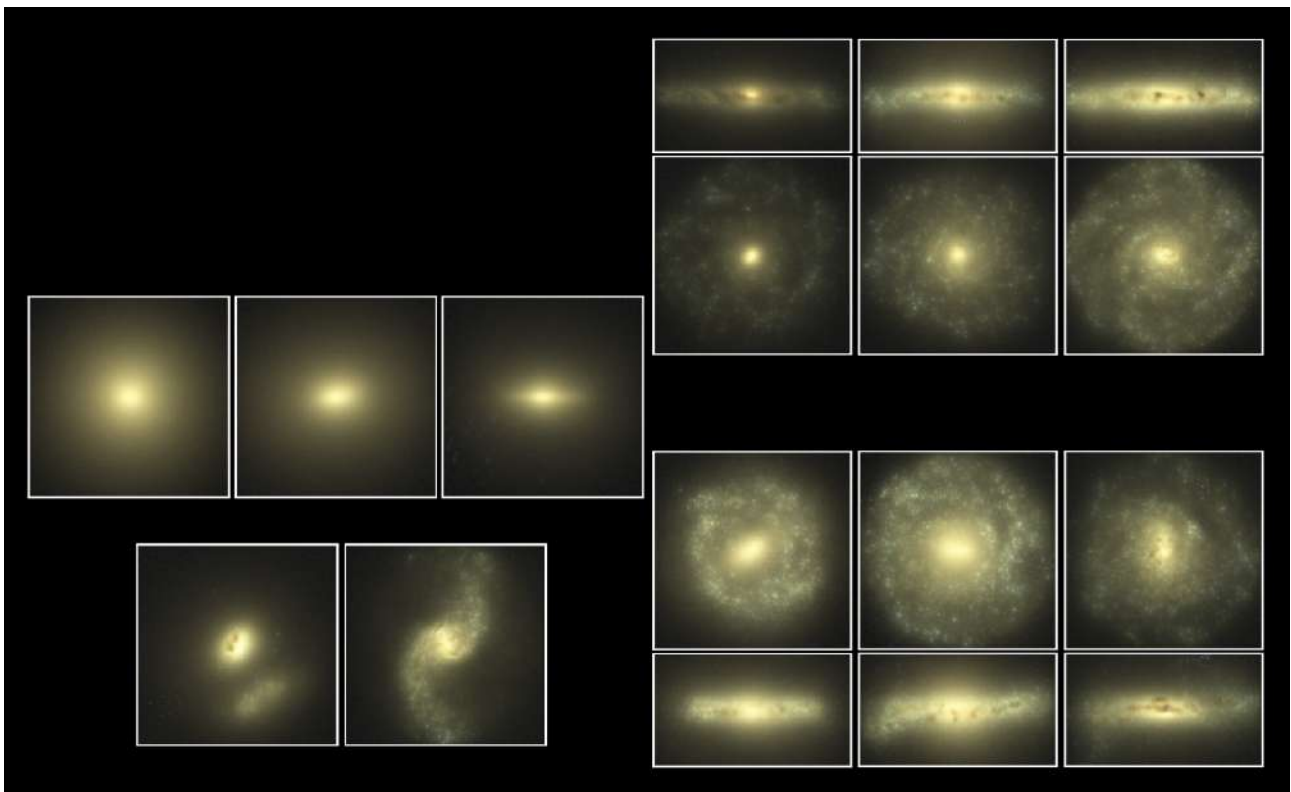


Figure 2.1: Illustrative sample of galaxies showing the Hubble sequence, using galaxies present in the Ref-L100N1504 EAGLE simulation. Images are made using a composition of the monochromatic u,g and r band SDSS filters, accounting for dust extinction. Each image has a 60ckpc of side. Image extracted from Schaye et al. 2015 *Credit: James Trayford*

defined as satellites all those galaxies that are gravitationally bound to the cluster at $z = 0$ and can be found inside the R_{200} . From this definition, we exclude the central halo of each cluster. We also defined their accretion time as the snapshot in which the galaxies are found evolving inside the cluster R_{200} for the first time.

The EAGLE project is a perfect laboratory for the first stage of this project. As shown in Schaye et al. 2015, the EAGLE simulation has been successful in reproducing not only a wide variety of morphologies, as seen in Figure 2.1, but several observational properties that were not directly calibrated. Examples are the Tully-Fisher relation, the column density distribution of C IV and O VI, the column density distribution of intergalactic metals (Schaye et al., 2015), the H I and H₂ properties of galaxies (Lagos et al., 2015; Bahé et al., 2016) and the luminosity function and colour-magnitude diagram for galaxies at $z = 0$ (Trayford et al., 2015). Moreover, as is shown in Furlong et al. 2015 and Furlong et al. 2017, the EAGLE simulation have been successful at reproducing the stellar mass function, the size-mass relation and the star formation main sequence in a wide range of satellite masses. This is particularly important for our analysis, given that most of our results will be related to the specific star formation rates of galaxies.

On the other hand, in Chapter 4 we used the C-EAGLE simulation project to disentangle the physical mechanisms behind the quenching of the star formation. By using the same definitions of galaxies and quenching used in Chapter 3, we characterized the local environment in which galaxies get quenched. We measure the ram pressure experienced by galaxies at their quenching time and compare them with the restoring force per unit of area exerted by the galaxy itself. By comparing the ratio between these two quantities, we were able to define the moment when galaxies become ram pressure dominated and explore its link with their quenching time. We characterized the dependence of our results with redshift and found that galaxies get quenched inside the first massive halo in which they reside.

The C-EAGLE project addresses some of the caveats present in the EAGLE project. With the available sample of high mass clusters, the C-EAGLE simulations allow us to follow the formation history of cluster satellite's residing on structures that range from groups to the most massive bound structures in the Universe. Also, thanks to the improved calibration of the subgrid model galaxies in clusters, in particular, the most massive ones, are well characterized even in the crowded cluster centre. In this sense, cluster properties in the C-EAGLE simulations are a prediction of a model that produces reasonably realistic field galaxies. On Barnes et al. 2017b is shown that the C-EAGLE simulations successfully reproduce the same observables as the EAGLE project, without the need for recalibration of the subgrid model to cluster-mass structures. Moreover, the simulated clusters reproduce with a good agreement the observed gas fraction - total mass relation and provide a good match between the gas temperature - cluster mass relation. For the development of this project, simulations capable of reproducing with a good agreement the ICM since the formation of the clusters are key to characterize the local environment in which galaxies reside and the impact that it could have in the star formation of galaxies.

Bibliography

Bahé Y. M., et al., 2016, , 456, 1115

Bahé Y. M., et al., 2017, , 470, 4186

Barnes J., Hut P., 1986, , 324, 446

Barnes D. J., Kay S. T., Henson M. A., McCarthy I. G., Schaye J., Jenkins A., 2017a, , 465, 213

Barnes D. J., et al., 2017b, , 471, 1088

Chabrier G., 2003, , 115, 763

Crain R. A., et al., 2009, , 399, 1773

Cullen L., Dehnen W., 2010, , 408, 669

Dalla Vecchia C., Schaye J., 2012, , 426, 140

Davis M., Efstathiou G., Frenk C. S., White S. D. M., 1985, , 292, 371

Dolag K., Borgani S., Murante G., Springel V., 2009, , 399, 497

Durier F., Dalla Vecchia C., 2012, , 419, 465

Furlong M., et al., 2015, , 450, 4486

Furlong M., et al., 2017, , 465, 722

Hockney R. W., Eastwood J. W., 1988, Computer simulation using particles

Hopkins P. F., 2013, , 428, 2840

Jenkins A., 2010, , 403, 1859

Jenkins A., 2013, , 434, 2094

Jenkins A., Booth S., 2013, arXiv e-prints, p. arXiv:1306.5771

Jiang L., Helly J. C., Cole S., Frenk C. S., 2014, , 440, 2115

Katz N., White S. D. M., 1993, , 412, 455

Kennicutt Jr. R. C., 1998, , 498, 541

Lagos C. d. P., et al., 2015, , 452, 3815

Le Brun A. M. C., McCarthy I. G., Schaye J., Ponman T. J., 2014, , 441, 1270

McAlpine S., et al., 2016, *Astronomy and Computing*, 15, 72

Peebles P. J. E., 1970, , 75, 13

Planck Collaboration et al., 2014, , 566, A54

- Press W. H., Schechter P., 1974, , 187, 425
- Price D. J., 2008, *Journal of Computational Physics*, 227, 10040
- Qu Y., et al., 2017, , 464, 1659
- Rodriguez-Gomez V., et al., 2015, , 449, 49
- Schaye J., 2004, , 609, 667
- Schaye J., Dalla Vecchia C., 2008, , 383, 1210
- Schaye J., et al., 2010, , 402, 1536
- Schaye J., et al., 2015, , 446, 521
- Springel V., 2005, , 364, 1105
- Springel V., White S. D. M., Tormen G., Kauffmann G., 2001, , 328, 726
- Springel V., Di Matteo T., Hernquist L., 2005, , 361, 776
- Toomre A., Toomre J., 1972, in *Bulletin of the American Astronomical Society*. p. 214
- Tormen G., Bouchet F. R., White S. D. M., 1997, , 286, 865
- Trayford J. W., et al., 2015, , 452, 2879
- Wiersma R. P. C., Schaye J., Smith B. D., 2009a, , 393, 99
- Wiersma R. P. C., Schaye J., Theuns T., Dalla Vecchia C., Tornatore L., 2009b, , 399, 574

3 Tracing the Quenching History of Cluster Galaxies in the EAGLE Simulation

Summary*

In this Chapter we use the EAGLE hydrodynamical simulation to trace the quenching history of galaxies in the 10 most massive clusters. We use two criteria to identify moments when galaxies suffer significant changes in their star formation activity: *i*) the instantaneous star formation rate (SFR) strongest drop, $\Gamma_{\text{SFR}}^{\text{SD}}$, and *ii*) a “quenching” criterion based on a minimum threshold for the specific SFR of $\lesssim 10^{-11} \text{yr}^{-1}$. We find that a large fraction of galaxies ($\gtrsim 60\%$) suffer their $\Gamma_{\text{SFR}}^{\text{SD}}$ outside the cluster virial radius. This “pre-processed” population is dominated by galaxies that are either low mass and centrals or inhabit low mass hosts ($10^{10.5} M_{\odot} \lesssim M_{\text{host}} \lesssim 10^{11.0} M_{\odot}$). The host mass distribution is bimodal, and galaxies that suffered their $\Gamma_{\text{SFR}}^{\text{SD}}$ in massive hosts ($10^{13.5} M_{\odot} \lesssim M_{\text{host}} \lesssim 10^{14.0} M_{\odot}$) are mainly processed within the clusters. Pre-processing mainly limits the total stellar mass with which galaxies arrive in the clusters. Regarding quenching, galaxies preferentially reach this state in high-mass halos ($10^{13.5} M_{\odot} \lesssim M_{\text{host}} \lesssim 10^{14.5} M_{\odot}$). The small fraction of galaxies that reach the cluster already quenched has also been pre-processed, linking both criteria as different stages in the quenching process of those galaxies. For the $z = 0$ satellite populations, we find a sharp rise in the fraction of quenched satellites at the time of first infall, highlighting the role played by the dense cluster environment. Interestingly, the fraction of pre-quenched galaxies rises with final cluster mass. This is a direct consequence of the hierarchical cosmological model used in these simulations.

*Based on Pallero et al. (2019), published in MNRAS

3.1 Introduction

As we stated in Chapter 1, since the first half of the twentieth century, it has been known that colors reflect the predominant stellar populations in galaxies and that they are related to their morphology (Morgan & Mayall, 1957). The colour-morphology (Roberts & Haynes, 1994) and color-magnitude relations (Chester & Roberts, 1964; Faber, 1973) are now widely used to study the properties of galaxies. As a result, rather than selecting objects according to their *early*- or *late-type* morphology, galaxies can be separated between *red* and *blue*, which naturally relates with their star formation and metal-enrichment history. Studies in the local universe show that, in general, galaxies present a strong bimodal color distribution (Strateva et al., 2001; Baldry et al., 2006; Cassata et al., 2008), regardless of the environment in which they reside (Hogg et al., 2004; Baldry et al., 2006). Reproducing this bimodality, and understanding the role played by the environment, has become an important goal for galaxy-evolution theories (Trayford et al., 2015; Nelson et al., 2018).

One of the first indications that the environment plays a fundamental role in driving the evolution of galaxies was the morphology-density relation (Dressler, 1980, 1984). Observational studies have shown that in high density environments there is a greater fraction of galaxies with early-type morphology than in low density environments, and that the fraction of early-type galaxies in clusters rises toward the cluster’s center (Brough et al., 2017; Cava et al., 2017).

In addition, several studies during the last decades have shown that dense environments can also affect the star formation history of galaxies (Gunn & Gott, 1972; Dressler, 1980; Moore et al., 1996; Poggianti et al., 2001; Boselli et al., 2005). Naturally, the cores of galaxy clusters are an ideal laboratory to study how the environment affects the evolution of galaxies in dense regions and at different redshifts (Cayatte et al., 1990; Smail et al., 1997; Bravo-Alfaro et al., 2000; Boselli et al., 2005). Evidence of global transformations for galaxies over time is given by the increasing fraction of spiral in clusters up to $z \sim 0.5$ (Dressler et al., 1997; Fasano et al., 2000; Desai et al., 2007), and thanks to the fact that high- z clusters are observed to contain more star-forming galaxies compared to present-day (Butcher & Oemler, 1984; Poggianti et al., 2006).

It is also well known that there are differences between the properties of galaxies located in the inner and outer regions of galaxy clusters. Some authors (Kodama et al., 2001; Treu et al., 2003), suggest that this is the result of a variety of mechanisms that act at different distances from the cluster center, driving galaxy evolution with different timescales. Moreover, it has been observed (e.g. Dressler et al. 2013; Hou et al. 2014; Bianconi et al. 2018) that in the outskirts of clusters infalling galaxy partly distribute in the form of groups.

Theoretical works (e.g. McGee et al. 2009; De Lucia et al. 2012) suggest that $\sim 25 - 40\%$ of galaxies belonging to a massive cluster ($M_{\text{halo}} \sim 10^{14.5} - 10^{15.0} [M_{\odot}]$) at $z = 0$ have been accreted in such groups. For the aforementioned reasons, the study of galaxy properties in cluster outskirts, where these systems are still assembling, has attracted the interest of several astronomers (e.g. Just et al. 2010; Cybulski et al. 2014; Jaffé et al. 2016). In particular, some authors (e.g. Hou et al. 2014; Haines et al. 2015; Bianconi et al. 2018) have studied the variation of the fraction of quiescent galaxies with the projected distance from the centers of clusters, finding that out to $3R_{200}$ clusters are richer in passive galaxies than the field. These results can only be explained if star formation was quenched in galaxies prior to their accretion on to clusters, when they were still members of in-falling groups (pre-processing Zabludoff & Mulchaey 1998; Fujita 2004). The fact that galaxies are “preprocessed” in groups before their accretion on to clusters shows that groups of galaxies constitute an important piece in the physics of galaxy formation and evolution, because the processes that take place within them may significantly alter star formation and change the structural and chemical properties of galaxies. Groups provide, then, further laboratories to study the environmental drivers of galaxy evolution (e.g.

Dressler et al. 2013; Bianconi et al. 2018; Olave-Rojas et al. 2018).

At $z \sim 0$, the specific star-formation rate of galaxies in dense environments is significantly lower than in lower density regions (Hashimoto et al., 1998; Lewis et al., 2002; Kauffmann et al., 2004; Gray et al., 2004; Balogh et al., 2007). Additionally, higher fractions of quiescent or passive galaxies are found in dense regions (Poggianti et al., 1999; Baldry et al., 2006; van den Bosch et al., 2008; Gavazzi et al., 2010; Haines et al., 2013). These studies also provide evidence that the star-forming activity and galaxy morphology can be correlated with $z \sim 0$ galactic stellar mass. Less massive galaxies also are more susceptible to environmental effects, indicating that the quenching of star formation can be accelerated in dense environments (De Lucia et al., 2012; Muzzin et al., 2012; Jaffé et al., 2016).

In spite of the observed relation between environment and cessation of star formation activity, i.e. “*environmental quenching*”, it is important to take into account internal process that can drive galaxy quenching. This process, known as “*mass quenching*” or “*internal quenching*”, can arise as a result of, e.g. internal gas consumption, supernova and AGN feedback, star formation feedback or halo gas heating (see e.g. Peng et al. 2010, Efstathiou 2000, Croton et al. 2006, Dekel & Birnboim 2008, Cantalupo 2010). The dominance of one way over the other is where the dichotomy of “*nature versus nurture*” was born, and has been one of the main subjects of study for extragalactic astronomy in the last years.

According to Oesch et al. (2016), quenching may start shortly after the first appearance of the galaxies, at roughly $z \sim 11$, but the environment does not play an important role until $z \sim 1.6$, with the environmental quenching efficiency rising by a factor of ~ 3.5 between $z \sim 1.6$ and $z \sim 0.9$. The quenching efficiency is defined as the ratio between passive galaxies in clusters and passive galaxies in the field, quantifying the number of galaxies that would be star-forming if they were in the field (Peng et al., 2010, 2015; Nantais et al., 2016). Nevertheless, a study of the sSFR and the fraction of star-forming galaxies in clusters at $z \sim 1$ from the GCLASS survey (Muzzin et al., 2012) shows that mass quenching dominates over environmental quenching, at least at this redshift. Balogh et al. (2016), using another cluster sample from GCLASS, found that the mechanisms driving the quenching at $z > 1$ may be different from those at $z \sim 0$. On the one hand, at high redshift, the cessation of star formation is mainly driven by a combination of gas consumption (due to an enhancement of star formation) and gas outflows as a result of supernovae and AGN feedback. On the other hand, at low redshift, dynamical mass removal mechanisms (due to environment) may be the main driver for the quenching of galaxies in clusters.

A detailed description of the main mechanisms that lead to environmental quenching is provided in Section 1.4. We can separate these mechanisms in three broad categories:

- Gravitational interactions between galaxies: Mergers can change drastically the star formation history of galaxies, as well as their morphology and kinematics. This phenomenon is usually observed in low-density environment such as groups of galaxies. In high-density environments, galaxies can experience harassment from other cluster members, through fast and aggressive encounters (Toomre & Toomre, 1972; Barnes & Hernquist, 1996; Walker et al., 1996; Moore et al., 1999);
- Interactions between galaxies and the intra-cluster medium: Ram-pressure from the intracluster medium can strip the gas of the galaxies and remove their interstellar medium (Gunn & Gott, 1972; Abadi et al., 1999; Quilis et al., 2000; Vollmer et al., 2001; Jaffé et al., 2015; Benítez-Llambay et al., 2013);
- Gravitational interactions between clusters and galaxies: The tremendous gravitational potential of the cluster can perturb some observable properties of the members, inducing gas inflows,

forming bars, compressing the gas or concentrating the star formation (Miller, 1986; Byrd & Valtonen, 1990; Boselli & Gavazzi, 2006).

It is precisely because of this complex nature of the environmental quenching that it is difficult to separate the aforementioned processes. It is expected that, at least, some of these processes act simultaneously and that they are effective in different overlapping regions of the cluster. Some studies show that the effectiveness of these processes is linked to the galaxy's cluster-centric distance (Moran et al., 2007).

A good approach to study the mechanisms that impact galaxy evolution is through cosmological models (Fujita, 2004; Wetzel et al., 2013; Vijayaraghavan & Ricker, 2013; Schaye et al., 2015; Nelson et al., 2018). Several works have used simulations to understand the properties of galaxies in different environments, and how their evolutionary history results in changes of their properties such as colors, stellar mass and star formation rate (Trayford et al., 2015, 2016; Katsianis et al., 2017; Tescari et al., 2018; Nelson et al., 2018). Hydrodynamical simulations can be used to define and test different criteria that can be used to understand the processes that drive galaxies to be quenched. Simulations also allow us to follow the evolution of galaxies in different environments and the evolution of their properties from $z \sim 20$ to $z = 0$. Since clusters at $z > 1.5$ are difficult to detect, due to the fact that they are still in an assembling process, simulations are a helpful tool to study the role that the environment plays at such high redshift (see e.g. Overzier 2016).

In this chapter, we use the public database from the state-of-the-art EAGLE hydrodynamic simulations (Schaye et al., 2015; Crain et al., 2015; McAlpine et al., 2016) to trace the evolution history of the satellite galaxies that belong to the ten most massive clusters at $z \sim 0$. We aim at identifying the environment in which galaxies preferentially cease their star formation and signatures that could be used to determine the main physical mechanism leading to the cessation of star formation of cluster satellite galaxies. We compare the results obtained from two different criteria to identify when star formation in galaxies significantly drops. The hydrodynamic simulations of the EAGLE project are perfectly suited for this study since they provide the possibility to study the evolution of galaxies and their properties.

This Chapter is organized as follows: in Section 2 we describe the EAGLE simulation, its main characteristics and the main potentialities that it provides for this study. In Section 3 we define the two criteria used in this work to locate those moments when galaxies suffer an important variation in their star formation; in Section 4 we describe the results obtained using our two approaches, putting special interest on the environment where these events take place. Finally, in Section 5 we summarize our main conclusions and compare our results with both observational and theoretical works.

3.2 Galaxy formation model

The EAGLE project, is a suite of cosmological hydrodynamical N-body simulations. These simulations were run with a modified version of the GADGET-3 code, which is an improved version of GADGET-2 (Springel, 2005). All the simulations adopt a flat Λ CDM cosmology whose parameters were calibrated with the data obtained by the Planck mission (Planck Collaboration et al., 2014); $\Omega_\Lambda = 0.693$, $\Omega_m = 0.307$, $\Omega_b = 0.04825$, $\sigma_8 = 0.8288$, $Y = 0.248$ and $H_0 = 67.77 \text{ km s}^{-1}$.

In particular, for this work we select our sample of galaxies from the main simulation, referred to as L100N1504, which consists of a periodic box with a volume of $(100\text{cMpc})^3$, initially containing $1,504^3$ gas particles with an initial mass of $1.81 \times 10^6 M_\odot$, and the same amount of dark matter particles with a mass of $9.70 \times 10^6 M_\odot$.

Each simulation counts with 29 discrete snapshots from redshift 20 to 0, with a time span between

consecutive snapshots ranging from 0.3 to 1 Gyr. Radiative cooling and photoheating are implemented following Wiersma et al. (2009a), assuming an optically thin X-Ray/UV background (Haardt & Madau, 2001). Star formation is implemented stochastically following Schaye & Dalla Vecchia (2008), and using the metallicity-dependent density threshold shown in Schaye (2004). This reproduces the observed Kennicutt-Schmith law (Kennicutt, 1998). Each particle is assumed to be a single-age stellar population, with a Chabrier initial mass function in the range $0.1 M_{\odot} - 100M_{\odot}$ (Chabrier, 2003).

Stellar evolution is modelled as shown in Wiersma et al. (2009b), and chemical enrichment is followed for the 11 elements that most contribute to radiative cooling from massive stars (Type II supernovae and stellar winds) and intermediate-mass stars (Type Ia supernovae and AGB stars). Following Dalla Vecchia & Schaye (2012), the thermal-energy product of stellar feedback is stochastically distributed among the gas particles surrounding the event without a preferential direction.

The EAGLE project calibrated the free parameters associated with stellar feedback to match the observations for the stellar mass function in a range of $10^8 M_{\odot} - 10^{11} M_{\odot}$ and the size-mass relation for galaxies in a range of $10^9 M_{\odot} - 10^{11} M_{\odot}$ (Schaye et al., 2015; Furlong et al., 2015, 2017). The appropriate calibration of the subgrid physics and the good agreement with the observational data make these simulations our best tool to study the evolution in the star formation of galaxies in these mass ranges for different environments.

The halo catalogues provided in the public database (used in this work) were built using a friend-of-friends (FoF) algorithm which identifies dark matter overdensities following Davis et al. (1985), considering a linking length of 0.2 times the average inter-particle spacing. Baryonic particles are assigned to the FoF halo of their closest dark matter particle. Subhalo catalogues were built using the SUBFIND algorithm (Springel et al., 2001; Dolag et al., 2009), which identifies local overdensities using a binding energy criterion for particles within a FoF halo. We will define as galaxies those structures recognized by the SUBFIND algorithm (Springel et al., 2001; Dolag et al., 2009) which possess a total stellar mass greater than $10^8 M_{\odot}$ and a total mass greater than $10^9 M_{\odot}$. These masses are obtained by direct summation of the corresponding particles; i.e., particles bound to the subhalo according to the SUBFIND. Since the simulations considered in this work have a baryonic mass resolution of $1.6 \times 10^6 M_{\odot}$ and dark matter mass resolution of $9.1 \times 10^6 M_{\odot}$, we ensure that we have at least 100 baryonic and dark matter particles in each galaxy, thus avoiding spurious results and non-physical detections. The analyzed clusters correspond to the 10 most massive in the simulation at $z = 0$. They all possess $M_{200} > 10^{14} [M_{\odot}]$. A galaxy is defined as satellite if it can be found inside the host R_{200} at $z = 0$.

3.3 The end of the star forming phase: Definitions

According to Peng et al. (2010), the quenching of a galaxy is the result of a process with two different components. A continuous component associated with internal galactic processes such as star formation and AGN feedback, and a “once-only” component due to environmental processes. Note, however, that other mechanisms like mergers may also have an important effect on the star formation activity.

To determine the moment when the star formation activity in a galaxy drops in a significant way, two different criteria are introduced: one based on the maximum drop of the SFR between two consecutive snapshots of the simulation, and the other based on a minimum threshold for specific star formation rate (sSFR). The first criterion seeks to identify those mechanisms that abruptly reduce star formation in galaxies, while the second one is meant to define when a galaxy is actually quenched, that is, it is no longer forming stars (e.g. Weinmann et al. 2010; De Lucia et al. 2012; Wetzel et al. 2012). The

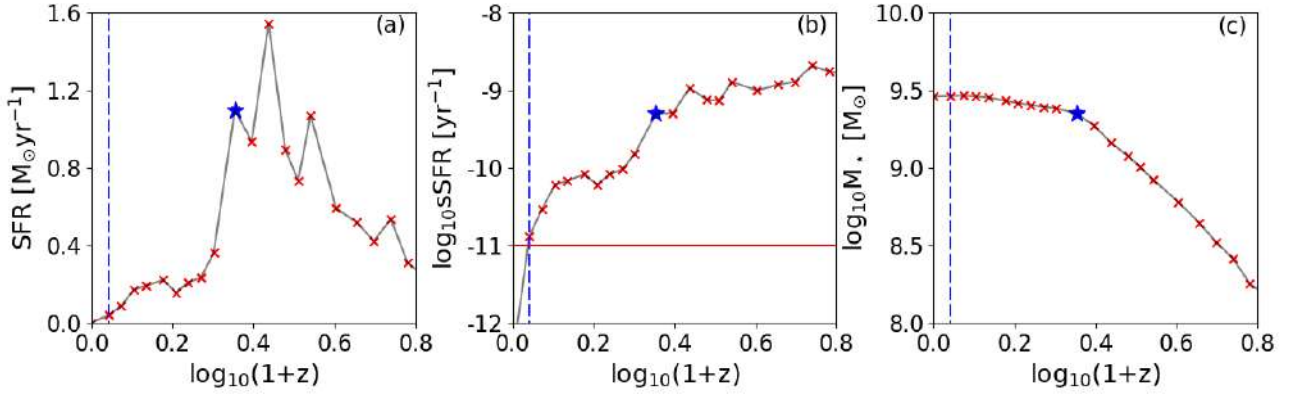


Figure 3.1: Examples of the selection criteria used in this work to determine whether a galaxy was processed or quenched, for a random galaxy in our sample. Panel (a) shows the star formation rate against redshift. The red ellipse highlights the strongest drop in the star formation activity, and the blue dashed line corresponds to the time of the first infall into the final cluster’s R_{200} . Panel (b) shows the specific star formation rate of the galaxy against redshift. The red solid line shows the critical star formation rate imposed by our selection criterion to define quenched galaxies. The blue dashed line corresponds to the first infall into R_{200} . Panel (c) shows the growth of the galaxy stellar mass through cosmic time. The blue star indicates the moment when the processing started. We can see that the growth of the stellar mass is suppressed after the strongest drop, and that the specific star formation rate decreases abruptly after passing R_{200} .

aim of using these two criteria is to determine and understand the different stages of quenching and how they are affected by the environment. From now on, we will refer to a galaxy as “processed” when it suffers its strongest drop, whereas we will refer to a galaxy as “quenched” when it reaches the imposed threshold in sSFR.

3.3.1 SFR Strongest Drop

One of our goals is to identify the mechanisms that can abruptly reduce the star formation in galaxies. For this purpose, we first calculate for each galaxy the variation of the star formation rate between two consecutive snapshots in the simulation, normalized by the star formation in the earliest snapshot. This is

$$\Gamma_{\text{SFR}} = \frac{\text{SFR}_{i+1} - \text{SFR}_i}{\text{SFR}_i}, \quad (3.1)$$

where the subscript i indicates the simulation snapshot, and $i + 1$ is at a lower redshift than i . Γ_{SFR} is computed only if the difference between the SFR value in the two snapshots is larger than $1 \times 10^{-3} M_{\odot} \text{yr}^{-1}$. This constraint was imposed to avoid measures of Γ_{SFR} for galaxies already quenched. We then define $\Gamma_{\text{SFR}}^{\text{SD}}$ as the fraction of star formation lost at the moment when the strongest drop occurs, i.e.

$$\Gamma_{\text{SFR}}^{\text{SD}} = |\min \Gamma_{\text{SFR}}| \quad (3.2)$$

We refer to this method as the “Strongest drop selection criterion”. $\Gamma_{\text{SFR}}^{\text{SD}}$ takes into account those episodes when a “once-only” event affects the star formation activity of the galaxies but does not take into account any rejuvenation scenario that could take place afterwards. For this reason, it is not a good tracer of definitive quenching. However, the information gathered by this criterion allows us

to find the epochs at which the galaxy suffers a “processing” event, in particular the most significant one. An example of this selection criterion is shown in Figure 3.1, panel (a), where we plot, as a function of time, the star formation rate of a random galaxy in our sample. The red ellipse highlights the moment when $\Gamma_{\text{SFR}}^{\text{SD}}$ takes place. In particular for this galaxy, the $\Gamma_{\text{SFR}}^{\text{SD}}$ is the result of several processes that heat and remove its cold gas content, producing a stagnation in the evolution of the stellar mass and a small decrease in the total gas mass of the galaxy. Unfortunately, we cannot isolate the different mechanisms that produce this processing event due to the lack of temporal resolution. We will further explore this in a future work using a better suited simulation.

3.3.2 Critical sSFR criterion

We further wish to define a criterion that aims at identifying the moment when the galaxies reach a definitive state of “quenching”. Several different definitions of “quenched galaxy” have been proposed in the literature. Here we used the criterion used in Wetzel et al. (2013). According to this criterion, a galaxy can be considered effectively quenched once it reaches a $\text{sSFR}^{\text{Q}} = 10^{-11} \text{ yr}^{-1}$. At this point the galaxy is considered to be passive. From now on we will refer to those galaxies with a sSFR lower than sSFR^{Q} as “quenched galaxies”, and we will call this selection criterion the “Critical sSFR Selection Criterion”. When using this semi-observational definition, we will only focus on galaxies that are quenched at redshift $z = 0$. This is to ensure that the selected galaxies will not suffer a rejuvenation process during their evolution. From each of our quenched galaxies, we will extract information about the environment and the time when the quenching state is reached.

An example of this selection criterion is shown in Figure 3.1, panel (b), where the sSFR is shown for the same galaxy from the previous example as a function of time. The red line indicates the sSFR threshold established in previous works (Weinmann et al., 2010; De Lucia et al., 2012; Wetzel et al., 2012, 2013) for passive galaxies. In particular for the galaxy shown in the example, the critical star formation is reached once it crosses the R_{200} of the cluster for the first time, showing the importance of dense environments in the quenching of star formation.

3.4 Results

We wish to study the dependencies of star formation quenching on environmental and internal processes focusing on dense environments such as those that can be found in galaxy clusters. For this it is necessary to characterize the properties of individual galaxies such as stellar mass, sSFR and total mass, as well as the overall properties of the host cluster such as total mass and virial radius. We will study how these properties evolve as a function of time, and focus on those moments where individual galaxies experience sharp falls in their star formation rates.

As previously discussed in Section 3.1, in this work we focus on the population of galaxies associated with the 10 most massive clusters of the EAGLE simulations. In order to study properties of these galaxies as a function of clusters mass with better statistics, the clusters were stacked in three different bins of $z = 0$ total mass:

- high mass: $14.6 < \log_{10} M_{\text{host}} [M_{\odot}] < 14.8$,
- intermediate mass: $14.3 < \log_{10} M_{\text{host}} [M_{\odot}] < 14.6$,
- low mass: $14.0 < \log_{10} M_{\text{host}} [M_{\odot}] < 14.3$.

We will refer to these three categories as HMC, IMC and LMC, respectively. The numbers of cluster that fall in each bin are 2 for the HMC, 5 for the IMC and 3 for the LMC. In this section we present our

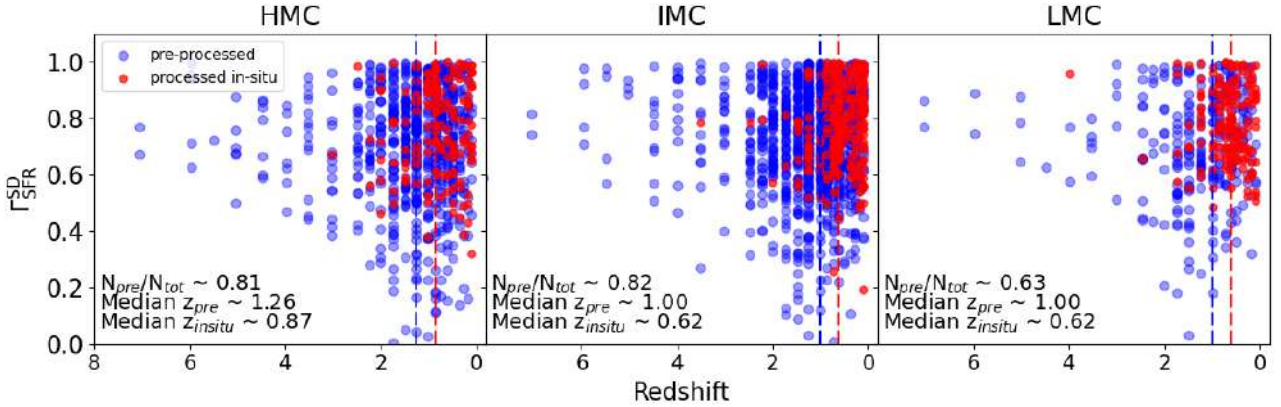


Figure 3.2: Distribution of Γ_{SFR}^{SD} (normalized instantaneous strongest drop of the SF activity), as a function of the redshift at which it takes place. Blue dots correspond to galaxies that suffer their Γ_{SFR}^{SD} outside the cluster’s R_{200} (pre-processed), while red dots to those that suffer their Γ_{SFR}^{SD} inside R_{200} (processed in-situ). The medians for both samples are indicated by the dashed lines. The panels are organized from left to right as high-mass clusters ($14.6 < \log_{10} M_{host} [M_{\odot}] < 14.8$), intermediate-mass clusters ($14.3 < \log_{10} M_{host} [M_{\odot}] < 14.6$) and low-mass clusters ($14.0 < \log_{10} M_{host} [M_{\odot}] < 14.3$), respectively.

results based on the two previously defined criteria to identify the time at which the star formation activity of a galaxy is significantly altered. We will use the terms *in-situ* and *pre* for galaxies that suffer the previously described processes inside or outside the cluster R_{200} , respectively.

3.4.1 Strongest Drop Selection Criterion

We first focus on abrupt changes in the SF activity. We start by computing Γ_{SFR}^{SD} for all galaxies that belong to the 10 most massive clusters at $z = 0$. Our goal is to assess where and when they suffer their most significant processing event. The total number of galaxies in the HMC, IMC and LMC bins are $N_{gal} = 846$, $N_{gal} = 1430$ and $N_{gal} = 421$, respectively. Note that the differences in the number of galaxies is mainly due to the number of clusters that fall in each mass bin.

In Figure 3.2 we show Γ_{SFR}^{SD} for all galaxies as a function of the redshift at which this event takes place. The blue and red dots correspond to pre- and in-situ processed galaxies, respectively. The different panels show the results for the different mass bins. We can clearly see that, for the pre-processed population, there is no preferential redshift for Γ_{SFR}^{SD} to take place. Note as well that there is no clear correlation between redshift and the typical value of Γ_{SFR}^{SD} for both populations. This indicates that these “once-only” events that significantly affect star formation activity are not associated with any preferential epoch.

In all mass bins, the majority of the galaxies have been pre-processed. Interestingly, for in-situ processed galaxies, Γ_{SFR}^{SD} typically occurs at lower values of redshift than for pre-processed galaxies. This can be seen from the dashed vertical lines, which indicate the median redshift for each population. Note as well that the pre-processed fraction grows with clusters mass, but the median in redshift for pre-processing remains the same regardless of the mass bin. This shows that, although more massive clusters accrete a greater number of pre-processed galaxies, the redshift at which Γ_{SFR}^{SD} typically takes place is independent of the $z = 0$ mass of the clusters in which galaxies reside.

To understand how the processing affects the evolution of galaxies and which is the role played by the environment, we characterize the mass distribution of the hosts in which these galaxies resided when

they suffered their $\Gamma_{\text{SFR}}^{\text{SD}}$. In Figure 3.3, panels a), we show the fraction of galaxies per bin of host halo mass, M_{host} , at the time of $\Gamma_{\text{SFR}}^{\text{SD}}$. Fractions are expressed with respect to the total galaxy sample. We split our sample in three populations: pre-processed central galaxies, pre-processed satellites, and in-situ processed satellites. Note that for the pre-processed central population, the mass of the host where the galaxies reside at the moment of processing is nearly the mass of the galaxy itself. From this panel we can clearly see that the three populations are well separated in the host mass distribution, regardless of the mass of the cluster. The median M_{host} of each population is indicated with dashed lines. As we can see, according to the criterion $\Gamma_{\text{SFR}}^{\text{SD}}$, central pre-processed galaxies tend to suffer their $\Gamma_{\text{SFR}}^{\text{SD}}$ in low-mass halos, preferentially in halos with total mass between $10^{10.5} \lesssim M_{\text{host}}[M_{\odot}] \lesssim 10^{11.0}$. For galaxies pre-processed as satellites, $\Gamma_{\text{SFR}}^{\text{SD}}$ occurs in a large variety of halo masses, ranging between $10^{11} \lesssim M_{\text{host}}[M_{\odot}] \lesssim 10^{13.5}$, with a median near $10^{13.0} M_{\text{host}}[M_{\odot}]$ regardless of the mass of the cluster (the typical mass of galaxy groups). On the other hand, for the in-situ processed, it preferentially occurs in higher mass halos, with total masses larger than $10^{14.0} M_{\text{host}}[M_{\odot}]$.

To explore the relation between $\Gamma_{\text{SFR}}^{\text{SD}}$ and environment we compute, for the overall processed galaxy population, the distribution of total mass (M_{galaxy}) and the stellar mass fraction ($M_{\star}/M_{\text{galaxy}}$) at the time they suffer their $\Gamma_{\text{SFR}}^{\text{SD}}$. These are shown on panels b) and c) of Figure 3.3, respectively. In general we find that in-situ processed galaxies tend to have a marginally larger M_{galaxy} than pre-processed galaxies. Interestingly, the difference in $(M_{\star}/M_{\text{galaxy}})$ for these three populations is significantly more evident, with the central pre-processed galaxies showing the lowest stellar mass fractions. This is in agreement with the results shown in Figure 3.2, where we show that $\Gamma_{\text{SFR}}^{\text{SD}}$ for the in-situ population occurs at lower redshift, thus giving more time to these galaxies to grow in stellar mass. Note as well that there is a preference for pre-processing to occur in galaxies when they still remain as centrals, specially for the LMC bin, as shown by the green bars. We found that, for the pre-processed population, 54.07% in the HMC bin, 52.14% in the IMC, and 69.81% in the LMC were pre-processed as centrals.

As expected for central galaxies, the M_{host} and M_{galaxy} distributions are similar. In Figure 3.3, panel d), we show the distribution of stellar mass, M_{\star} , for all galaxies at the time of the first R_{200} crossing. We can clearly see that the difference in M_{\star} between in-situ and pre-processed galaxies is not only present at the time of $\Gamma_{\text{SFR}}^{\text{SD}}$, but pre-processed galaxies tend to arrive in the cluster with a significantly lower stellar mass. These results suggest that one of the strongest effects associated with this pre-processing is to limit the final stellar mass of satellites in galaxy clusters. As an example, in Figure 3.1, Panel c, we show how the $\Gamma_{\text{SFR}}^{\text{SD}}$ significantly affects the subsequent growth of M_{\star} in a galaxy. For the pre-processed population, we have derived the time difference between the infall time, t_{inf} , and the pre-processing time, t_{proc} . In general, we find that $(t_{\text{proc}} - t_{\text{inf}})$ is smaller for satellite galaxies than for centrals, and that this quantity grows with cluster mass. This result explains the difference in stellar mass ratio at the moment of the processing seen in Figure 3.3 for the pre-processed population. Central galaxies suffer their pre-processing earlier than the satellite sample and, despite the fact that both populations shows similar M_{\star} at the moment of the infall, those which had their strongest drop as centrals are more dark matter dominated.

It is clear from Figure 3.3 that centrals represent an important fraction of the pre-processed population, as they constitute $\gtrsim 50\%$ of this population in any mass bin. In isolated and low-mass galaxies several mechanisms can significantly affect the star formation history and current star formation activity. Examples are photo-reionization, which limits their gas reservoir to form stars (Hopkins et al., 2014; Chan et al., 2018), or supernova feedback which, thanks to the injection of large amounts of kinetic energy into the intergalactic medium, can eject significant fractions of the available gas (Dekel & Silk, 1986; Davé et al., 2011; Biernacki & Teyssier, 2018). In addition, as shown by Benítez-Llambay et al. (2013), ram-pressure stripping from the gas distribution within the cosmic web can efficiently remove

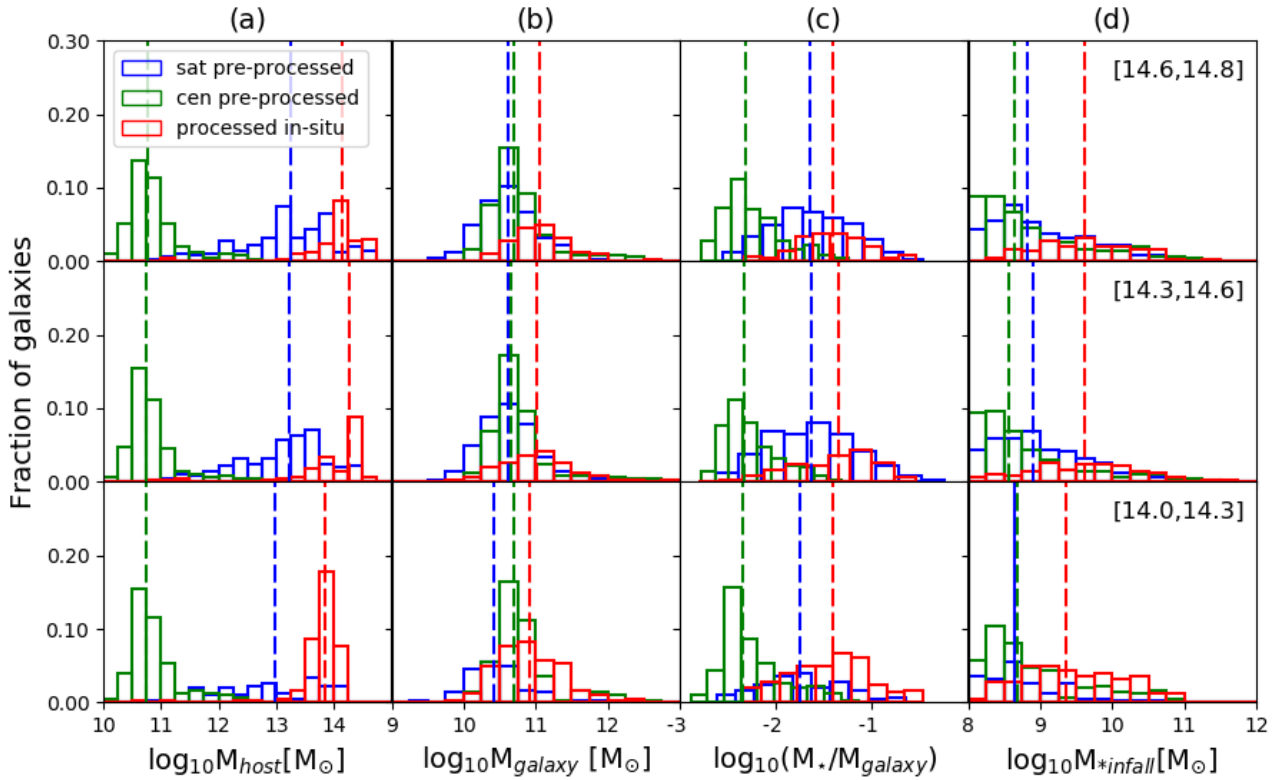


Figure 3.3: Mass distribution of galaxies and their hosts at key moments related to the $\Gamma_{\text{SFR}}^{\text{SD}}$. Each row shows the results obtained after stacking the distribution of galaxies associated with clusters within different mass ranges. Column (a) shows the mass distribution of the host of each galaxy at the moment of their $\Gamma_{\text{SFR}}^{\text{SD}}$. Column (b) shows the total mass distribution of the galaxies at their $\Gamma_{\text{SFR}}^{\text{SD}}$. Column (c) shows the stellar mass fraction distributions at $\Gamma_{\text{SFR}}^{\text{SD}}$. Column (d) shows the stellar mass distribution of galaxies at the time of their first infall into the cluster they belong to at $z = 0$. Blue, red and green bars correspond to galaxies pre-processed, in-situ processed, and processed as centrals, respectively. The dashed lines indicate the median of each distribution.

the gas content of isolated low-mass galaxies. Pre-processing in galaxies that were not centrals at the time of $\Gamma_{\text{SFR}}^{\text{SD}}$ is generally associated with ram-pressure stripping within the corresponding host. However, Figure 3.3 shows that the environment associated with a massive host galaxy plays a minor role in the pre-processing of low-mass galaxies.

As discussed before, the fraction of galaxies processed in-situ is rather low ($\lesssim 30\%$), and these galaxies tend to be more massive than the pre-processed population at the time of their corresponding $\Gamma_{\text{SFR}}^{\text{SD}}$. Their most significant drop in star formation activity took place within the R_{200} of the main cluster. Thus, the main mechanisms acting are tidal and ram-pressure stripping within the cluster itself. This highlights the role played by the denser environment associated with galaxy clusters.

There is a small fraction ($<30\%$) of pre-processed galaxies for which $\Gamma_{\text{SFR}}^{\text{SD}}$ takes place in high-mass halos different from the main cluster. These halos correspond to objects that belong to massive galaxy-groups, in the mass range $10^{13.0} \lesssim M_{\text{host}}[M_{\odot}] \lesssim 10^{14.0}$, that are later accreted into the main cluster.

3.4.2 Critical sSFR Selection Criterion

In Section 3.4.1 we focused on the the properties of galaxies when they suffer their strongest drop in their star formation, $\Gamma_{\text{SFR}}^{\text{SD}}$. These drops do not necessarily result in the cessation of the star formation activity. Rather, as shown in Section 3.4.1, on average pre-processed galaxies arrive in the cluster with a significantly lower stellar mass than those galaxies processed in-situ. Thus, instead of ceasing the star formation activity, an early $\Gamma_{\text{SFR}}^{\text{SD}}$ constrains the final galactic stellar mass.

In this Section we will focus on the moment when galaxies become effectively quenched. Within the R_{200} each cluster, we search for galaxies with sSFR values lower than sSFR^{Q} defined in Section 3.3.2, and track their specific star formation history to identify the moment when this threshold is crossed. As before, we separate our galaxy sample in three bins according to cluster mass. The number of quenched galaxies in each bin is $N_{\text{gal}} = 780, 1282$ and 374 for the HMC, IMC and LMC bins, respectively. Note that, in general, the number of quenched galaxies in each bin is $\lesssim 12\%$ smaller than the number of galaxies that have suffered some type of processing.

In the left panels of Figure 3.4 we show the host mass distribution associated with each galaxy at the time in which they became quenched. As before, for galaxies that became quenched while being centrals (green bars), $M_{\text{host}} \sim M_{\text{galaxy}}$. Contrary to what is found with the $\Gamma_{\text{SFR}}^{\text{SD}}$ criterion, we find that, independently of the cluster mass bin, the vast majority of galaxies become quenched within massive hosts with $10^{13.5} \lesssim M_{\text{host}}[M_{\odot}] \lesssim 10^{14.5}$. This highlights the important role played by the denser environment of massive clusters on the overall quenching of their galaxy members. As an example we show, in Figure 3.5, the time evolution of the sSFR of six galaxies in our sample as they approach the central galaxy of one of our clusters. The dashed lines show the time evolution of the clusters R_{200} and the color bar the sSFR of each galaxy. The star denotes the moment when the $\Gamma_{\text{SFR}}^{\text{SD}}$ takes place. Note that galaxies in panel a) reach their quenching state as centrals. Also, it is interesting to note that the quenching state is reached as a consequence of their $\Gamma_{\text{SFR}}^{\text{SD}}$. For galaxies in panels b) and f), they reach their quenching state as satellites before they were accreted by the cluster, and galaxies in panels c) d) and e) are quenched inside the cluster R_{200} . Also, in any case, as galaxies approach the cluster center, their sSFR slowly decreases. However, the change in sSFR just after the first R_{200} crossing is significantly more abrupt, in some cases rapidly resulting in quenching. On the other hand, galaxies that quenched in low-mass halos, i.e. $10^{10.0} \lesssim M_{\text{host}}[M_{\odot}] \lesssim 10^{11.0}$, did it as centrals, highlighting the regime where internal quenching processes are most relevant.

The red bars on Figure 3.4 indicate the distributions of the in-situ quenched galaxies population. Interestingly, we find that the fraction of galaxies that arrived in the cluster already quenched (i.e., pre-quenched population) increases with cluster mass. For comparison we find 73% of the galaxies

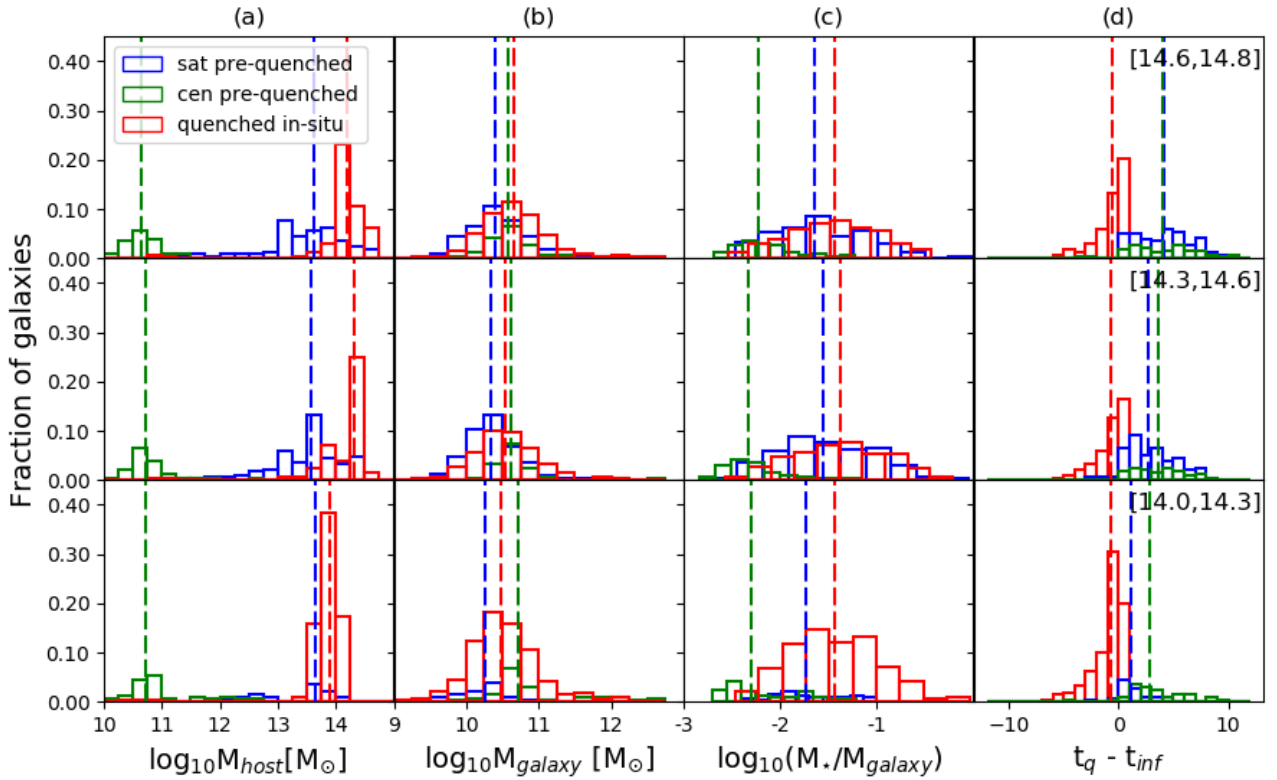


Figure 3.4: Mass distribution of galaxies and their hosts at the moment when they reach their quenching state. Each row shows the results obtained after stacking the distribution of galaxies associated with clusters within different mass ranges. Column (a) shows the mass distribution of the host of each galaxy. Column (b) shows distribution of galaxies’ total mass. Column (c) shows the stellar mass fraction distributions. Column (d) shows the distribution of times, in lookbacktime, at which galaxies become quenched. Blue, red and green bars correspond to galaxies pre-quenched, in-situ quenched, and quenched as centrals, respectively. The dashed lines indicate the median of each distribution.

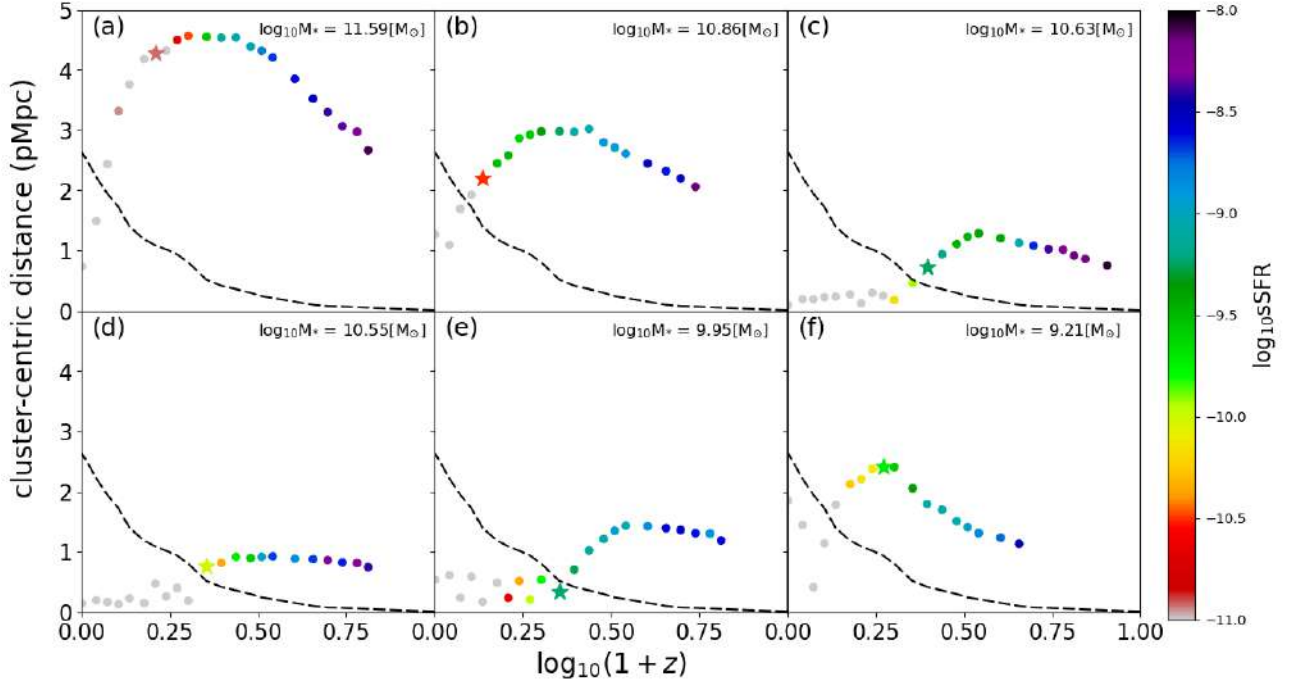


Figure 3.5: Time evolution of cluster-centric distance for a subset of four galaxies in our sample. In panel a) we show a galaxy pre-quenched as central, in panels b) and f) we have galaxies pre-quenched as satellite, and for panels c), d) and e), we have galaxies quenched in-situ. The color coding indicates the sSFR at each time. The dashed line shows the time evolution of the cluster R_{200} and the star shows the moment when the galaxies suffer their “processing” event. The label indicates the galaxy stellar mass at $z = 0$.

were quenched in-situ in the LMC bin, but only 45% in the HMC bin. This apparent relation between the fraction of pre-quenched galaxies with cluster mass is further explored below. As in the case of the $\Gamma_{\text{SFR}}^{\text{SD}}$ criterion, we find the total mass distribution of pre- and in-situ quenched galaxies to be very similar (medium-left panels), but they show a significant offset on their stellar masses at the moment of quenching (medium-right panels). As expected, we find that most pre-quenched galaxies ($\sim 95\%$) have also been pre-processed, indicating the important role played by the pre-processing in the quenching of low-mass objects. Panel d) of Figure 3.4 shows the distribution of $(t_q - t_{\text{inf}})$, where t_q represents the galaxy quenching time. We find a relation between t_q and cluster mass for the pre-quenched population, where the high mass bin presents bigger differences between both times. This is a result of the hierarchical scenario; i.e., bigger clusters accrete bigger structures and, thus, environmental effects are more significant since earlier epochs. In general for the in-situ quenched population, we find no difference in $(t_q - t_{\text{inf}})$, between the different mass bins, highlighting the role of the virial-radius crossing in the star formation quenching of galaxies.

In figure 3.6 we show the time evolution of the cumulative fraction of quenched galaxies, N_q/N_{total} , as a function of cluster-centric distance. Here, N_q represents the number of quenched galaxies within a given radius, R , and N_{total} the total number of galaxies within the same distance. The different lines correspond to the different cluster mass bins. Interestingly, we see that at early times, between $z \sim 1$ and $z \sim 0.5$, the fraction of quenched galaxies grows towards the cluster outskirts. However, at later times this trend reverses, showing a decreasing fraction of quenched galaxies with distance. During the last decade, surveys such as WINGS (Cava et al., 2017) and SAMI (Brough et al., 2017) have shown that:

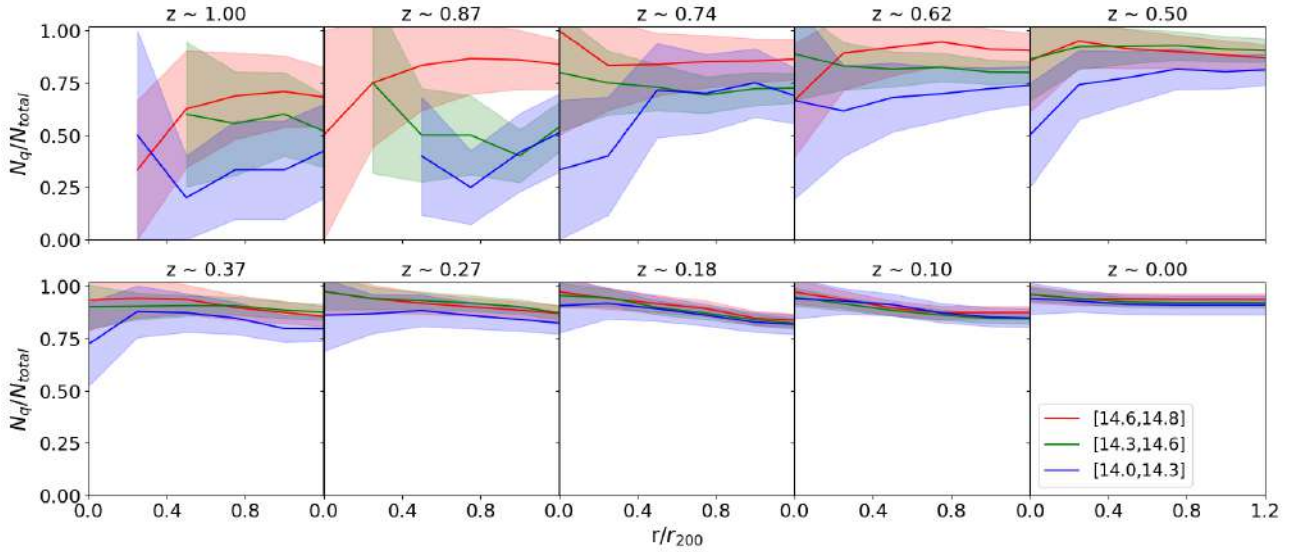


Figure 3.6: Time evolution of the cumulative fraction of quenched galaxies within the clusters' R_{200} . The red, green and blue lines show the results for the high, intermediate and low mass clusters, respectively. The shaded regions show Poissonian errors.

1. the fraction of quenched galaxies grows towards $z = 0$. This is attributed to the environment having more time to act on cluster galaxies, in addition to the cluster build-up by accretion of structures;
2. the fraction of quenched galaxies decreases with cluster-centric distance. Thanks to the denser environments that can be found in the inner cluster region, galaxies, especially those with lower masses, can be more efficiently depleted of their gas reservoir.

Our results are in good agreement with these observations.

We have previously highlighted a correlation between the fraction of pre-quenched galaxies and cluster mass. We further explore this correlation in Figure 3.7. Here we show how the cumulative fraction of quenched galaxies, with respect to the total number of all galaxies that can be found within R_{200} at $z = 0$, grows as a function of the normalized time, $t - t_{\text{infall}}$. To generate this plot, we first compute for each galaxy within R_{200} at $z = 0$ the time when it first crossed R_{200} . Second, for each galaxy we define the variable $t - t_{\text{infall}}$ and identify the moment when it became quenched on this new time scale. Finally, we compute the cumulative quenched galaxy fraction as a function of $t - t_{\text{infall}}$. This figure allows us to study how the fraction of quenched galaxies changes as a function of the time they remain either outside (negative $t - t_{\text{infall}}$) or inside (positive $t - t_{\text{infall}}$) the cluster's R_{200} . The different lines are associated with the galaxy populations of different clusters. The colors indicate the mass of each cluster at $z = 0$. Note that, in all clusters, the fraction of quenched galaxies slowly grows as galaxies approach the cluster's R_{200} , again highlighting the role of pre-processing. Interestingly, there is a change in the slope of this cumulative function around the time of the first R_{200} crossing, i.e. $-1 \text{ Gyr} \lesssim t - t_{\text{infall}} \lesssim 1 \text{ Gyr}$. During this period, the fraction of quenched galaxies raises more rapidly than during any other epoch. This is in agreement with the behaviour of the sSFR observed in Figure 3.5, and clearly displays the role played by the cluster's environment. We can also observe a large dispersion in the fraction of galaxies that arrive quenched at the cluster's R_{200} , with values that go from 20 to 60%. More importantly, this fraction shows a dependency with final cluster mass, with larger values for more massive clusters.

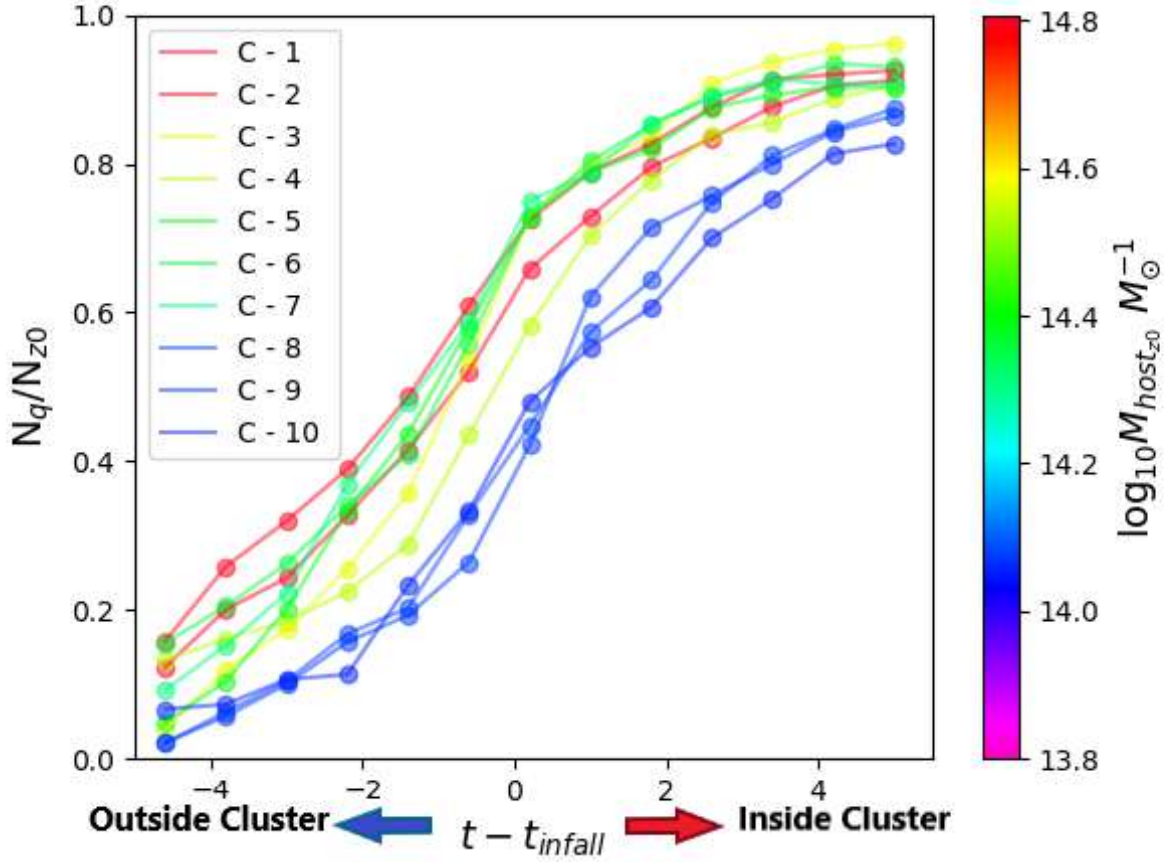


Figure 3.7: Cumulative fraction of quenched galaxies as a function of the normalized time scale, $t - t_{\text{infall}}$. The infall time t_{infall} is computed for each individual galaxy. The color coding indicates the total mass of each cluster at $z = 0$. Negative (positive) $t - t_{\text{infall}}$ corresponds to periods of time when galaxies are located outside (inside) the cluster’s R_{200} .

To study the origin of this trend we compute the mass distribution of the structures, M_{host} , where the quenched galaxy population at $z = 0$ were located at the snapshot before their first R_{200} crossing. This is shown in Figure 3.8, panels a). As before, each row corresponds to the results obtained from a different cluster mass bin. The blue bars indicate the fraction of pre-quenched galaxies, while the white bars show all the quenched galaxies found within the cluster at $z = 0$. The dashed lines indicate the median for the pre-quenched population. Interestingly, pre-quenched galaxies on the LMC bin tend to arrive in lower mass structures than in the rest of the cluster mass bins. However, no significant difference is observed in both the distribution of total (M_{galaxy}) and stellar masses (M_{\star}) of the pre-quenched galaxy populations at infall, shown in panels b) and c), respectively.

Our results indicate that the larger fraction of pre-quenched galaxies in larger mass clusters is the result of the hierarchical nature of the Λ CDM cosmological model used in this work, in which larger mass object can accrete more massive substructures. These more massive substructures are naturally more efficient in quenching their own galaxy satellite population, thus resulting in a larger fraction of pre-quenched galaxies at $z = 0$.

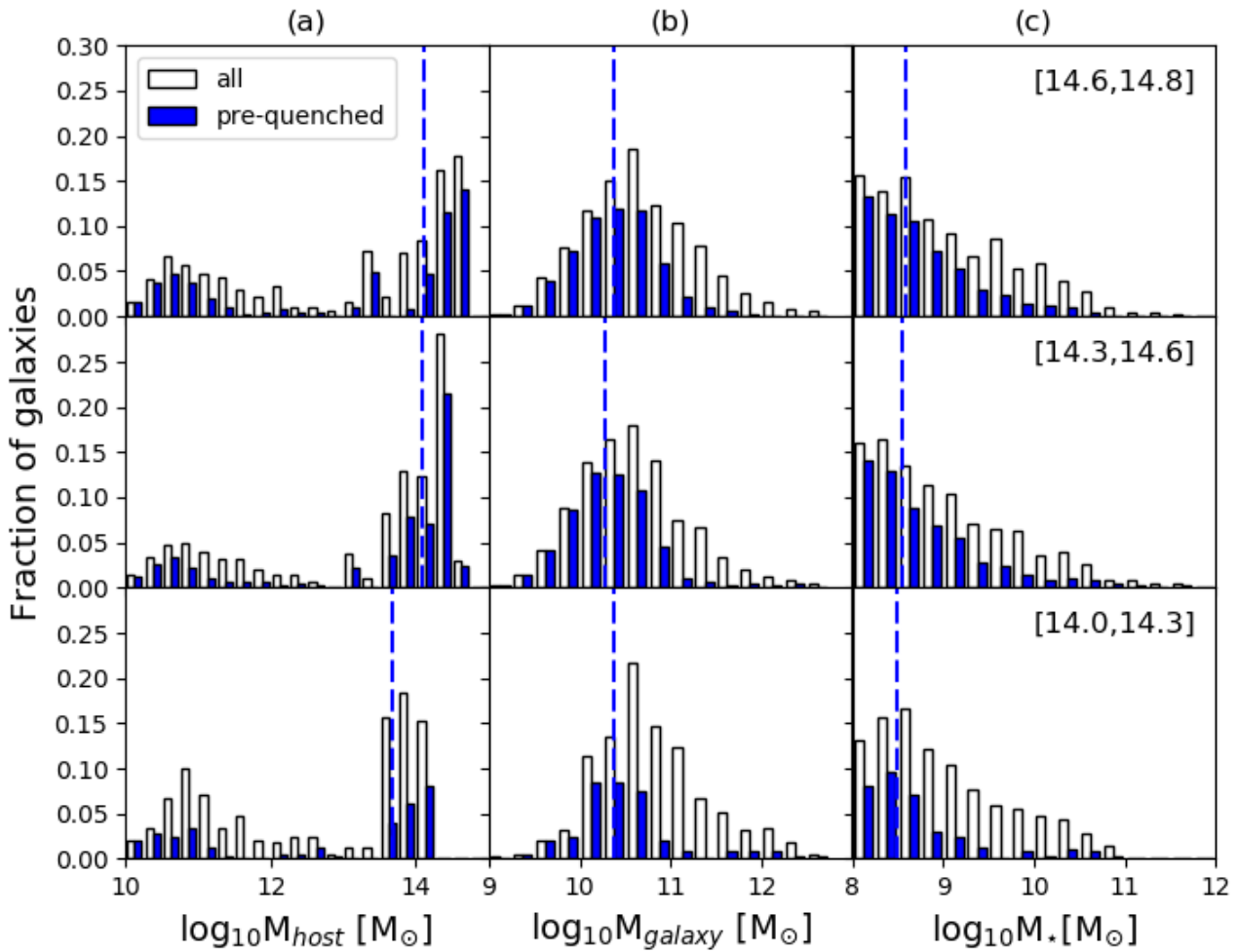


Figure 3.8: Mass distribution of galaxies and their hosts at the moment before crossing the cluster’s R_{200} . Each row shows the results obtained after stacking the distribution of galaxies associated with clusters within different mass ranges. Column (a) shows the mass distribution of the host of each galaxy. Column (b) shows the distribution of galaxy total mass. Column (c) shows the distributions of stellar mass. The blue bars correspond to the galaxies quenched before the first infall and the white bars correspond to all galaxies in our sample. Dashed lines correspond to the median of the pre-quenched population.

3.5 Discussion and Conclusions

In this Chapter we have presented a study of the different environmental-quenching and processing scenarios undergone by the satellite galaxies of the ten most massive clusters in the state-of-the-art EAGLE hydrodynamical simulation. Two different criteria were defined to explore the different processes that significantly affect the SFR of these galaxies along their history. Our goal is to quantify and characterize the role played by the environment in these processes.

For the instantaneous strongest drop in SFR, we find that the majority of galaxies suffer their $\Gamma_{\text{SFR}}^{\text{SD}}$ outside the cluster's R_{200} (pre-processed fraction $\gtrsim 60\%$). This fraction grows with cluster mass. We find that there is no correlation between the strength of the $\Gamma_{\text{SFR}}^{\text{SD}}$ and the time at which it occurs, nor a preferential redshift for it to happen. Nonetheless, for galaxies processed in-situ, $\Gamma_{\text{SFR}}^{\text{SD}}$ tends to happen at lower redshift than for the pre-processed population. In terms of the environment, while in-situ processing mainly occurs in massive hosts, pre-processing shows a strong preference to take place in galaxies that are either low mass and central ($10^{10.5} \lesssim M_{\text{host}} [M_{\odot}] \lesssim 10^{11.0}$) or that belong to low-to-middle mass hosts ($10^{11} \lesssim M_{\text{host}} [M_{\odot}] \lesssim 10^{13.5}$). Our results are in good agreement with those published by Bianconi et al. (2018), who observationally studied a sample of 23 massive clusters ($M_{200} = 10^{15.0} [M_{\odot}]$) with 34 infalling groups ($\log_{10} M_{\star} [M_{\odot}] = 10.75$), located in outer cluster regions. They found that at cluster-centric distances $R \sim 1.3R_{200}$ the fraction of star-forming galaxies in infalling groups is half of that in the clusters. According to this, Bianconi et al. (2018) suggest that the pre-processing in groups is the responsible for these results.

Interestingly, for galaxies with similar total mass, at the time of arrival in the main cluster, the in-situ processed population shows in general a larger stellar mass than those pre-processed. This highlights the important role of pre-processing in limiting the star formation activity of low-mass galaxies. The origin of this pre-processing event can be explained by a variety of different internal mechanisms such as supernova feedback, photo-reionization, interactions and starburst phases. Unfortunately, due to the poor time and spatial resolution available with this simulation, it is too hard to identify what the main mechanism acting on each galaxy is. In addition, ram-pressure from the cosmic web can also cause an accelerated depletion of the gas reservoirs in low mass galaxies, producing abrupt changes in their star formation (Benítez-Llambay et al., 2013).

In the case of the Critical sSFR criterion, contrary to our results for $\Gamma_{\text{SFR}}^{\text{SD}}$, we find that quenching presents a strong preference for high-mass halos to take place. This is a strong indicator that dense environments promote the definitive cessation of the star formation.

Our results are in agreement with the observations presented by Olave-Rojas et al. (2018), who find that the fraction of high-mass ($M_{\star} \geq 10^{10.5} [M_{\odot}]$) red (i.e. passive) galaxies in clusters at $z \sim 0.4$ (i.e. quenched in-situ) is higher than the fraction of high-mass red galaxies in accreted groups (i.e. pre-quenched). We find that most of the pre-quenched galaxies ($\gtrsim 95\%$) have also been pre-processed, evidencing the importance of pre-processing in the quenching of low-mass galaxies. In general we find a slight preference for pre-quenching to take place at earlier times compared with quenching in-situ. The difference in the median of the quenching time distribution is only of the order of 1 to 2 Gyr. As a function of cluster-centric distance, close to $z = 0$ the fraction of quenched galaxies grows toward the cluster center. This is in good agreement with the results obtained from observational studies based on different surveys such as WINGS (Cava et al., 2017) and SAMI (Brough et al., 2017). However, at earlier times, between $z \sim 1$ and $z \sim 0.5$, this trend reverts, showing a fraction of quenched galaxies that grows towards the cluster outskirts.

In general, we find that in comparison to the in-situ quenched population, on average pre-quenched galaxies have lower stellar-masses. This result appears to be in disagreement with those presented by Hou et al. (2014) who found that, independent of galaxy mass, the fraction of quiescent galaxies

is higher in groups than in the clusters and field. However, we can reconcile our findings with those of Hou et al. (2014) by noting that those authors only studied galaxies with stellar masses in the range $9.5 < \log_{10} M_{\star} [M_{\odot}] < 10.5$ and with $10^{12.0} \leq M_{\text{halo}} [M_{\odot}] \leq 10^{14.0}$. In these massive and dense substructures the environmental quenching effects are stronger.

We find a sharp rise in the fraction quenched satellites at the time of the first infall, highlighting the role played by the dense cluster environment. It is interesting to note that, although galaxies prefer denser environments to reach their quenching state, the fraction of pre-quenched galaxies in our sample grows with the total mass of the cluster at $z = 0$. We find that 73% of galaxies were quenched in-situ in the low-mass clusters, but only 45% were quenched in-situ for the high-mass clusters. To explain why high-mass clusters show higher fractions of pre-quenched galaxies, we explore the mass distribution of the structures where the cluster satellite galaxies reside at the moment of accretion. We find that high-mass clusters preferentially accrete their satellites through structures and groups that are significantly more massive than those accreted by low-mass clusters. This is a direct consequence of the hierarchical cosmological model used in these simulations. More massive clusters tend to accrete more massive substructures. Due to their own intracluster dense environments, these massive substructures arrive in the clusters with their satellite population already quenched.

Cora et al. (2018a) explored the quenching time of galaxies, and the relevance of the environment on this process, using the semi-analytic model SAG (Cora et al., 2018b). A criterion similar to our sSFR threshold was imposed. According to their results, environmental effects dominate the star formation quenching of low-mass satellite galaxies ($M_{\star} < 10^{10.1} [M_{\odot}]$). These results are in good agreement with our results. Panels a) and c) of Figure 3.4 show that we also find an important fraction of low-stellar mass galaxies that are quenched within the cluster's R_{200} . Note that a significant fraction of the low-stellar mass galaxies that arrive in the cluster as quenched galaxies were actually quenched in the dense environments of massive groups. This exemplifies the relevance of the environment in the quenching of the cluster satellite population.

We also find that there is a fraction of low-stellar mass galaxies that are quenched as centrals. According to Benítez-Llambay et al. (2013), this can be explained through a combination of different mechanisms that are acting simultaneously on dwarf galaxies. Processes such as supernova feedback and photo-reionization can reheat the cool gas of these galaxies inducing the quenching of their star formation activity, a scenario commonly referred to as mass quenching. In addition, as previously discussed, ram-pressure stripping taking place within the cosmic web filaments can also deplete the gas reservoir of dwarf galaxies, producing a quenching state due to the environment.

As we mentioned before, due to the limited number of snapshots available in the simulation, we do not have the capabilities to separate and distinguish the different overlapping processes that are influencing the star formation history of the galaxies. In the following Chapter we will explore these different mechanisms using the C-EAGLE simulation, a suite of hydrodynamical zoom-in simulations, better suited for this purpose.

These simulations provide us with a great improvement in temporal resolution, with a temporal resolution of 500 Myr for group catalogues (Barnes et al., 2017; Bahé et al., 2017). Since this simulation suite also counts with a sample of 30 clusters with a M_{200} in the range between of $10^{14.0} < M_{200} [M_{\odot}] < 10^{15.4}$, this study has allowed us to explore in more detail the dependency between cluster mass and fraction of pre-quenched galaxies.

Bibliography

- Abadi M. G., Moore B., Bower R. G., 1999, , 308, 947
- Bahé Y. M., et al., 2017, , 470, 4186
- Baldry I. K., Balogh M. L., Bower R. G., Glazebrook K., Nichol R. C., Bamford S. P., Budavari T., 2006, , 373, 469
- Balogh M. L., et al., 2007, , 374, 1169
- Balogh M. L., et al., 2016, , 456, 4364
- Barnes J. E., Hernquist L., 1996, , 471, 115
- Barnes D. J., et al., 2017, , 471, 1088
- Benítez-Llambay A., Navarro J. F., Abadi M. G., Gottlöber S., Yepes G., Hoffman Y., Steinmetz M., 2013, , 763, L41
- Bianconi M., Smith G. P., Haines C. P., McGee S. L., Finoguenov A., Egami E., 2018, , 473, L79
- Biernacki P., Teyssier R., 2018, , 475, 5688
- Boselli A., Gavazzi G., 2006, , 118, 517
- Boselli A., et al., 2005, , 629, L29
- Bravo-Alfaro H., Cayatte V., van Gorkom J. H., Balkowski C., 2000, , 119, 580
- Brough S., et al., 2017, , 844, 59
- Butcher H., Oemler Jr. A., 1984, , 285, 426
- Byrd G., Valtonen M., 1990, , 350, 89
- Cantalupo S., 2010, , 403, L16
- Cassata P., et al., 2008, , 483, L39
- Cava A., et al., 2017, , 606, A108
- Cayatte V., van Gorkom J. H., Balkowski C., Kotanyi C., 1990, , 100, 604
- Chabrier G., 2003, , 115, 763
- Chan T. K., Kereš D., Wetzel A., Hopkins P. F., Faucher-Giguère C.-A., El-Badry K., Garrison-Kimmel S., Boylan-Kolchin M., 2018, , 478, 906
- Chester C., Roberts M. S., 1964, , 69, 635
- Cora S. A., Hough T., Vega-Martínez C. A., Orsi Á., 2018a, preprint, (arXiv:1801.03884)
- Cora S. A., et al., 2018b, , 479, 2

- Crain R. A., et al., 2015, , 450, 1937
- Croton D. J., et al., 2006, , 365, 11
- Cybulski R., Yun M. S., Fazio G. G., Gutermuth R. A., 2014, , 439, 3564
- Dalla Vecchia C., Schaye J., 2012, , 426, 140
- Davé R., Oppenheimer B. D., Finlator K., 2011, , 415, 11
- Davis M., Efstathiou G., Frenk C. S., White S. D. M., 1985, , 292, 371
- De Lucia G., Weinmann S., Poggianti B. M., Aragón-Salamanca A., Zaritsky D., 2012, , 423, 1277
- Dekel A., Birnboim Y., 2008, , 383, 119
- Dekel A., Silk J., 1986, , 303, 39
- Desai V., et al., 2007, , 660, 1151
- Dolag K., Borgani S., Murante G., Springel V., 2009, , 399, 497
- Dressler A., 1980, , 236, 351
- Dressler A., 1984, , 22, 185
- Dressler A., et al., 1997, , 490, 577
- Dressler A., Oemler Jr. A., Poggianti B. M., Gladders M. D., Abramson L., Vulcani B., 2013, , 770, 62
- Efstathiou G., 2000, , 317, 697
- Faber S. M., 1973, , 179, 731
- Fasano G., Poggianti B. M., Couch W. J., Bettoni D., Kjærgaard P., Moles M., 2000, , 542, 673
- Fujita Y., 2004, , 56, 29
- Furlong M., et al., 2015, , 450, 4486
- Furlong M., et al., 2017, , 465, 722
- Gavazzi G., Fumagalli M., Cucciati O., Boselli A., 2010, , 517, A73
- Gray M. E., Wolf C., Meisenheimer K., Taylor A., Dye S., Borch A., Kleinheinrich M., 2004, , 347, L73
- Gunn J. E., Gott III J. R., 1972, , 176, 1
- Haardt F., Madau P., 2001, in Neumann D. M., Tran J. T. V., eds, Clusters of Galaxies and the High Redshift Universe Observed in X-rays. p. 64 (arXiv:astro-ph/0106018)
- Haines C. P., et al., 2013, , 775, 126
- Haines C. P., et al., 2015, , 806, 101

- Hashimoto Y., Oemler Jr. A., Lin H., Tucker D. L., 1998, , 499, 589
- Hogg D. W., et al., 2004, , 601, L29
- Hopkins P. F., Kereš D., Oñorbe J., Faucher-Giguère C.-A., Quataert E., Murray N., Bullock J. S., 2014, , 445, 581
- Hou A., Parker L. C., Harris W. E., 2014, , 442, 406
- Jaffé Y. L., Smith R., Candlish G. N., Poggianti B. M., Sheen Y.-K., Verheijen M. A. W., 2015, , 448, 1715
- Jaffé Y. L., et al., 2016, , 461, 1202
- Just D. W., Zaritsky D., Sand D. J., Desai V., Rudnick G., 2010, , 711, 192
- Katsianis A., et al., 2017, , 472, 919
- Kauffmann G., White S. D. M., Heckman T. M., Ménard B., Brinchmann J., Charlot S., Tremonti C., Brinkmann J., 2004, , 353, 713
- Kennicutt Jr. R. C., 1998, , 498, 541
- Kodama T., Smail I., Nakata F., Okamura S., Bower R. G., 2001, , 562, L9
- Lewis I., et al., 2002, , 334, 673
- McAlpine S., et al., 2016, *Astronomy and Computing*, 15, 72
- McGee S. L., Balogh M. L., Bower R. G., Font A. S., McCarthy I. G., 2009, , 400, 937
- Miller R. H., 1986, , 167, 41
- Moore B., Katz N., Lake G., Dressler A., Oemler A., 1996, , 379, 613
- Moore B., Lake G., Quinn T., Stadel J., 1999, , 304, 465
- Moran S. M., Ellis R. S., Treu T., Smith G. P., Rich R. M., Smail I., 2007, , 671, 1503
- Morgan W. W., Mayall N. U., 1957, , 69, 291
- Muzzin A., et al., 2012, , 746, 188
- Nantais J. B., et al., 2016, , 592, A161
- Nelson D., et al., 2018, , 475, 624
- Oesch P. A., et al., 2016, , 819, 129
- Olave-Rojas D., Cerulo P., Demarco R., Jaffé Y. L., Mercurio A., Rosati P., Balestra I., Nonino M., 2018, , 479, 2328
- Overzier R. A., 2016, , 24, 14

- Pallero D., Gómez F. A., Padilla N. D., Torres-Flores S., Demarco R., Cerulo P., Olave-Rojas D., 2019, , 488, 847
- Peng Y.-j., et al., 2010, , 721, 193
- Peng Y., Maiolino R., Cochrane R., 2015, , 521, 192
- Planck Collaboration et al., 2014, , 566, A54
- Poggianti B. M., Smail I., Dressler A., Couch W. J., Barger A. J., Butcher H., Ellis R. S., Oemler Jr. A., 1999, , 518, 576
- Poggianti B. M., et al., 2001, , 562, 689
- Poggianti B. M., et al., 2006, , 642, 188
- Quilis V., Moore B., Bower R., 2000, *Science*, 288, 1617
- Roberts M. S., Haynes M., 1994, in Meylan G., Prugniel P., eds, *European Southern Observatory Conference and Workshop Proceedings Vol. 49, European Southern Observatory Conference and Workshop Proceedings*. p. 197
- Schaye J., 2004, , 609, 667
- Schaye J., Dalla Vecchia C., 2008, , 383, 1210
- Schaye J., et al., 2015, , 446, 521
- Smail I., Ellis R. S., Dressler A., Couch W. J., Oemler A., Sharples R. M., Butcher H., 1997, , 479, 70
- Springel V., 2005, , 364, 1105
- Springel V., White S. D. M., Tormen G., Kauffmann G., 2001, , 328, 726
- Strateva I., et al., 2001, , 122, 1861
- Tescari E., et al., 2018, , 473, 380
- Toomre A., Toomre J., 1972, in *Bulletin of the American Astronomical Society*. p. 214
- Trayford J. W., et al., 2015, , 452, 2879
- Trayford J. W., Theuns T., Bower R. G., Crain R. A., Lagos C. d. P., Schaller M., Schaye J., 2016, , 460, 3925
- Treu T., Ellis R. S., Kneib J.-P., Dressler A., Smail I., Czoske O., Oemler A., Natarajan P., 2003, , 591, 53
- Vijayaraghavan R., Ricker P. M., 2013, , 435, 2713
- Vollmer B., Cayatte V., Balkowski C., Duschl W. J., 2001, , 561, 708
- Walker I. R., Mihos J. C., Hernquist L., 1996, , 460, 121

Weinmann S. M., Kauffmann G., von der Linden A., De Lucia G., 2010, , 406, 2249

Wetzel A. R., Tinker J. L., Conroy C., 2012, , 424, 232

Wetzel A. R., Tinker J. L., Conroy C., van den Bosch F. C., 2013, , 432, 336

Wiersma R. P. C., Schaye J., Smith B. D., 2009a, , 393, 99

Wiersma R. P. C., Schaye J., Theuns T., Dalla Vecchia C., Tornatore L., 2009b, , 399, 574

Zabludoff A. I., Mulchaey J. S., 1998, , 498, L5

van den Bosch F. C., Aquino D., Yang X., Mo H. J., Pasquali A., McIntosh D. H., Weinmann S. M., Kang X., 2008, , 387, 79

4 Too dense to go through: The importance of low-mass clusters in satellite quenching

Summary*

In this Chapter, we study the evolution of satellite galaxies in clusters of the C-EAGLE simulations, a suite of 30 high-resolution cosmological hydrodynamical zoom-in simulations based on the EAGLE code. We find that the majority of galaxies that are quenched at $z = 0$ ($\gtrsim 80\%$) reached this state in a dense environment ($\log_{10}M_{200}[M_{\odot}] \geq 13.5$). At low redshift, regardless of the final cluster mass, galaxies appear to reach their quenching state in low mass clusters. Moreover, galaxies quenched inside the cluster that they reside in at $z = 0$ are the dominant population in low-mass clusters, while galaxies quenched in a different halo dominate in the most massive clusters. When looking at clusters at $z > 0.5$, their in-situ quenched population dominates at all cluster masses. This suggests that galaxies are quenched inside the first cluster they fall into. After galaxies cross the cluster's r_{200} they rapidly become quenched ($\lesssim 1\text{Gyr}$). Just a small fraction of galaxies ($\lesssim 15\%$) is capable of retaining their gas for a longer period of time, but after 4Gyr, almost all galaxies are quenched. This phenomenon is related to ram pressure stripping and is produced when the density of the intracluster medium reaches a threshold of $\rho_{\text{ICM}} \sim 3 \times 10^{-5} n_{\text{H}} \text{ (cm}^{-3}\text{)}$. These results suggest that galaxies start a rapid-quenching phase shortly after their first infall inside r_{200} and that, by the time they reach r_{500} , most of them are already quenched.

*Based on Pallero et al. (2020), submitted to MNRAS

4.1 Introduction

Much effort has been devoted to understanding the physical processes that drive galaxy evolution. It has been well established that the environment plays a decisive role in shaping important properties of galaxies (Gunn & Gott, 1972; Dressler, 1980, 1984; Moore et al., 1996; Poggianti et al., 2001; Blanton & Moustakas, 2009); while galaxies located in low density environments typically show bluer colors and late-type morphology, galaxies located in dense environments, such as galaxy clusters, show redder colors and an early-type morphology (Gómez et al., 2003; Kauffmann et al., 2004; Poggianti et al., 2006; Moran et al., 2007; Blanton & Moustakas, 2009). Even within clusters, there are differences between the population of galaxies located on the outskirts and those in the inner, denser regions (Postman et al., 2005; Fasano et al., 2015; Haines et al., 2015; Brough et al., 2017; Cava et al., 2017).

This color/morphology-density relation can be explained as a decrease in the star formation activity of galaxies located in denser environments and it is thought to be a consequence of the cold gas depletion of the satellite population (Haynes et al., 1984; Gavazzi et al., 2006; Fabello et al., 2012; Catinella et al., 2013; Hess & Wilcots, 2013). Nevertheless, the main mechanism responsible for this gas depletion is still an open question. There are several processes that can cause a sharp decrease in the star formation activity of a galaxy. These can be broadly classified as events of ‘*mass quenching*’ and ‘*environmental quenching*’ (Peng et al., 2010). The former correspond to mechanisms related to internal galaxy processes influenced by the galaxy mass such as gas outflows driven by the presence of an active galaxy nucleus (AGN) (Croton et al., 2006; Fabian, 2012; Cicone et al., 2014), or supernova feedback and stellar winds (Larson, 1974; Dekel & Silk, 1986; Efstathiou, 2000; Cantalupo, 2010). Environmental quenching, on the other hand, refers to mechanisms related to the interaction between a galaxy and its local environment. Simulations and models have shown that, in particular for the case of galaxy groups and clusters, the main mechanisms associated to environmental quenching can be separated into three broad categories (for details see Boselli & Gavazzi, 2006; Jaffé et al., 2016): gravitational interactions between galaxies, gravitational interactions between cluster and galaxies and interactions between galaxies and the intra-cluster medium (ICM).

It is expected that at least some of these mechanisms act simultaneously, thus rendering the characterization of galaxy quenching in dense environments challenging. Nevertheless, over the last decade several studies have suggested that ram pressure and starvation are the main drivers responsible for environmental quenching (De Lucia et al., 2012; Wetzel et al., 2013; Muzzin et al., 2014; Wetzel et al., 2015; Peng et al., 2015; Foltz et al., 2018). Wetzel et al. (2012) presented a model in which quenching is driven in a ‘*delayed-then-rapid*’ fashion in which galaxies, after its infall into a massive halo, keep forming stars as a central for several Gyr and, once the satellite star formation quenching begins, occurs rapidly.

In a recent observational study, Roberts et al. (2019, hereafter R19) showed that, inside clusters, galaxies experience what they call a ‘*slow-then-rapid*’ quenching scenario, especially for low mass galaxies. In the scenario proposed by R19, when a galaxy first enters the virial radius, R_{vir} , of a cluster it starts a slow quenching phase that can last between 1-2.5 Gyr until the galaxy reaches a region where the characteristic density of the ICM reaches $\rho_{\text{ICM}} \sim 10^{-28.3} \text{gr cm}^{-3}$ ($\sim 3 \times 10^{-5} n_{\text{H}} \text{cm}^{-3}$). At this point the galaxy starts a rapid quenching phase, that can take between 0.5-1 Gyr. The authors suggest that this rapid quenching phase could be associated to ram pressure stripping events, but this is hard to conclude from observations alone.

Cosmological simulations are a powerful tool that allows us to disentangle the effects associated with the different processes that are typically coupled in a non-linear fashion. In the last years, analytic models (Fujita, 2004; Mok et al., 2014; Contini et al., 2020), semi-analytic (De Lucia et al., 2012;

Wetzel et al., 2013; Henriques et al., 2017; Stevens & Brown, 2017; Cora et al., 2018; Contini et al., 2019) and hydrodynamical simulations (e.g. Bahé et al., 2013; Bahé & McCarthy, 2015; Taylor et al., 2017; Wright et al., 2019; Pallero et al., 2019; Donnari et al., 2020) have allowed us to explore the relative importance of the different mechanisms that bring a galaxy to a final quenched state. In the previous Chapter, we studied the satellite population of galaxy clusters in the publicly available data from the EAGLE simulation.

My main findings from the previous Chapter is that cluster satellite galaxies reach their quenching state preferentially in dense environments such as massive galaxy groups or low-mass galaxy clusters. This holds even for galaxies that become quenched before their infall into the $z = 0$ host cluster and those that suffer strong drops in their SFR (but not get completely quenched) prior to their infall to any cluster. Also, I found that the quenched fraction in $z = 0$ cluster satellites grows significantly after the first r_{200} crossing. However, this trend depends strongly on the cluster mass, with low mass clusters showing the largest increase of the quenched fraction during satellite infall. Here the aim is to determine the physical mechanisms behind satellite quenching during the r_{200} crossing, and to understand why low mass clusters seem to play a larger role on this phenomenon.

Unfortunately, our study suffered from low number statistics as EAGLE only included 10 low and intermediate mass clusters. In this Chapter, we will add new evidence to address these open issues, and to disentangle the mechanisms that finally lead to quenching of the star formation in the satellite population of galaxy clusters.

To this end, we present a detailed study of the quenching history of the satellite population in galaxy clusters from the CLUSTER-EAGLE simulations (Bahé et al., 2017; Barnes et al., 2017b), a set of zoom-in high resolution hydrodynamical simulations of 30 galaxy clusters spanning a mass range of $14 \leq \log_{10} M_{200}^{z=0} [M_{\odot}] \leq 15.4$. Thanks to the wide mass range of the modelled clusters, the same mass resolution as EAGLE simulations, and an improved time resolution at low z , C-EAGLE is an ideal laboratory to study which is the dominant quenching mechanism associated with environmental quenching. This Chapter is organized as follows. Section 4.2 contains a brief summary of the simulations and a description of the method to identify structures in space and time. In Section 4.3 we characterize the properties of each cluster and of their satellite populations at $z = 0$, and study how their properties evolve as a function of the time they spent inside clusters. In Section 4.4 we discuss how, in our models, ram pressure can account almost completely for the quenching of satellite galaxies. We also discuss the impact of numerical resolution on our results. Finally, in Section 4.5, we present a summary of our main conclusions.

4.2 Simulations

4.2.1 C-EAGLE simulations

Here we briefly summarize the main characteristics of the C-EAGLE simulations. For a more detailed description of the simulations and their subgrid model see Barnes et al. (2017b) and Bahé et al. (2017), or refer to Chapter 2.2. The C-EAGLE project comprises a suite of 30 cosmological hydrodynamical zoom-in simulations of massive galaxy clusters, spanning a mass range between $14 \leq \log_{10} M_{200}^{z=0} [M_{\odot}] \leq 15.4$. The clusters were selected from a parent N-body low resolution simulation with a box of size $(3.2 \text{ Gpc})^3$, first presented in Barnes et al. (2017a). Each zoom-in simulation was performed adopting the same flat Λ CDM cosmology that was used in the EAGLE simulation (Schaye et al., 2015; Crain et al., 2015) corresponding to $\Omega_{\Lambda} = 0.693$, $\Omega_m = 0.307$, $\Omega_b = 0.04825$, $\sigma_8 = 0.8288$, $Y = 0.248$ and $H_0 = 67.77 \text{ km s}^{-1}$ (Planck Collaboration et al., 2014).

All simulations were performed with the variant ‘AGNdT9’ of the EAGLE simulations (Schaye et al.,

2015), with a dark matter and gas mass resolution of $m_{\text{DM}} = 9.7 \times 10^6 M_{\odot}$ and $m_{\text{gas}} = 1.8 \times 10^6 M_{\odot}$, respectively. The gravitational softening was set to $\epsilon = 2.66$ comoving kpc at $z \geq 2.8$, and set to $\epsilon = 0.7$ physical kpc at $z < 2.8$. The zoom-in simulations were run with a high-resolution region extending at least to $5r_{200c}$, with the 24 galaxy clusters belonging to the HYDRANGEA sub-sample extending their high-resolution region to at least $10r_{200c}$. In this study one of the C-EAGLE clusters was removed (CE-27). This cluster experienced a very dramatic numerical AGN outburst at high redshift that significantly and artificially affected the overall properties of the system (see Bahé et al. in prep).

The code used to run these models is an upgraded version of the N-Body Tree-PM SPH code GADGET 3 (described in Springel, 2005). The modifications include updates to the hydrodynamics scheme, collectively known as ‘ANARCHY’ (see Appendix A in Schaye et al. (2015) and Schaller et al. (2015) for details) and several subgrid physics models to simulate unresolved properties. Radiative cooling and photo-heating are implemented following Wiersma et al. (2009a), assuming an optically thin X-Ray/UV background (Haardt & Madau, 2001). Star formation is implemented stochastically based on the Kennicutt-Schmidt law (Kennicutt, 1998) in pressure law form as in Schaye & Dalla Vecchia (2008), using the metallicity-dependent density threshold as in Schaye (2004). Each particle is assumed to be a single-age stellar population, with a Chabrier initial mass function in the range $0.1M_{\odot}$ - $100M_{\odot}$ (Chabrier, 2003).

Stellar evolution is modelled following Wiersma et al. (2009b), and chemical enrichment is followed for the 11 elements that most contribute to radiative cooling (i.e., H, He, C, N, O, Ne, Mg, Si, S, Ca, and Fe). The thermal energy released by stellar feedback is stochastically distributed among the gas particles surrounding the event without any preferential direction (Dalla Vecchia & Schaye, 2012).

4.2.2 Halo Identification

The main outputs from each simulation correspond to 30 snapshots spaced between $z = 14$ and $z = 0$, 28 of them equidistant in time with a $\Delta t = 500$ Myr. Two additional snapshots at $z = 0.366$ and $z = 0.101$ were added to facilitate comparisons with EAGLE. All these outputs were later post-processed to identify structures in each snapshot using the SUBFIND algorithm (Springel et al., 2001; Dolag et al., 2009) in a two-step procedure, as described below.

In order to define bound halos, first a friends-of-friends algorithm (FoF) is applied to all dark matter particles using a linking length $b = 0.2$ times the mean interparticle distance. Baryons are then assigned to the FoF (if any) associated to their nearest dark matter particle. If a FoF halo possess fewer than 32 dark matter particles, it is considered as unresolved and discarded. As a second step, SUBFIND identifies any gravitationally self-bound substructures (or ‘subhaloes’) within a FoF halo taking dark matter and baryons into consideration. These subhaloes are identified as local overdensities using a binding energy criterion. For a more detailed description of the method, we refer to Springel et al. (2001) and Dolag et al. (2009).

SUBFIND identifies structures at a single point in time. Since we need to follow galaxies both in space and time an additional procedure is required to create merger trees. The trees analyzed in this work were obtained with the SPIDERWEB algorithm (see Bahé et al., 2019, Appendix A). Differently to other ‘merger tree’ algorithms, SPIDERWEB was designed with the purpose to identify descendants for as long as possible in crowded environments. For that purpose, SPIDERWEB consider as descendants all subhaloes that share particles between consecutive snapshots. This treatment become especially relevant in groups and cluster of galaxies, where galaxy-galaxy encounters become more common. Throughout this paper, we will define as galaxies all those subhalos that possess a stellar mass $M_{\text{star}} > 10^8 M_{\odot}$, and a total mass $M_{\text{galaxy}} > 10^9 M_{\odot}$. Nevertheless, as shown in Bahé et al. (2017), C-EAGLE

possess an excess of quenched galaxies at the low mass end, probably due to numerical resolutions effects. In order to avoid spurious results, we will neglect the population of low mass galaxies that reach their quenching state as centrals, and only take into account those galaxies that reach their quenched state as satellites. Nonetheless, regardless of the cluster mass, galaxies that reach their quenching state while centrals correspond to less than 10% of all the galaxies in our cluster sample. The galaxies in our sample correspond to those satellite galaxies that are inside the r_{200} of the most massive structures of each zoom-in simulation at $z = 0$.

4.2.3 Ram Pressure and Restoring Force models

In order to measure the instantaneous ram pressure experienced by cluster satellites galaxies we follow the methodology described in Vega-Martínez et al. 2021. They introduce a general analytic profile for the instantaneous ram pressure experienced by satellite galaxies that is a function of their host mass and redshift. The profile is described by a damped power law as:

$$P_{\text{ram}}(M, z) = P_0(z) \left[\frac{1}{\xi(z)} \left(\frac{r}{R_{200}} \right) \right]^{-\frac{3}{2}\alpha(M, z)}.$$

This depends directly on r/r_{200} , the relative distance of the satellite galaxy from the halo center. $P_0(z)$ sets the normalization of the profile; $\xi(z)$ determines the radial scaling, and the exponent $\alpha(M, z)$ regulates the dependence on the host halo mass according to

$$\alpha(M, z) = \alpha_M(z) \log(M_{200} h^{-1} [\text{M}_\odot]) - 5.5.$$

Thereby, the shape of the profile is fully described by $P_0(z)$, $\xi(z)$, and $\alpha_M(z)$. Their dependence with the redshift is expressed in terms of the scale factor $a = 1/(1+z)$, as follows:

$$\log \left(\frac{P_0(z)}{10^{-12} h^2 \text{dyn cm}^{-2}} \right) = 7.01 a^{-0.122} - 9.1,$$

$$\xi(z) = -3.4 a^{-0.42} + 10.2,$$

$$\alpha_M(z) = 3.3 \times 10^{-3} a^{1.33} + 0.512.$$

The numerical values in these relations were obtained from a χ^2 minimization to fit ram pressure measurements from hydrodynamical resimulations of groups and clusters of galaxies. Given the low scatter found in the relation by the authors, and given the great agreement between the values found with this method and direct measurement inside the clusters in our $z = 0$ sample, throughout this work we will use this expression to estimate the ram pressure acting on our satellite galaxies at any time. A galaxy will suffer ram pressure stripping once the ram pressure overcomes the restoring force exerted by the galaxy itself. To measure the restoring pressure, we follow the methodology presented in Simpson et al. (2018). The restoring force per area on the satellite's gas can be expressed by

$$P_{\text{rest}} = \left| \frac{\partial \Phi}{\partial z_h} \right|_{\text{max}} \Sigma_{\text{gas}},$$

where Φ corresponds to the gravitational potential, z_h correspond to the direction motion of the gas (and in opposite direction the gas displacement), $|\partial \Phi / \partial z_h|_{\text{max}}$ is the maximum of the derivative of Φ along z_h , and Σ_{gas} is the surface gas density of the satellite (Roediger & Hensler, 2005). We adopt a simple estimate for both $|\partial \Phi / \partial z_h|_{\text{max}}$ and Σ_{gas} that can be applied to all the galaxies in our

sample regardless of their morphology. We will measure $|\partial\Phi/\partial z_h|_{\max}$ as v_{\max}^2/r_{\max} , where v_{\max} is the maximum circular velocity of the galaxy and r_{\max} is the distance to the center of the galaxy where the maximum circular velocity is reached. For the gas surface density, we will measure it using $\Sigma_{\text{gas}} = M_{\text{gas}}/\pi(2r_{1/2}^{\text{gas}})^2$, where M_{gas} is the total gas mass of the galaxy and $(r_{1/2}^{\text{gas}})$ is the 3D radius enclosing half of the gas mass.

4.3 Properties of clusters: Quenched population and gas density profiles

As previously discussed, it is well established that the environment can play an important role quenching the star formation activity of galaxies, especially within the inner and denser environments of clusters. But the way in which the mechanisms associated with environmental quenching lead to the final quenching state is still an open question. In this work we want to study the relation between the local density of the ICM and the moment of quenching for the satellite population. Several criteria have been used in the past to select quenched galaxies. Following previous studies, we use a threshold in specific star formation rate (sSFR), defined as the instantaneous star formation rate (SFR) divided by their total stellar mass (M_*) (Weinmann et al., 2010; De Lucia et al., 2012; Wetzel et al., 2012, 2013) such that if a galaxy satisfies *i*) that its $\text{sSFR} \leq 10^{-11}\text{yr}^{-1}$ and *ii*) it never reaches a sSFR greater than that threshold value again, it is classified as quenched. It is worth mentioning that we tried a different threshold sensitive to redshift to split our sample between star-forming and quenched galaxies, following Davé et al. (2019). Using this criterion, a galaxy is classified as quenched if its $\text{sSFR} \leq 10^{-10.8+0.3z}\text{yr}^{-1}$. We found none or little differences in our results. In order to make our results directly comparable with previous works, we choose to keep the fixed sSFR threshold.

In the previous chapter I studied the quenching history of the satellite population of galaxy clusters in the EAGLE simulation. I will use the same quenching classification criteria throughout this Chapter.

4.3.1 Quenching of the star formation

Because of their high resolution and wide range of halo masses, spanning from groups to clusters, the C-EAGLE re-simulations are an excellent laboratory to understand the different environmental processes that affect the quenching of star formation and its dependence on cluster mass. Under the assumption that more massive clusters are associated with denser environments, we first search for correlations between the properties of galaxies at their quenching time and the mass of the halo where they reach their quenching state.

Following what was done in the previous Chapter, and to improve the number statistics of our results, we stack galaxy in four bins of host cluster mass $M_{200}(z=0)$. On Chapter 3, I split the 10 most massive halos in the EAGLE simulations in three bins of mass, ranging from $14 < \log_{10}M_{200}/M_{\odot} < 14.8$, and found significant differences between the properties of satellites residing in the lowest and highest cluster masses at quenching. Taking advantage of the larger C-EAGLE sample, we will be able to see if the trend previously found, will prevail at higher masses. To this end we split our $z=0$ cluster sample as follows:

- High mass: $14.9 < \log_{10}M_{200}/M_{\odot} < 15.4$
- Intermediate-high mass: $14.6 < \log_{10}M_{200}/M_{\odot} < 14.9$
- Intermediate-low mass: $14.3 < \log_{10}M_{200}/M_{\odot} < 14.6$
- Low mass: $14.0 < \log_{10}M_{200}/M_{\odot} < 14.3$.

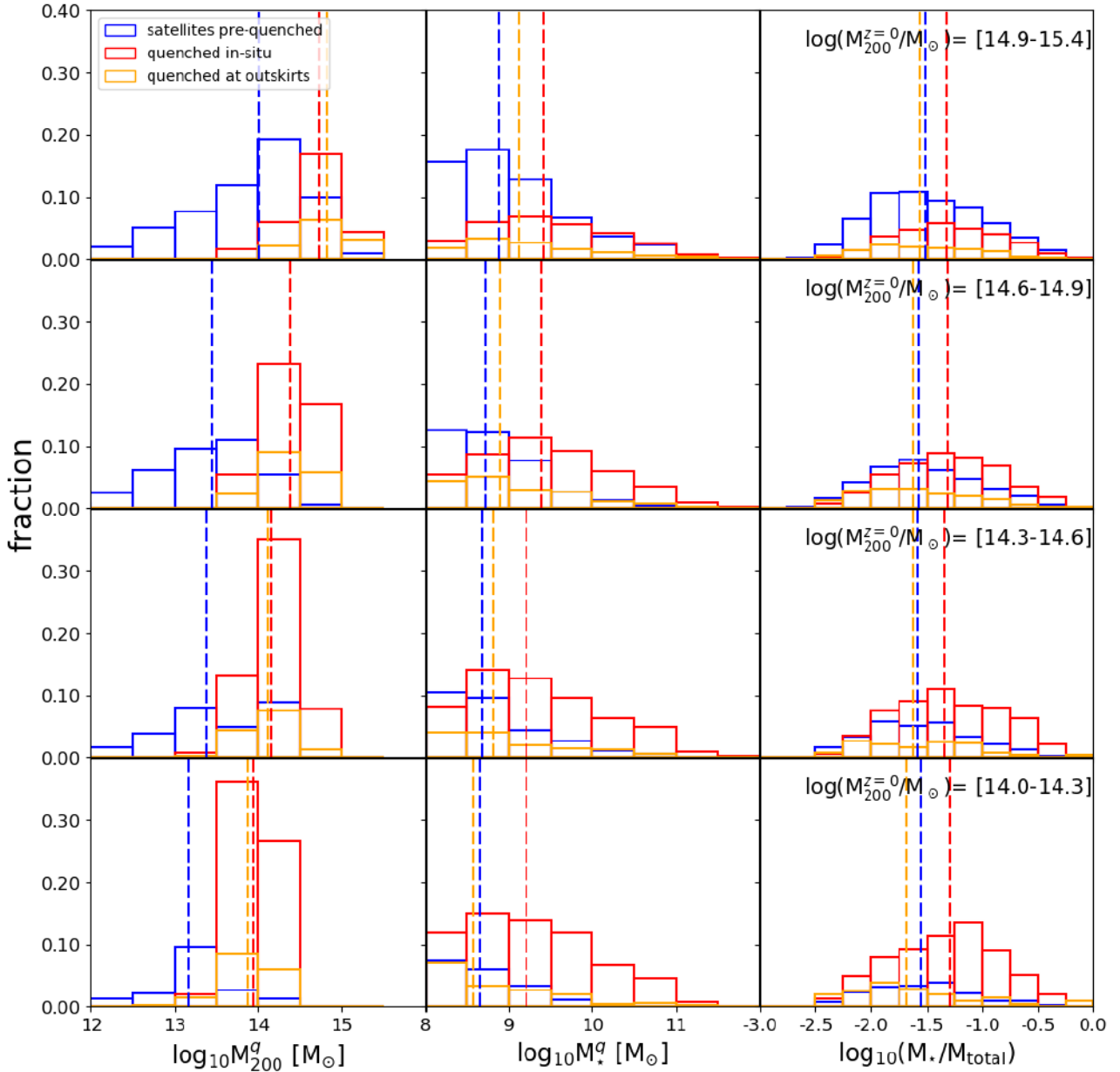


Figure 4.1: Mass distribution of galaxies and their hosts at the moment when they quench. Each row corresponds to the results obtained after stacking the distribution of galaxies associated with clusters within (from upper to lower row) high, intermediate-high, intermediate-low and low mass bin respectively. The left column shows the mass distribution of the host of each galaxy at the moment of quenching. The middle column shows the distribution of galaxies’ stellar mass at quenching time and the right hand column shows the distribution of stellar mass fractions. The galaxies are separated into ‘pre-quenched as satellites’ (blue), ‘quenched on cluster outskirts’ (orange), and galaxies ‘quenched in-situ’ (red). We can see that there is a trend between the $z = 0$ cluster mass and the halo mass at the quenching time for the satellite population. Nonetheless, independent of the M_{200} , more than 80% of cluster galaxies get quenched inside a halo with $M_{200} \geq 10^{13.5} M_{\odot}$.

The number of clusters in each mass bin from high to low mass is 8, 8, 6 and 7, respectively. To characterize the relation between the environment in which galaxies reside and the quenching of their star formation, we will further split our galaxy sample as follows:

- Pre-quenched as satellites: quenched as satellites of another structure, i.e., outside the cluster.
- Quenched on cluster outskirts: satellites quenched outside clusters r_{200} but while part of the cluster FoF.
- Quenched in-situ: satellites quenched inside the r_{200} of the final cluster.

Figure 4.1 shows the distribution of $z = 0$ satellite properties at their quenching time, t_q , for the four cluster mass bins. From top to bottom we show the results for *high*, *intermediate-high*, *intermediate-low* and *low* cluster mass bins respectively. In each panel, blue, orange and red histograms represent the population of satellites pre-quenched as satellites, quenched on cluster outskirts, and quenched in-situ, respectively. Each histogram is normalized by the total number of satellite galaxies per cluster mass bin. The dashed lines correspond to the median of each population.

In the left column we show the distribution of satellite host mass at their t_q . We can see that, regardless of the mass of the cluster, quenching tends to happen in high-mass haloes. We find that the typical host mass at the time of quenching increases with $z = 0$ cluster mass; this change is more appreciable in the pre-quenched population. However, note that the bins in these histograms are 0.5 dex wide; i.e. the peak of the distribution is in-between $13 \leq \log_{10} M_{200}/M_{\odot} \leq 14.5$, and correspond to the typical mass range for low mass clusters. We will further explore this in detail in Section 4.3.2. From the pre-quenched satellite population, we see that the peak in the host mass distribution at t_q moves from galaxy groups at the low-mass bin to low-mass clusters at the high-mass bin. This is a consequence of the hierarchical nature in which the clusters in our simulations are built. This result also shows that galaxies that arrive already quenched to the present-day clusters reached their quenched state earlier, when they entered another massive halo ($\log_{10} M_{200}/M_{\odot} \geq 12.0$).

The middle and right columns show the total stellar mass (M_{\star}) and the stellar mass fraction for the galaxies at their t_q . The stellar mass fraction is defined as the stellar mass divided by their total mass, $M_{\star}/M_{\text{galaxy}}$. Galaxies quenched in-situ show a higher stellar mass and stellar ratio compared to the pre-quenched and quenched at the outskirts populations. Moreover, galaxies that quenched on the outskirts of their $z = 0$ clusters follow the same distribution as galaxies quenched as satellites of other clusters than their $z = 0$ host, in both their stellar mass and stellar mass fraction. This suggests that the mechanisms affecting these two populations are similar.

As previously discussed, more than 60% of the galaxies quenched in our sample reach this state in groups or low mass clusters; i.e. with $13.5 \leq \log_{10} M_{200} [M_{\odot}] \leq 14.5$. This suggests that satellites get quenched after their first interaction with the ICM of structures within this mass range, independently of any subsequent mergers into more massive clusters. As massive clusters grow by the accretion of lower mass structures, most galaxies arrive in the final cluster already quenched in less massive progenitors. In the following sections we will study and discuss the possible physical processes that can lead to the quenching of galaxies in these structures.

Figure 4.2 quantifies the relative abundances of the pre-quenched and in-situ quenched satellite populations. To increase the satellite number statistics, and to obtain more reliable trends, we bin our cluster sample in 10 sets based on their M_{200c} at $z = 0$. We divide the 29 available clusters in ten sets of three, with the exception of the most massive set that contains only two clusters. The figure shows the difference between the fraction of in-situ quenched and pre-quenched satellites,

$$\frac{N_q^{\text{insitu}} - N_q^{\text{preq}}}{N_{\text{total}}} = f_{\text{insitu}} - f_{\text{preq}},$$

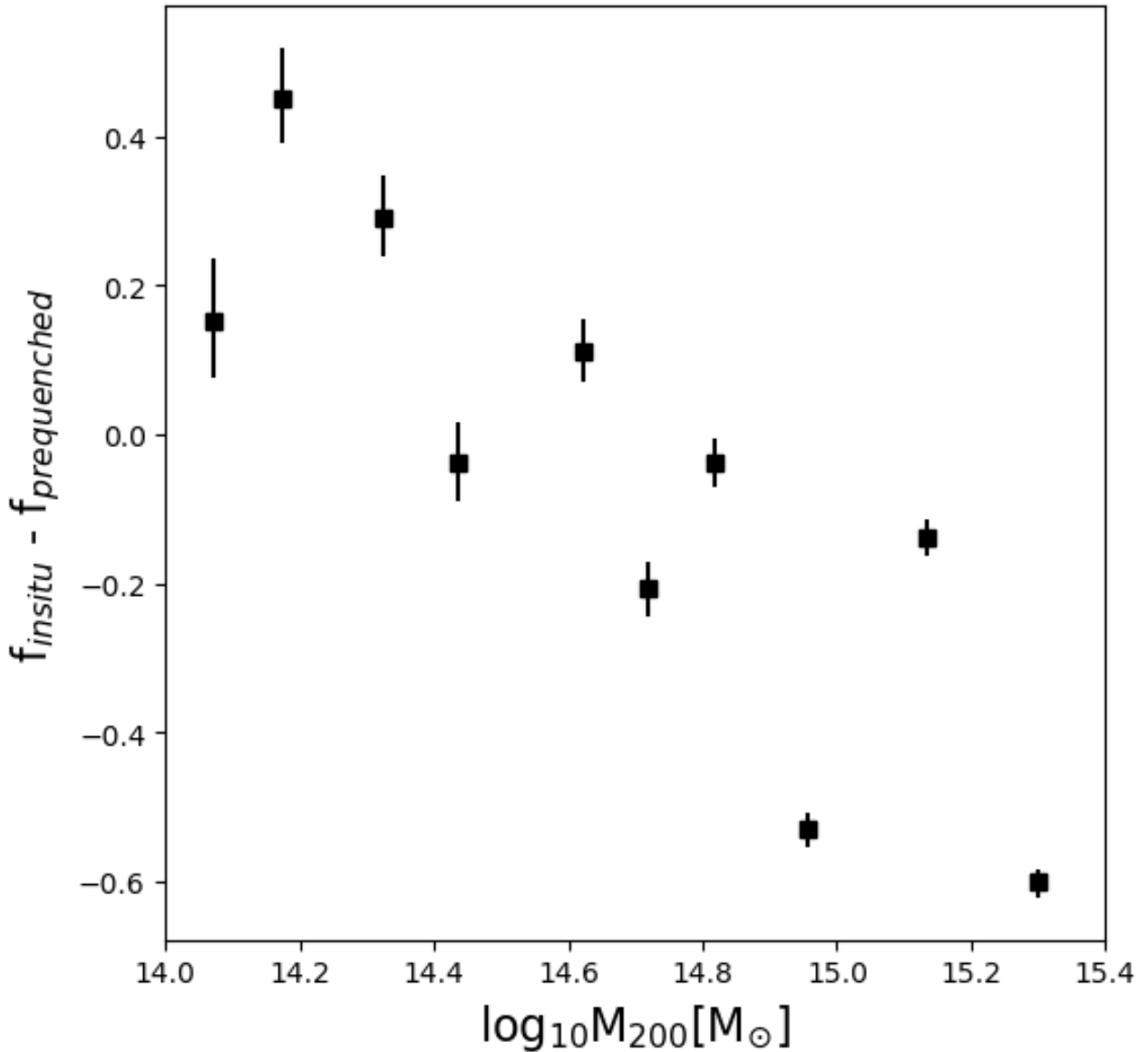


Figure 4.2: Variation of the fraction between the population pre-quenched as satellites and the population of galaxies quenched inside the cluster's r_{200} ($f_{\text{insitu}} - f_{\text{pre-quenched}}$) as a function of their halo cluster mass. Each dot represents a triplet of clusters ranked by mass. The halo mass plotted corresponds to the average of each group of three clusters, with the exception of the most massive bin, in which only two clusters were used. The error bar correspond to the binomial error associated with each measurement. In this plot we can see that the predominant population changes as the cluster mass grows. This result supports the scenario where low mass clusters are responsible for the high pre-quenching fraction found in high mass clusters.

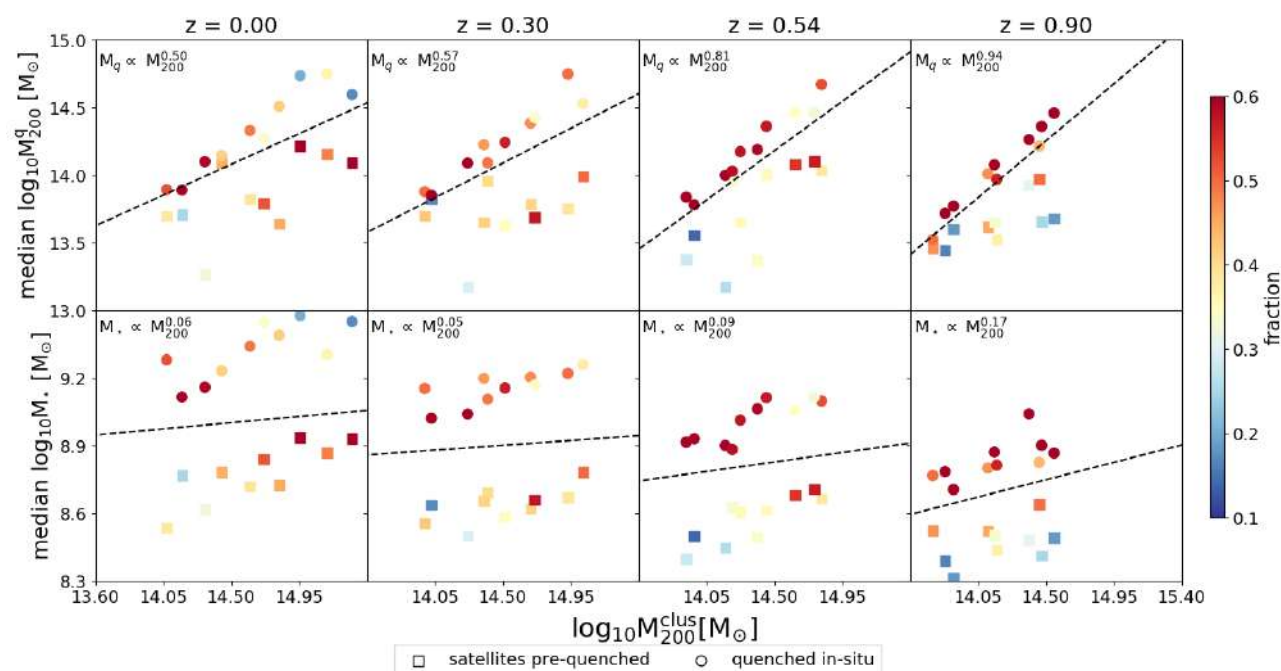


Figure 4.3: Median of the halo and stellar mass for the satellite galaxies at their quenching time as a function of their halo mass at $z = 0.0$; 0.30 ; 0.54 ; 0.90 (from left to right). Squares represent the median of the pre-quenched population while the circles represent the population quenched in-situ. Each dot represents a triplet of clusters ranked by mass, color-coded by the fraction that the pre-quenched or in-situ quenched population represents in a given bin of mass and redshift from the whole population for those clusters. Additionally, a fit to the whole population is plotted in dashed black lines. As we look at higher redshift clusters, in-situ quenching becomes dominant, and the median of the halo mass where galaxies are quenched is similar to the mass of the cluster itself. As we go down in redshift pre-quenching becomes dominant. This highlights the fact that galaxies reach their quenching state in the first transition from central to satellite galaxy. Regarding the stellar mass, as we look at galaxies at higher redshift, the stellar content is reduced systematically, while the slope of the fit shows a mild systematic growth.

as a function of the mean M_{200c} of each bin. The error bar on each dot corresponds to the binomial error associated with each measurement. This figure clearly shows that for low mass clusters, galaxies quenched in-situ are the predominant population. On the other hand, for high mass clusters the population of pre-quenched satellites becomes highly dominant. At $M_{200}^{z=0} \sim 10^{14.6} M_{\odot}$ the dominant population changes from insitu-quenched dominated to pre-quenched dominated. It should be noted that more than 60% of cluster galaxies that are quenched at present day reached this state in structures with $13.5 \leq \log_{10} M_{200} [M_{\odot}] \leq 14.6$.

4.3.2 Clusters at different times

In this Section we explore the evolution of the cluster satellite properties over a range of redshifts $0 < z < 1$, typical for current photometric surveys. As in previous sections, we study the satellite population of the most massive structures in each zoom-in simulation, at each redshift. It should be noted that their corresponding satellite galaxies can be different from the $z = 0$ population, as many of them will be disrupted before the present day (but see Bahé et al., 2019), while others will be accreted after the selected redshift. We choose to compare the satellite population of clusters at four

different times: $z = 0.90, 0.54, 0.30$ and $z = 0$. These correspond to lookback times of 7.5, 5.5, 3.5 and 0.0 Gyr, respectively. As before, for each satellite galaxy we record the values of their total stellar mass and the host halo mass at their corresponding t_q .

The top panels of Figure 4.3 show the relation between the median host mass when satellites quench and the mass of the cluster they belong to at the corresponding z . The different columns show the results at the four redshifts considered. Each symbol represents the median of the distribution, \bar{M}_{200}^q ; squares and circles represent the population of pre-quenched and in-situ quenched satellites, respectively. As before, clusters have been combined into 10 mass bins. Thus, each symbol represents the population of satellites of 3 clusters (2 in the last bin). The color coding indicates the fraction that each population represents with respect to the total, at the given redshift. For clarity, galaxies quenched as centrals are not shown in this figure. Nevertheless, they are considered when estimating the percentage that each population represents.

In the top left panel we show the relation between \bar{M}_{200}^q and the cluster's M_{200} at $z = 0$. The panel shows a mild growth of \bar{M}_{200}^q with $z = 0$ cluster mass. The dashed lines show the result of a linear regression fit, obtained combining all satellites inside each cluster-mass bin, regardless of whether they were quenched in-situ or pre-quenched. Not surprisingly, this relation is clearly stronger for the in-situ quenched than for the pre-quenched satellites. From the color coding we can also see that, at $z = 0$, the dominant population changes with cluster mass (see also Fig. 4.2). For low $z = 0$ cluster masses, most satellites were quenched in-situ, while for their high mass counterparts satellites arrive to the cluster pre-quenched. However, the values of \bar{M}_{200}^q are all within the mass range of low mass clusters, i.e. $\log_{10} M_{200} [\text{M}_\odot] \sim 14.0$.

As we move towards higher redshift, we can clearly see that the slope of the fit increases, reaching a value ≈ 1 at $z = 0.9$. In section 4.4.1 we will study in detail the mechanisms that produce this trend. Note that the most massive structures at this z have $M_{200} \sim 10^{14.6} \text{M}_\odot$. Interestingly, according to Fig. 4.2, this mass corresponds to the transition where the pre-quenched population at $z = 0$ becomes dominant over the in-situ quenched satellites. A comparison between the left and right top panels ($z = 0$ and $z = 0.9$, respectively) shows that, even at this transition mass, the in-situ quenched population is more dominant at high than low redshifts. This could be produced by the different assembly histories that clusters at $z = 0.90$ and $z = 0.00$ have experienced. High redshift clusters have mainly accreted star forming galaxies residing in low mass structures, while low redshift clusters were able to grow by the accretion of more massive, pre-quenched substructures.

In the bottom panels we show the median of the galaxies' stellar mass distribution, \bar{M}_* , at their quenching time. Here we find clear correlation (but a very mild one) between \bar{M}_* and the cluster mass. Instead, we find a correlation between \bar{M}_* and redshift, independently of the cluster mass. Similar to what was found in the previous section, a difference of 0.5 dex in \bar{M}_* between the pre-quenched and the in-situ quenched population is found at all z .

In order to highlight the role played by the environment in the quenching of the star formation activity of satellites, in Figure 4.4 we show, for each cluster, the satellite quenched fraction as a function of satellite accretion time onto the corresponding cluster. The panels show the results obtained at different z . Each line is associated to one of the 29 simulated clusters, and the color coding indicates the cluster M_{200} at the given z . Following P19, to generate this figure we computed, for each galaxy within the cluster R_{200} (at the corresponding z), the time (t_{infall}) when it first crossed the cluster's R_{200} . We then define, for each galaxy, the variable $t - t_{\text{infall}}$, and identify the moment when it became quenched on this new time scale. Finally, we compute the cumulative quenched galaxy fraction as a function of $t - t_{\text{infall}}$.

The bottom right panel of Fig 4.4 shows the result obtained at $z = 0$. For all clusters we find that the satellite quenched fraction rises rapidly after intall ($t - t_{\text{infall}} > 0$), regardless of cluster mass. The

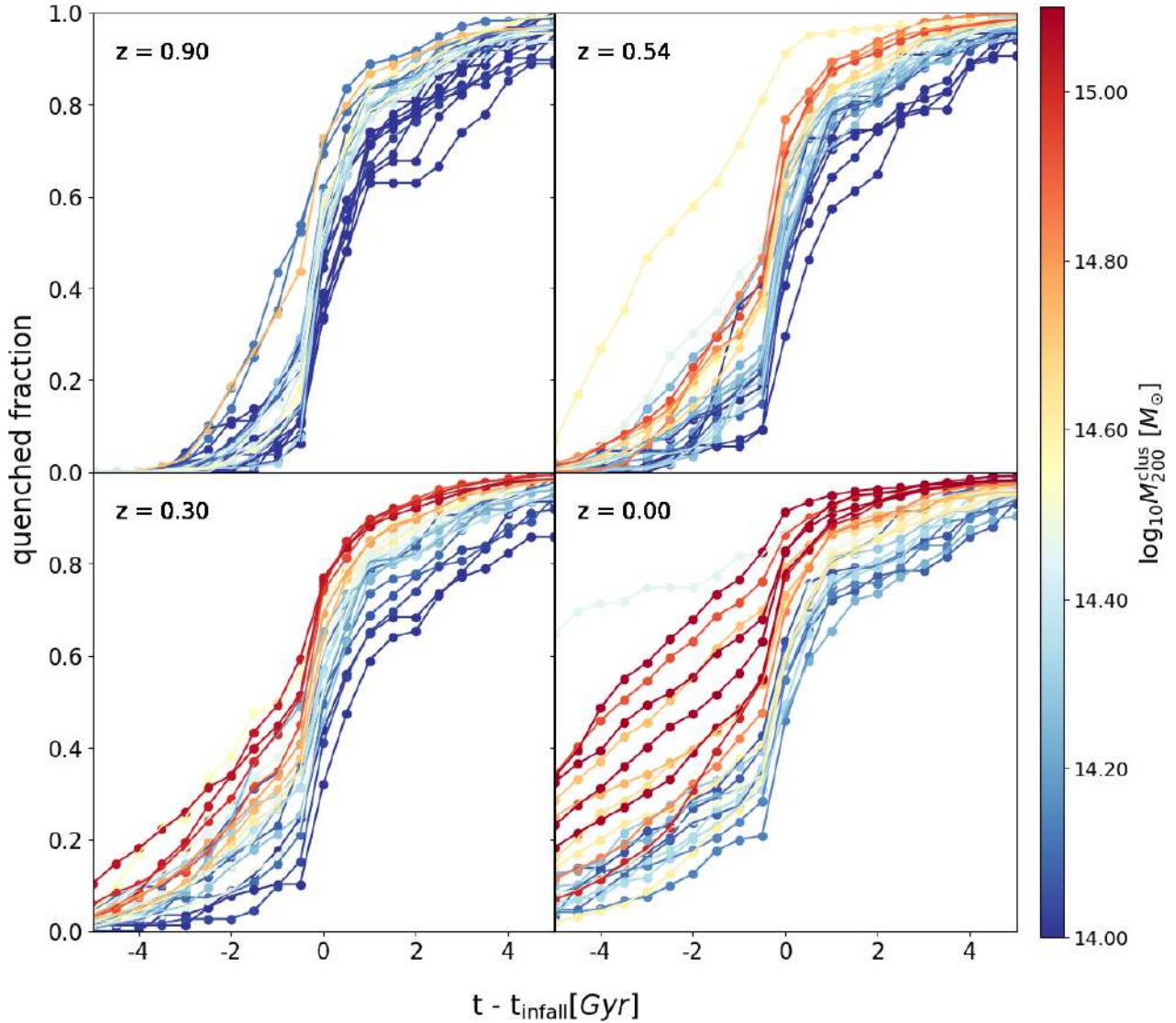


Figure 4.4: Growth of the quenched fraction of the satellite population of galaxy clusters as a function of the normalized timescale $t - t_{\text{infall}}$ for clusters at $z = 0.00; 0.30; 0.54; 0.90$. Each line represents one cluster in the simulation, color-coded by their M_{200} at the given redshift. Negative (positive) values correspond to times before (after) the first crossing of the R_{200} of the final cluster. As we look at clusters at higher redshift, we can see that the fraction of pre-quenching is reduced significantly ($t - t_{\text{infall}} < 0$). At the time of their infall ($t - t_{\text{infall}} = 0$) we can see a sharp increase in quenching and an abrupt change in the slope of the fraction of quenched galaxies. This result is even clearer when looking at higher redshifts, where even the most massive clusters present a rise in the quenched fraction $\gtrsim 60\%$ when $-1 \lesssim t - t_{\text{infall}} \lesssim 1$. As we decrease the redshift, the fraction of pre-quenching increases, especially for the most massive clusters, which at $z = 0.30$ presents $> 50\%$ of their galaxies already quenched before accretion. And by $z = 0$, clusters with $M_{200} \geq 10^{15} M_{\odot}$ possess a pre-quenching fraction $> 80\%$.

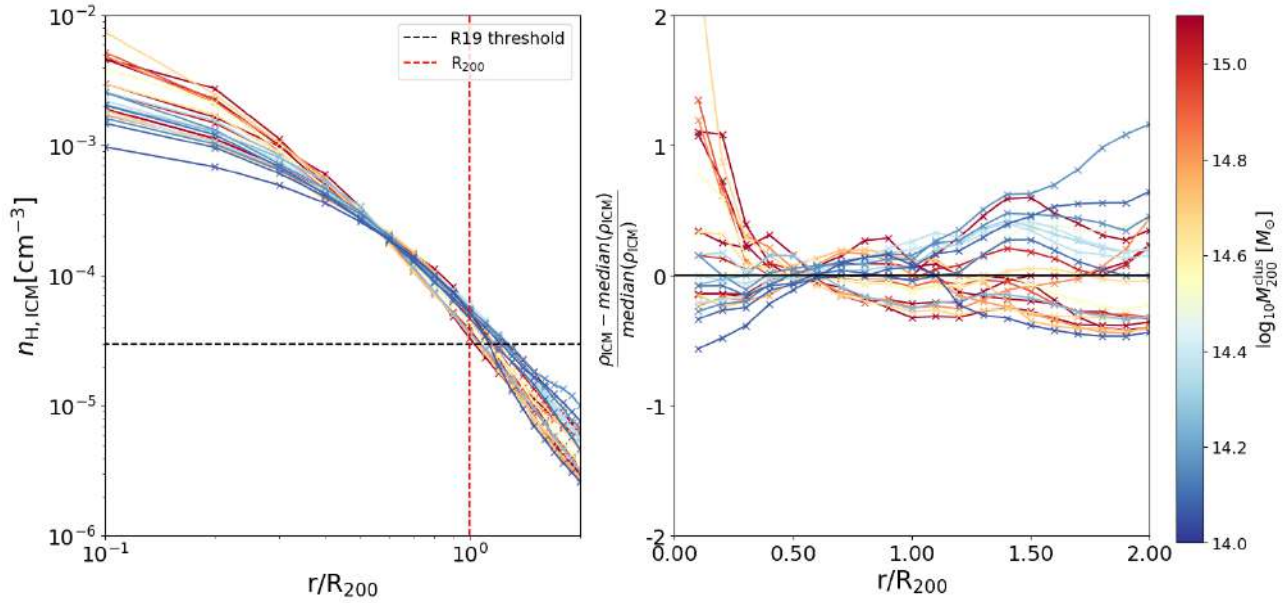


Figure 4.5: *Left panel:* Azimuthally averaged cluster gas density profiles for the $z = 0$ sample. *Right panel:* Fractional deviation from the median cluster gas density profiles. Each line is color-coded by cluster M_{200} . We can see that low mass clusters possess a more extended gas component in comparison with high mass clusters that are more concentrated. This result is more evident when looking at the normalized distribution in the right panel. Regardless of the cluster mass, the threshold in ρ_{ICM} found by Roberts et al. (2019) is reached near the r_{200} of our clusters.

jump is, however, significantly more abrupt for low mass clusters. High mass clusters show a larger fraction of quenched satellites for $t - t_{\text{infall}} < 0$ and rapidly reach a fraction of 90% after satellite infall. In general, we find that the fraction of pre-quenching varies between 20-80%, with a strong dependence on the cluster mass. Almost every satellite galaxy reaches its quenched state 4 Gyr after their accretion time (see also Chapter 3). As previously discussed, most $z = 0$ satellites get quenched while inhabiting low mass clusters and arrive to the final massive structure without any star formation activity. As a result, the ρ_{ICM} of these $z = 0$ massive clusters ($M_{200} \gtrsim 10^{14.6} M_{\odot}$) are not playing a significant role in the overall quenching of (massive) cluster galaxies in the local Universe. Instead, their main role is to end the star formation activity of that small amount of galaxies that is not accreted in a subgroup into the cluster.

As we move towards higher redshift, the fraction of satellites arriving to the clusters as star forming galaxies increases. Note that at $z = 0.9$ (top left panel) the typical pre-quenched satellite fraction is $\lesssim 20\%$, and that just after t_{infall} these fraction quickly jump to values of $\sim 70\%$. Most cluster satellites are suffering strong environmental effects for the first time in structures that are within the mass range $10^{13.5} \lesssim M_{200} \lesssim 10^{14.5} M_{\odot}$, i.e. low mass clusters (see also Fig. 4.1)

4.3.3 Gas density of the intracluster medium

Our analysis points towards a preferential cluster mass range where environmental quenching is more efficient. Interestingly, using a sample of cluster galaxies selected from the Sloan Digital Sky Survey with high-quality Chandra X-ray data, R19 found a threshold in ρ_{ICM} for quenching, likely related to the effects of ram pressure stripping. Their study shows that the fraction of quenched galaxies in dense environments grows with ρ_{ICM} . For galaxies with a stellar mass $\log_{10} M_{\star} [M_{\odot}] > 9.9$ (intermediate

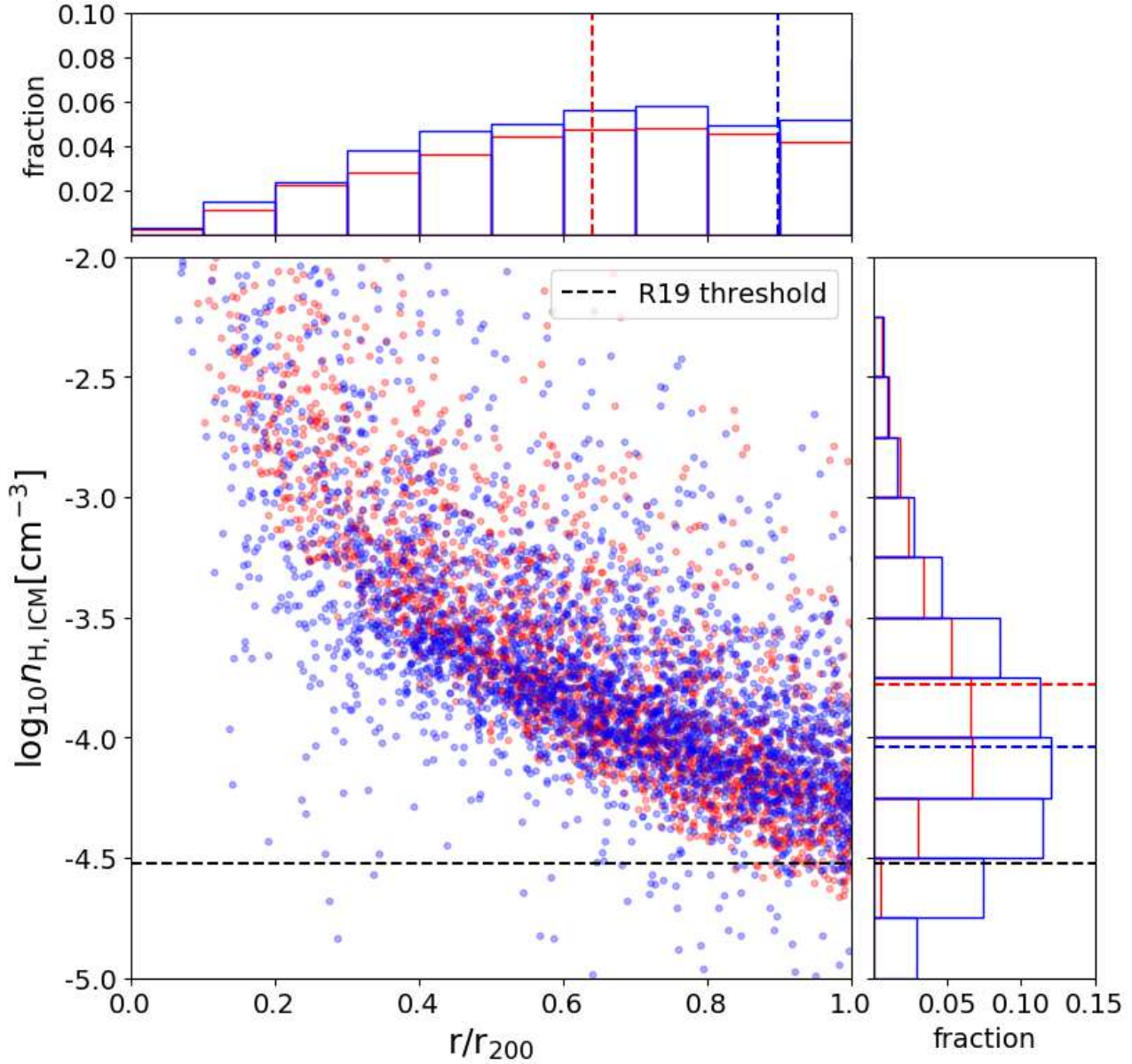


Figure 4.6: Density of the local environment in which galaxies reside at their quenching time as a function of the distance from the halo center in units of r_{200} . Blue dots correspond to galaxies that are quenched in a different halo than the final cluster (pre-quenched) and red dots correspond to galaxies quenched in the final cluster (quenched in-situ). The histograms show the distribution of density and distance separately. The black dashed lines show the threshold found in R19 and the blue and red dashed lines in the histograms correspond to the median of each distribution. We can see that the majority of the population in our sample, regardless of their status as pre-quenched or in-situ quenched, suffer quenching in high density environments ($\log_{10} n_{\text{H, ICM}} \geq 3 \times 10^{-5} [\text{cm}^{-3}]$) with the majority of the population reaching this state in the outskirts of clusters ($r > 0.5 r_{200}$).

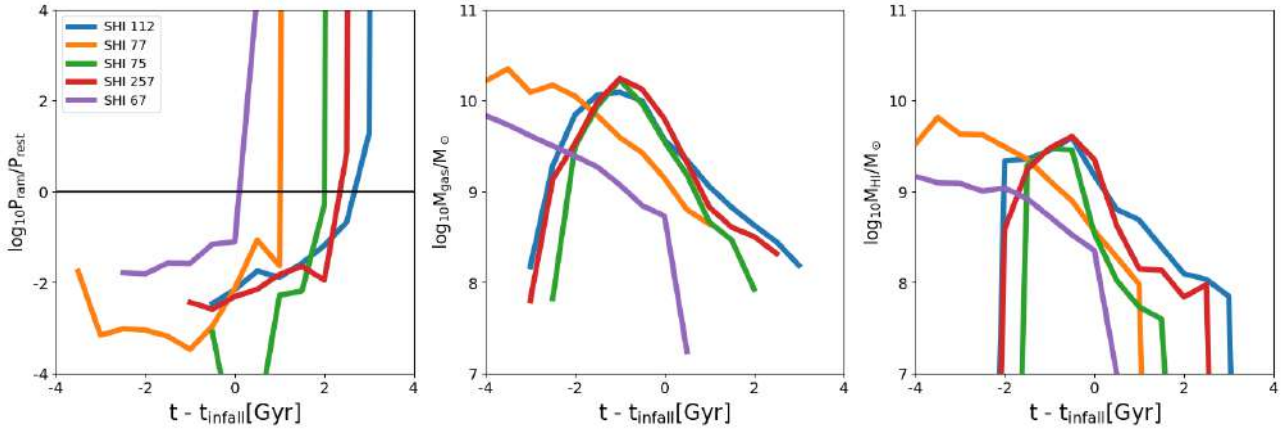


Figure 4.7: Evolution of properties for a subset of galaxies in our sample. SHI correspond to the SubHaloIndex associated with each galaxy in the zoom-in simulation CE-0. *Left*: Ratio between ram pressure and the restoring force per area, *Middle*: evolution of the total gas mass and *Right*: HI content in the galaxy, as a function of their time since accretion. The restoring force per area dominates over the ram pressure until they arrive to the cluster. At the time that galaxies become ram-pressure dominated, they lose most of their total gas content.

and high mass galaxies), the relation between the quenched fraction and ρ_{ICM} can be described with a single power law. However, for galaxies in the mass range of $9.0 < \log_{10} M_{\star} [M_{\odot}] < 9.9$ (low mass galaxies) a broken power law is needed. The ‘knee’ in this double power law is located at densities $\rho_{\text{ICM}} = 10^{-28.3} \text{ gr cm}^{-3}$ ($n_{\text{H}} = 3 \times 10^{-5} [\text{cm}^{-3}]$). According to the model presented in R19, when a galaxy reaches this density threshold it starts to experience a ‘rapid-quenching’ mode. It is worth noting that, as discussed by Simpson et al. (2018), the ICM of hosts with total masses in the range $12 < \log_{10} M_{200} [M_{\odot}] < 13$ are inefficient at quenching this type of satellites. Thus, they are bound to reach the final quenching state within the environments of low mass clusters and massive groups.

To explore this scenario with our models, in Figure 4.5 we show azimuthally averaged gas density profiles for the 24 $z = 0$ clusters of the HYDRANGEA sub-sample. Each line on the left panel corresponds to the gas density distribution of one cluster in our simulation, color-coded by their M_{200} at $z = 0$. The cluster-centric distances have been normalized by the corresponding r_{200} . Note that low mass clusters typically have relatively more extended gas distributions than their more massive counterparts. These differences are better highlighted in the right panel, where we show

$$\Delta\rho_{\text{ICM}} = \frac{\rho_{\text{ICM}} - \bar{\rho}_{\text{ICM}}}{\bar{\rho}_{\text{ICM}}}.$$

Here $\bar{\rho}_{\text{ICM}}$ represents, at each radius, the median of the distribution of ρ_{ICM} for all clusters. These panels clearly show that the distribution of gas in high mass clusters is more concentrated. These clusters also possess lower amounts of cold gas than lower mass objects.

The black dashed line on the left panel indicates the ρ_{ICM} threshold introduced by R19 and the red dashed line shows the density of each cluster at their r_{200} . In general, we find that low mass clusters reach this threshold a bit further out, $\sim 1.3 R_{200}$, than high mass clusters, at $\sim 1.0 R_{200}$. Note that, as shown in Figure 4.4 (see also Chapter 3), a drastic change in the slope of the cumulative satellite quenched fraction as a function of time takes place at $(t - t_{\text{infall}} = 0)$ Gyr; this is, during the first crossing of the clusters r_{200} .

Using the density profiles shown in Fig 4.5 we estimate, for each cluster, the local value of ρ_{ICM} at the time where in-situ quenched satellites ceased their star formation activity. These values are obtained

by interpolating the density profiles shown in Fig 4.5 at the locations where satellites are identified as quenched. We find that the peak of the local density experienced by each galaxy at their quenching time is $n_{\text{H,ICM}} \sim 1.8 \times 10^{-4} \text{cm}^{-3}$ briefly after $0.7R_{200}$ which roughly corresponds to r_{500} (Ettori & Balestra, 2009).

To extend these results to the pre-quenched population, we estimate the local densities where galaxies reach their quenching state, either in the final host or in an accreted substructure. This time we use the ram-pressure profile shown in Section 4.2.3. As discussed, ram pressure can be written as

$$P_{\text{ram}} = \rho_{\text{ICM}} v^2,$$

where ρ_{ICM} corresponds to the density of the local environment of the galaxy, and v^2 corresponds to the square of the relative velocity between the galaxy and its environment. Based on this, we estimate the local environment density using the analytic ram pressure profile and the velocity of the galaxies directly measured from the simulations. The velocity is measured as the relative velocity between the galaxy and the center of the host in which each galaxy resides at their t_q . In Fig 4.6 we show the values of the local density at which galaxies reach their quenching state as a function of the normalized distance to the host-centre at their t_q . The red dots correspond to the in-situ quenched population, while blue dots stand for the pre-quenched population. The histograms show both populations separately, and the red and blue dashed lines correspond to the median of each distribution. The dashed black line corresponds to the density threshold proposed by R19. We can see that in general, regardless of their in-situ or pre-quenched condition, galaxies reach their quenching state in a local environment denser than the threshold proposed by R19. We can also see that the majority of galaxies reach their quenched state at the outskirts of their host ($\sim R_{200}$), and just a small percentage of the whole sample the galaxies reach their quenched state in the inner parts of their hosts ($r \lesssim 0.5R_{200}$). We note that, given the time resolution of the simulation, we are not able to recover the exact moment and place where the galaxy get quenched. Also, for this particular result, we are not taking into account the time spent within the host in which they eventually get quenched. Nonetheless, as we see in Figure 4.4, galaxies get quenched shortly after their first accretion event (but see Oman et al., 2020, for observational evidence to the contrary).

4.4 Discussion

4.4.1 Ram pressure as the main culprit

The R19 ‘slow-then-rapid’ quenching scenario proposes that galaxies first experience a slow quenching phase as they approach the cluster due to what is known as starvation (Larson et al., 1980). During this phase galaxies are not able to replenish their gas reservoir and, as a result, slowly deplete their gas available to form stars. In the absence of other mechanisms, starvation would slowly lead to the final quenching of galaxies, within a typical timescale $\gtrsim 3$ Gyr (Peng et al., 2010, 2015). However, and in particular for low mass galaxies, once they reach the inner cluster region, where the intracluster-medium (ICM) reaches $\rho_{\text{ICM}} \sim 10^{-28.3} \text{gr cm}^{-3}$ ($n_{\text{H,ICM}} \sim 3 \times 10^{-5} [\text{cm}^{-3}]$), the process switches to a rapid quenching phase due to the effect of ram pressure. The ram pressure experienced by satellites in these inner regions becomes large enough to overcome their own restoring force, triggering the rapid depletion of their gas component. The typical quenching timescale in this phase is of the order of $\lesssim 1$ Gyr. As we have just shown in the previous section, this density is reached in these simulations at the outskirts of low mass clusters ($\sim R_{200}$).

In Figure 4.7, we further explore whether the rapid quenching phase we observe in our simulations is associated with the R19 ICM density threshold, $n_{\text{H,ICM}} \sim 3 \times 10^{-5} [\text{cm}^{-3}]$. In the left panel of this

figure we show the time evolution of the balance between the ram pressure and the restoring force per area felt by the satellites' gas component. As an example, we focus on a subset of randomly selected galaxies. As before, the timescale is measured as $(t - t_{\text{infall}})$. This panel shows that, after crossing the virial radius of the cluster, the influence of ram pressure rapidly grows until it completely dominates over the restoring force. The middle and right panels show the time evolution of the total gas and HI content, respectively. We can see that the gas content of these galaxies starts to slowly decrease prior to accretion (slow phase) and then rapidly drops after infall (rapid phase). To generalize these results, we show in the left panel of Figure 4.8 the cumulative fraction of galaxies dominated by ram pressure ($P_{\text{ram}} > P_{\text{rest}}$) for each cluster, as a function of their infall time. Note that ram pressure is estimated for each satellite based on the density of their environment at the corresponding time, using the methodology shown in Section 4.2.3. In other words, if galaxies are arriving to the cluster as satellites of another substructure, the ICM considered is the one associated with the corresponding substructure. For comparison, in the right panel of this figure we also show the evolution of the quenched galaxy fraction. Each line is color-coded by the cluster M_{200} at $z=0$. As we saw in the previous section, present-day satellites with masses $M_{\star} \gtrsim 10^9 M_{\odot}$ (see Fig. 4.1), in low mass clusters, tend to arrive as star forming objects but the quenched fraction grows rapidly after infall (right panel). This trend becomes progressively less pronounced as the mass of the cluster increases. The left panel of this figure shows a very similar trend when considering the fraction of satellites that are ram pressure dominated (with respect to their own restoring force). We can clearly see that, for low mass clusters, the vast majority of satellites reach the cluster's r_{200} for the first time, dominated by their own restoring force, but this abruptly changes after infall. Instead, in more massive clusters, a significant fraction of satellites are arriving already dominated by ram pressure (and already quenched). As previously discussed, and shown in Chapter 3, this is due to the accretion of larger substructures into more massive clusters, bringing a significant fraction of the present-day quenched satellite population. Nonetheless, and regardless of the mass of the cluster, we see immediately after the t_{infall} a sharp rise in the fraction of ram pressure dominated fraction ($\sim 40\%$ in the most extreme cases). As the cluster mass grows, the rise becomes less pronounced.

4.4.2 Over-quenching in C-EAGLE

It was reported in Bahé et al. (2017) that the fraction of low mass ($\log_{10}M_{\star}[M_{\odot}] \leq 9.5$) quenched galaxies in the C-EAGLE simulations is higher than observed in data. In fact, while observations show that the fraction of quenched galaxies decreases steadily as we look at lower stellar masses, in C-EAGLE this fraction rises towards low masses (See figure 6 of Bahé et al. 2017). In a similar way, the EAGLE simulations also possess higher fraction of quenched galaxies towards lower masses ($\log_{10}M_{\star}[M_{\odot}] \lesssim 9.5$), mainly due to numerical resolution artifacts (Schaye et al., 2015). Since C-EAGLE uses the same numerical code and resolution as EAGLE, Bahé et al. (2017) argue that the excess of passive galaxies found in these simulations is also mainly due to resolution effects, as over-quenching is measured only in low mass satellite galaxies. They propose that this resolution issue can be connected to the formation of large holes ($\sim 20\text{kpc}$) in the atomic hydrogen discs of many dwarf galaxies, similar to what was found in the EAGLE simulation (see Bahé et al., 2016). The limited resolution and high energetic feedback model implemented in EAGLE develop these large holes in the discs of dwarfs, making them more susceptible to ram pressure stripping events.

As we showed in the previous section, in general C-EAGLE clusters possess an extended gas envelope that makes them relatively denser than the observational clusters shown in R19, reaching the density needed for 'rapid-quenching' even at the outskirts of low mass clusters. Given all these considerations it is straightforward to conclude that the excess of dwarf galaxies quenched inside clusters is

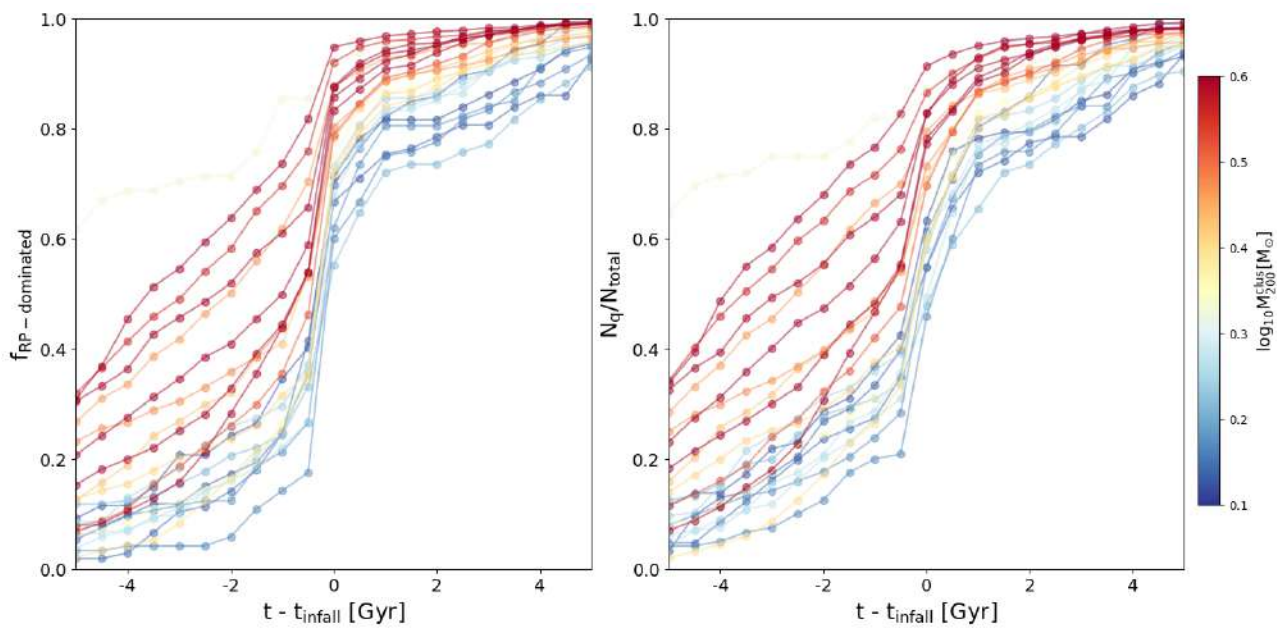


Figure 4.8: *Left:* Evolution of the ram-pressure dominated population of galaxies as a function of time since infall. *Right:* Growth of the quenched fraction of the satellite population in clusters as a function of the time since infall. Each line represents one cluster in the simulation, color-coded by their M_{200} at $z=0$. These results are coincident with the evolution of the ram pressure dominated population; as galaxies become more ram pressure dominated the quenched fraction also increases. This suggests that most galaxies quenched in our sample were quenched due to ram pressure inside clusters of galaxies.

mainly due to a combination of the extreme environment in which galaxies reside and the feedback phenomenology implemented in the code (for a more detailed explanation regarding the feedback model we refer the reader to Schaye et al., 2015; Crain et al., 2015; Bahé et al., 2017).

To address this issue, simulations containing galaxy clusters with higher resolution are needed. However no suitable simulation suites are available at present; TNG-50 (Nelson et al., 2019; Pillepich et al., 2019) and ROMULUSC (Tremmel et al., 2019) only partly fulfill this requirement. These simulations lack a statistical sample of clusters to carry out our study, with just one halo with $\log_{10}M_{*}[M_{\odot}] \geq 14$. On the other hand, simulations as the ones presented in THE THREE HUNDRED PROJECT (Cui et al., 2018), or in the TNG-300 (Marinacci et al., 2018; Naiman et al., 2018; Nelson et al., 2018; Pillepich et al., 2018; Springel et al., 2018) can be useful to statistically study the properties of galaxies inside clusters. But due to the low mass and spatial resolution, it is impossible to study in detail the mechanisms that lead to the quenching of star formation in these simulations.

4.5 Summary and Conclusions

In this Chapter, we have studied the evolution of the quenched fraction of satellites in the galaxy clusters of the C-EAGLE simulation. C-EAGLE is a suite of 30 cosmological hydrodynamic zoom-in simulations of massive galaxy clusters in the mass range of $14.0 \leq \log_{10}M_{200}/M_{\odot} \leq 15.4$ at $z = 0$, using the state-of-the-art EAGLE galaxy formation code. We select satellite galaxies with stellar mass $\log_{10}M_{*}/M_{\odot} \geq 8$ that at $z = 0$ are bound to a main cluster and are located inside the cluster's r_{200} . First, using the merger trees obtained with the SPIDERWEB post-processing software (see details in Bahé et al. 2019), we study the time evolution of the quenched population ($sSFR < 10^{-11}\text{yr}^{-1}$) as they traverse different environments. To study the quenching of star formation of galaxies inside and outside the main cluster, we define three types of populations:

- pre-quenched as satellites: quenched as satellites in a structure outside the final $z = 0$ cluster.
- quenched on cluster outskirts: quenched outside the cluster R_{200} while in cluster FoF
- quenched in-situ: quenched inside the main clusters R_{200} .

We found that regardless of the final cluster mass, most galaxies ($> 80\%$) reach their final quenching state inside dense structures ($\log_{10}M_{200}/M_{\odot} \geq 13.5$); the remaining galaxies ($\lesssim 20\%$) are quenched in a medium sized halo ($12.0 < \log_{10}M_{200}/M_{\odot} < 13.5$) as satellites. We study the relation between the median of the distribution of galaxy properties at their quenching time and the cluster final mass. The first thing to notice is that, regardless of the cluster mass, quenching occurs mainly in halos of $\log_{10}M_{200}/M_{\odot} \sim 14$; in fact, as the cluster mass increases the predominant population in our sample changes from galaxies quenched in-situ, to galaxies pre-quenched. This highlights the fact that the quenching of the star formation happens in low mass clusters rather than in the most massive structures, even though they have the environmental conditions to strip the gas reservoirs of these satellites. Most of the galaxies that these massive clusters accrete are already quenched due to their earlier accretion onto another low mass cluster.

Regarding their stellar content, galaxies quenched inside the cluster contain 0.5 dex higher stellar masses than the pre-quenched population, and show 0.3 dex higher stellar mass fraction.

We also studied the gas density profiles of clusters and the relation between the local density and the quenching suffered by satellite galaxies. Our clusters possess similar gas profiles. There are no cool-core clusters in the sample and all are widely hot-gas dominated. In general, high mass clusters show a more concentrated hot gas component, while low mass clusters exhibit a more extended envelope.

In the case of low mass clusters, they reach the critical threshold in ρ_{ICM} , discussed by Roberts et al. (2019) at $\sim 1.3R_{200}$. This suggests that galaxies in our sample experience the ‘rapid-quenching’ scenario starting at the outskirts of these clusters. When comparing to the time evolution of the quenched fraction we found that, at the moment of the first R_{200} crossing, the quenched fraction increases rapidly, with low mass clusters being the ones showing the most extreme change in this fraction; for these, the rise in their quenched fraction ($\sim 60\%$) is produced in a very short period of time ($\lesssim 1\text{Gyr}$). After this period, the fraction grows more slowly ($\sim 15\%$ within $1 \lesssim t - t_{\text{infall}} \lesssim 4\text{Gyr}$). High mass clusters contain higher fractions of quenched galaxies regardless of their accretion time. In this case, the effect of crossing the cluster’s virial radius is not as significant as in the case of low mass clusters. This is due to the earlier passage of the galaxies through the high density structure of previous substructures. Nevertheless, we still found a measurable rise in the fraction of quenched galaxies after infall into their final massive clusters. 1Gyr after infall, the fraction of quenched galaxies rises from 10% to 40%, and between [1-4]Gyrs after their infall, the fraction of quenched galaxies grows at a much slower rate than in low mass clusters ($\lesssim 10\%$). This result is slightly different at high redshift, where most of our simulated clusters are significantly less massive. At higher z , we find that most galaxies reach their quenching state in-situ, regardless of the cluster mass. This is a consequence of the different assembly history of clusters at high and low redshift. In other words, our results show that galaxies in the mass range of $9.0 < \log_{10}M_{\star}[\text{M}_{\odot}] < 9.9$ reach their quenching state inside the first dense structure they fall into. Regardless of z and cluster mass, 4Gyr after their infall, almost all galaxies ($\gtrsim 90\%$) are quenched.

Even though the excess of quenching found in our results, especially at the outskirts of clusters for low mass galaxies, can be related to the limited resolution of the simulation, we show that the ram pressure experienced by intermediate and high mass galaxies at the moment when they reach this threshold in gas density is high enough to strip their gas content, shortly after their first infall.

Bibliography

Bahé Y. M., McCarthy I. G., 2015, , 447, 969

Bahé Y. M., McCarthy I. G., Balogh M. L., Font A. S., 2013, , 430, 3017

Bahé Y. M., et al., 2016, , 456, 1115

Bahé Y. M., et al., 2017, , 470, 4186

Bahé Y. M., et al., 2019, , 485, 2287

Barnes D. J., Kay S. T., Henson M. A., McCarthy I. G., Schaye J., Jenkins A., 2017a, , 465, 213

Barnes D. J., et al., 2017b, , 471, 1088

Blanton M. R., Moustakas J., 2009, , 47, 159

Boselli A., Gavazzi G., 2006, , 118, 517

Brough S., et al., 2017, , 844, 59

Cantalupo S., 2010, , 403, L16

Catinella B., et al., 2013, , 436, 34

Cava A., et al., 2017, , 606, A108

Chabrier G., 2003, , 115, 763

Cicone C., et al., 2014, , 562, A21

Contini E., Gu Q., Kang X., Rhee J., Yi S. K., 2019, , 882, 167

Contini E., Gu Q., Ge X., Rhee J., Yi S. K., Kang X., 2020, , 889, 156

Cora S. A., et al., 2018, , 479, 2

Crain R. A., et al., 2015, , 450, 1937

Croton D. J., et al., 2006, , 365, 11

Cui W., et al., 2018, , 480, 2898

Dalla Vecchia C., Schaye J., 2012, , 426, 140

Davé R., Anglés-Alcázar D., Narayanan D., Li Q., Rafieferantsoa M. H., Appleby S., 2019, , 486, 2827

De Lucia G., Weinmann S., Poggianti B. M., Aragón-Salamanca A., Zaritsky D., 2012, , 423, 1277

Dekel A., Silk J., 1986, , 303, 39

Dolag K., Borgani S., Murante G., Springel V., 2009, , 399, 497

- Donnari M., Pillepich A., Nelson D., Marinacci F., Vogelsberger M., Hernquist L., 2020, arXiv e-prints, p. arXiv:2008.00004
- Dressler A., 1980, , 236, 351
- Dressler A., 1984, , 22, 185
- Efstathiou G., 2000, , 317, 697
- Ettori S., Balestra I., 2009, , 496, 343
- Fabello S., Kauffmann G., Catinella B., Li C., Giovanelli R., Haynes M. P., 2012, , 427, 2841
- Fabian A. C., 2012, , 50, 455
- Fasano G., et al., 2015, , 449, 3927
- Foltz R., et al., 2018, , 866, 136
- Fujita Y., 2004, , 56, 29
- Gavazzi G., O'Neil K., Boselli A., van Driel W., 2006, , 449, 929
- Gómez P. L., et al., 2003, , 584, 210
- Gunn J. E., Gott III J. R., 1972, , 176, 1
- Haardt F., Madau P., 2001, in Neumann D. M., Tran J. T. V., eds, Clusters of Galaxies and the High Redshift Universe Observed in X-rays. p. 64 (arXiv:astro-ph/0106018)
- Haines C. P., et al., 2015, , 806, 101
- Haynes M. P., Giovanelli R., Chincarini G. L., 1984, , 22, 445
- Henriques B. M. B., White S. D. M., Thomas P. A., Angulo R. E., Guo Q., Lemson G., Wang W., 2017, , 469, 2626
- Hess K. M., Wilcots E. M., 2013, , 146, 124
- Jaffé Y. L., et al., 2016, , 461, 1202
- Kauffmann G., White S. D. M., Heckman T. M., Ménard B., Brinchmann J., Charlot S., Tremonti C., Brinkmann J., 2004, , 353, 713
- Kennicutt Jr. R. C., 1998, , 498, 541
- Larson R. B., 1974, , 169, 229
- Larson R. B., Tinsley B. M., Caldwell C. N., 1980, , 237, 692
- Marinacci F., et al., 2018, , 480, 5113
- Mok A., et al., 2014, , 438, 3070
- Moore B., Katz N., Lake G., Dressler A., Oemler A., 1996, , 379, 613

- Moran S. M., Ellis R. S., Treu T., Smith G. P., Rich R. M., Smail I., 2007, , 671, 1503
- Muzzin A., et al., 2014, , 796, 65
- Naiman J. P., et al., 2018, , 477, 1206
- Nelson D., et al., 2018, , 475, 624
- Nelson D., et al., 2019, , 490, 3234
- Oman K. A., Bahé Y. M., Healy J., Hess K. M., Hudson M. J., Verheijen M. A. W., 2020, arXiv e-prints, p. arXiv:2009.00667
- Pallero D., Gómez F. A., Padilla N. D., Torres-Flores S., Demarco R., Cerulo P., Olave-Rojas D., 2019, , 488, 847
- Pallero D., Gómez F. A., Padilla N. D., Bahé Y. M., Vega-Martínez C. A., Torres-Flores S., 2020, arXiv e-prints, p. arXiv:2012.08593
- Peng Y.-j., et al., 2010, , 721, 193
- Peng Y., Maiolino R., Cochrane R., 2015, , 521, 192
- Pillepich A., et al., 2018, , 475, 648
- Pillepich A., et al., 2019, , 490, 3196
- Planck Collaboration et al., 2014, , 566, A54
- Poggianti B. M., et al., 2001, , 562, 689
- Poggianti B. M., et al., 2006, , 642, 188
- Postman M., et al., 2005, , 623, 721
- Roberts I. D., Parker L. C., Brown T., Joshi G. D., Hlavacek-Larrondo J., Wadsley J., 2019, , 873, 42
- Roediger E., Hensler G., 2005, , 433, 875
- Schaller M., Dalla Vecchia C., Schaye J., Bower R. G., Theuns T., Crain R. A., Furlong M., McCarthy I. G., 2015, , 454, 2277
- Schaye J., 2004, , 609, 667
- Schaye J., Dalla Vecchia C., 2008, , 383, 1210
- Schaye J., et al., 2015, , 446, 521
- Simpson C. M., Grand R. J. J., Gómez F. A., Marinacci F., Pakmor R., Springel V., Campbell D. J. R., Frenk C. S., 2018, , 478, 548
- Springel V., 2005, , 364, 1105
- Springel V., White S. D. M., Tormen G., Kauffmann G., 2001, , 328, 726

Springel V., et al., 2018, , 475, 676

Stevens A. R. H., Brown T., 2017, , 471, 447

Taylor P., Federrath C., Kobayashi C., 2017, , 469, 4249

Tremmel M., et al., 2019, , 483, 3336

Vega-Martínez C. A., Gómez F. A., Cora S. A., Hough T., 2021, arXiv e-prints, p. arXiv:2102.00132

Weinmann S. M., Kauffmann G., von der Linden A., De Lucia G., 2010, , 406, 2249

Wetzel A. R., Tinker J. L., Conroy C., 2012, , 424, 232

Wetzel A. R., Tinker J. L., Conroy C., van den Bosch F. C., 2013, , 432, 336

Wetzel A. R., Tollerud E. J., Weisz D. R., 2015, , 808, L27

Wiersma R. P. C., Schaye J., Smith B. D., 2009a, , 393, 99

Wiersma R. P. C., Schaye J., Theuns T., Dalla Vecchia C., Tornatore L., 2009b, , 399, 574

Wright R. J., Lagos C. d. P., Davies L. J. M., Power C., Trayford J. W., Wong O. I., 2019, , 487, 3740

5 Galaxy Quenching in Modified Gravity

Summary

In this Chapter, we present our first results of a project that aims to characterize galaxy evolution in the context of Universes dominated by non-standard gravities. Using the state-of-the-art SHYBONE simulations we study host halo properties, as well as quenched fractions and colour distribution of galaxies residing in models constructed over $f(R)$ and nDGP gravity models. We define two different criteria to select and compare haloes between models, using observable properties. The gas density profiles of groups in modified gravity models are generally denser than their standard gravity counterparts. In general, we show that the selection criteria used to compare haloes in models with different gravities have little impact on the properties of their satellites. Galaxies at $z = 0$ in modified gravity models show higher quenched fractions with respect to the standard model. These differences can be up to $\sim 20\%$ larger than the quenched fractions observed in standard gravity models. Regarding the colour distribution, galaxies in modified gravity models show a more predominant red population with respect to standard gravity, regardless of their host mass. Our results suggest that it is possible to use observable properties of galaxy populations in different environments to place important constraints on something as fundamental as the nature of gravity.

5.1 Introduction

To understand how the Universe evolves, it is necessary to characterize its composition and how its different constituents interact with each other. In this sense, all matter in the Universe is known to gravitationally interact, but a deep understanding of the physical nature of gravity has proven to be a hard task to achieve. The current standard cosmological model (Λ CDM) is constructed over Einstein's General Relativity (GR) as its gravitational model and has as its main constituents the cosmological constant Λ and the cold dark matter, both given the model its name. The Λ CDM model has provided a simple yet very accurate description of the Universe. Many observational pieces of evidence support it. However, even though GR has been empirically confirmed in small scales, the lack of tests at cosmological scales has allowed constraining this model only to a low level of accuracy.

With the arrival of new galaxy surveys such as EUCLID (Laureijs et al., 2011), the Dark Energy Spectroscopic Instrument (DESI; DESI Collaboration et al., 2016) and the Vera C. Rubin Observatory, previously known as the Large Synoptic Spectroscopic Survey (LSST; LSST Science Collaboration et al., 2009), gravity will be testable to an unprecedented level of accuracy at all scales. This will allow astronomers to distinguish between different gravitational models. However, in order to do so, it is necessary to fully understand the impact that different models could have on the distribution of galaxies in the large scale structure, and the imprints that could leave in their properties.

Within this context, hydrodynamical simulations play a key role in connecting theoretical prediction with observational data. In the last decade, hydrodynamical simulations of large cosmological volumes (eg. Vogelsberger et al., 2014; Schaye et al., 2015; Pillepich et al., 2018a; Nelson et al., 2018a), evolved within the standard model, have successfully reproduced observable properties of individuals as well as populations of galaxies. Simulations have also been a widely used tool to study the evolution of galaxies through cosmic time, providing accurate descriptions of some complex phenomena that galaxies experience throughout their history. Nevertheless, the lack of models using non-standard cosmologies hinders the comparison between observations and modified gravity theories. First steps have been given in an effort to study the impact that some of the most studied models of modified gravity could have in the evolution of galaxies (Llinares & Mota, 2014; Hammami et al., 2015; Arnold et al., 2014, 2015, 2016; Ellefsen et al., 2018). However, none of them considers a cosmological volume big enough to make statistically representative studies nor a *'full physics'* model that allows a detailed description of the evolution of baryons within these models. In this sense, the link between the dark and luminous components in Universes governed by modified gravity is still an open question.

This changes with the arrival of the Simulation HYdrodynamics BeyONd Einstein project, SHYBONE. The project introduces the first suite of cosmological simulations with a comprehensive galaxy formation model, evolved with two of the most studied modified gravity models, the Hu & Sawicki $f(R)$ -gravity (Hu & Sawicki, 2007), and the normal Dvali-Gabadadze-Porrati (nDGP) (Dvali et al., 2000) brane model in the Newtonian limit. The simulations count with the same galaxy formation model used for the Illustris-TNG simulation (Pillepich et al., 2018a) and count with several runs, from small high-resolution (25cMpc) to big intermediate-resolution boxes (100cMpc). With these state-of-the-art simulations, it is now possible to study galaxy evolution in a context beyond the classical standard model. Moreover, thanks to the detailed description provided by the galaxy formation model of Illustris-TNG simulations, it is possible to characterize how modified gravity models can affect relevant galaxy properties.

In this Chapter we discuss our efforts to use the SHYBONE simulations to statistically characterize some of the most studied properties of galaxies in a standard model Universe, such as passive fractions and colour distributions, as a function of galaxy stellar mass and environment. We will use

populations of galaxies in different environments to characterize the departures that models based on modified theories of gravity show with respect to the standard model. This effort, which is still part of an ongoing project, represents one of the first attempts to characterize the properties of galaxies in different cosmological contexts based on some of the most promising candidates of modified gravities. Any clear departures between models will be readily tested thanks to available and upcoming large galaxy surveys (eg. Laureijs et al., 2011; LSST Science Collaboration et al., 2009).

The Chapter is organized as follows. In subsection 5.2 we review the galaxy formation model and the properties of the simulations used for this project. Also, we review some of the key aspects of the considered gravitational models. The potential exerted by structures as they evolve varies from one model to another. Thus, it is not possible to provide a one to one comparison between the different simulations. As such, in subsection 5.3 we define the criteria used to compare haloes between different gravitational models. These are based on properties such as the stellar mass of central galaxies and the measured M_{200} of given halo. In section 5.4 we show the differences in the galaxy properties between different models as a function of the environment in which they reside. Finally, in subsection 5.5 we summarize our preliminary findings and discuss the following steps for the project.

5.2 Galaxy formation in alternative Gravities

In this section, we introduce the SHYBONE simulation suite. A series of hydrodynamical cosmological simulations carried out with the hydrodynamical simulation code AREPO (Springel, 2010) and a modified gravity solver, first presented in (Arnold et al., 2019). The simulation suite is currently composed of two series of simulations dedicated to studying two different models of modified gravity. The first suite, first presented in (Arnold et al., 2019), provides models of populations of galaxies evolved in a universe constructed over the $f(R)$ -gravity model (Hu & Sawicki, 2007). A second simulation series was later performed to study a universe evolved over a normal Dvali-Gabadadze-Porrati (nDGP) braneworld model (Dvali et al., 2000). These simulations follow the same methodology presented in Arnold et al. (2019), and are first introduced in Hernández-Aguayo et al. (2021).

In the following section, we discuss the main characteristics of the gravitational models considered, as well as the main characteristics of the simulations themselves. Both simulation suites were performed including the galaxy formation model used in the Illustris-TNG (Springel et al., 2018; Pillepich et al., 2018b; Nelson et al., 2018b; Marinacci et al., 2018; Naiman et al., 2018), following the same subgrid physics prescription.

5.2.1 Modified Gravity Models

5.2.1.1 $F(R)$ -gravity

$f(R)$ -gravity is an extended version of Einstein's General Relativity, which includes an additional scalar degree of freedom (Buchdahl, 1970). This parameter produces a so-called fifth force that yields an enhancement of the gravity in low-density environments by a factor of 4/3. Regions with deep gravitational potential are screened from this force. As a result, the forces experienced within these regions are the same as those expected for GR.

To construct this model, some modifications are applied to the Einstein-Hilbert action S , by adding a function of the Ricci scalar curvature R , $f(R)$, as follows:

$$S = \int d^4x \sqrt{-g} \left[\frac{R + f(R)}{16\pi G} + \mathcal{L}_M \right], \quad (5.1)$$

where g is the determinant of the metric tensor $g_{\mu\nu}$, G is the universal gravitational constant, and \mathcal{L}_M is the Lagrangian of the density field. With this modification, an extra tensor, $\chi_{\mu\nu}$ is added to the Einstein's field equations:

$$\chi_{\mu\nu} = f_R R_{\mu\nu} - \left(\frac{f}{2} - \square f_R \right) g_{\mu\nu} - \nabla_\mu \nabla_\nu f_R. \quad (5.2)$$

This yields to the field equations of $f(R)$ -gravity model to be in the form of:

$$G_{\mu\nu} + \chi_{\mu\nu} = 8\pi G T_{\mu\nu}, \quad (5.3)$$

$$G_{\mu\nu} + f_R R_{\mu\nu} - \left(\frac{f}{2} - \square f_R \right) g_{\mu\nu} - \nabla_\mu \nabla_\nu f_R = 8\pi G T_{\mu\nu}, \quad (5.4)$$

where, $G_{\mu\nu}$, $R_{\mu\nu}$ and $T_{\mu\nu}$ correspond to the Einstein tensor, the Ricci tensor and the stress-energy tensor respectively. ∇_μ correspond to the covariant derivative associated with the metric tensor, and \square correspond to the d'Alembert operator, where $\square \equiv \nabla_\mu \nabla^\mu$. The extra scalar degree of freedom, f_R , corresponds to the derivative of the scalar function $f_R \equiv df(R)/dR$ and mediates with the previously mentioned 'fifth force', an attractive force exerted over massive particles. This force can enhance the gravity by a factor of 4/3 in low-density environments, while in dense environments it behaves like GR-gravity.

In $f(R)$ evolved universes, this fifth force has a significant effect for perturbations in the power spectrum with scales smaller than the Compton wavelength, λ_c ,

$$\lambda_c = a^{-1} \left(3 \frac{df_R}{dR} \right)^{\frac{1}{2}}, \quad (5.5)$$

with a being the scale factor. For distances greater than λ_c the force decays exponentially. This translates into an increased growth rate of cosmological linear density perturbations on scales smaller than λ_c . Regarding the form of f_R , for these simulations, the model of $f(R)$ -gravity proposed by Hu & Sawicki (2007) was chosen. Here $f(R)$ takes the form

$$f(R) = -m^2 \frac{c_1 (-R/m^2)^n}{c_2 (-R/m^2)^n + 1}, \quad (5.6)$$

where $m^2 \equiv 8\pi G \bar{\rho}_{M,0}/3 = H_0^2 \Omega_M$, $\bar{\rho}_{M,0}$ the background matter density at $z = 0$, H_0 the Hubble constant and Ω_M the dimensionless matter density parameter. In this simulation, n is chosen to be $n = 1$. The parameters c_2 and c_3 are selected in such a way that fulfill the gravitational constraints measured in the solar neighborhood (Will, 2014). Also, the model is able to reproduce the late expansion of the Universe, with the appropriate selection of values for the parameters c_1 and c_2 , as shown in Hu & Sawicki (2007)

$$\frac{c_1}{c_2} = 6 \frac{\Omega_\Lambda}{\Omega_m}; \quad (5.7)$$

and

$$\frac{c_2 R}{m^2} \gg 1. \quad (5.8)$$

With these considerations, it is possible to approximate the scalar degree of freedom, f_R , to:

$$f_R \equiv \frac{df(R)}{dR} = -n \frac{c_1 (R/m^2)^{n-1}}{[c_2 (R/m^2)^n + 1]^2} \approx -n \frac{c_1}{c_2} \left(\frac{m^2}{R} \right)^{n+1}. \quad (5.9)$$

Finally, the scalar degree of freedom can be expressed in terms of the background value of the scalar field at $z = 0$, \bar{f}_{R0} . The purpose of this parameter is to set the potential depth threshold in which the screening starts to be effective.

For this work, we only consider two different values of \bar{f}_{R0} , the F6 model, $\bar{f}_{R0} = -10^{-6}$, and the F5 model, $\bar{f}_{R0} = -10^{-5}$. The simulation suite also has available a dark matter only run with an F4 model, $\bar{f}_{R0} = -10^{-4}$. In this sense, the F6 model starts the screening at relatively low gravitational potential depth and is in good agreement with most observational constraints (Terukina et al., 2014). On the other hand, F5 screens regions even with deep gravitational potential, and is in tension with the constraints presented in Will (2014). Nevertheless, even though F5 is ruled out by observational data, the corresponding model provides a useful tool to understand the behaviour of the properties of galaxies, and the Universe, when accounting for this type of gravity.

5.2.1.2 The n-DGP model

The Dvali-Gabadadze-Porrati braneworld model (Dvali et al., 2000), states that matter in the Universe is confined to a 4-dimensional brane embedded in a 5-dimensional bulk spacetime. The model presents a modification to the Einstein-Hilbert action, consisting of two arguments. The first being the classical Einstein-Hilbert action from General Relativity, and the second argument being the extension from the Einstein-Hilbert action to the 5-dimensions of the bulk as follows:

$$S = \int_{brane} d^4x \sqrt{-g} \left(\frac{R}{16\pi G} \right) + \int d^5x \sqrt{-g^{(5)}} \left(\frac{R^{(5)}}{16\pi G^{(5)}} \right) \quad (5.10)$$

where $g^{(5)}$, $R^{(5)}$ and $G^{(5)}$ correspond to the equivalents of the determinant of the metric tensor, the Ricci scalar curvature and the gravitational constant in the space-time bulk.

From here, it is possible to define a characteristic length scale, r_c , at which the behaviour of gravity transitions from the 4-dimensional brane to the 5-dimensional bulk. This scale is called cross-over scale and is defined as follows:

$$r_c = \frac{1}{2} \frac{G^{(5)}}{G}. \quad (5.11)$$

In this sense, at scales larger than the cross-over scale, the second term from equation 5.10 will dominate over the action and the gravity becomes 5 dimensional. The change over the action produces modifications in the Friedmann equation, in the form:

$$\frac{H(a)}{H_0} = \sqrt{\Omega_M a^{-3} + \Omega_{DE}(a) + \Omega_{rc}} - \sqrt{\Omega_{rc}} \quad (5.12)$$

where Ω_{DE} is a dark energy component added to the nDGP model since it is not able to reproduce the late-time acceleration of the universe by itself. The Ω_{DE} parameter was fixed in such a way that $H(a)$ is identical to the values found in a Λ CDM universe. Finally, Ω_{rc} is defined as

$$\Omega_{rc} \equiv \frac{1}{4H_0^2 r_c^2}. \quad (5.13)$$

From these equations, we can see that the greater the value of $H_0 r_c$, the more similar the model becomes to the standard Λ CDM model. In particular for these simulations, values of $H_0 r_c = 5$ and $H_0 r_c = 1$ will be studied. Throughout this thesis, these models are referred to as N5 and N1 respectively. These variations on the gravitational model lead to an enhancement in the gravitational potential of a factor 1.12 for N1 and a factor of 1.04 for N5 at the present day.

Simulation	Hydro model	Cosmologies	$L_{\text{box}} [h^{-1}\text{Mpc}]$	N_{DM}	N_{gas}	$m_{\text{DM}}[h^{-1}\text{M}_{\odot}]$	$\bar{m}_{\text{gas}}[h^{-1}\text{M}_{\odot}]$
Full-physics, L62	TNG-model	ΛCDM , F6, F5	62	512^3	$\approx 512^3$	1.3×10^8	$\approx 3.1 \times 10^7$
Full-physics, L25	TNG-model	ΛCDM , F6, F5	25	512^3	$\approx 512^3$	8.4×10^6	$\approx 2.2 \times 10^6$
Non-rad	Non-radiative	ΛCDM , F6, F5	62	512^3	$\approx 512^3$	1.3×10^8	$\approx 3.6 \times 10^7$
DM-only	-	ΛCDM , F6, F5, F4	62	512^3	-	1.5×10^8	-

Table 5.1: Summary of the properties of the SHYBONE- $f(R)$ simulation suite, presented in Arnold et al. (2019)

Simulation	Cosmologies	$L_{\text{box}} [h^{-1}\text{Mpc}]$	N_{DM}	N_{gas}	$m_{\text{DM}}[h^{-1}\text{M}_{\odot}]$	$\bar{m}_{\text{gas}}[h^{-1}\text{M}_{\odot}]$
Full-physics, L62	ΛCDM , N5, N1	62	512^3	$\approx 512^3$	1.28×10^8	$\approx 2.40 \times 10^7$
Full-physics, L25	ΛCDM , N5, N1	25	2×512^3	$\approx 2 \times 512^3$	8.41×10^6	$\approx 1.57 \times 10^6$
DM-only	ΛCDM , N5, N1	62	512^3	$\approx 512^3$	1.52×10^8	-

Table 5.2: Summary of the properties of the SHYBONE-nDGP simulation suite, presented in Hernández-Aguayo et al. (2021)

5.2.2 SHYBONE Simulations

The SHYBONE simulation is the first suite of cosmological hydrodynamical simulations that simultaneously model galaxy formation, with a complete description of the subgrid physics, within modified gravity models. The first article by Arnold et al. (2019) presented the SHYBONE- $f(R)$, where a model of galaxy formation in a Hu & Sawicki $f(R)$ -gravity universe is introduced. In Hernández-Aguayo et al. (2021) the second series of this suite is introduced, where models of the Universe with an nDGP gravity are studied.

The simulations were performed using the hydrodynamical simulation code AREPO, (Springel, 2010) coupled with the Illustris-TNG galaxy formation model (Pillepich et al., 2018a). To solve the equations of modified gravity presented in the previous section, a modified gravity (MG) module was added to AREPO. The first module, specialized to solve the Hu & Sawicki $f(R)$, was presented in Arnold et al. (2019). The gravity solver for the nDGP model was introduced in Hernández-Aguayo et al. (2021). These modules allow to solve the equations for the scalar field and the Poisson equation in the quasi-static limit and are based in the modified gravity solver presented in the modified-gravity-GADGET code (MG-GADGET, Puchwein et al., 2013). Some modifications were performed to the code, including a more efficient method to solve the nonlinear field equations (Bose et al., 2017) and a local time-stepping scheme presented in Arnold et al. (2016).

The subgrid physics included in the Illustris-TNG galaxy formation model is based on the original Illustris galaxy formation model (Vogelsberger et al., 2014) and includes a set of well-calibrated prescriptions for a series of relevant astrophysical processes needed to reproduce realistic galaxies in cosmological simulations. Within the processes included, in a subgrid fashion, there are prescriptions for black hole growth and AGN feedback, stellar feedback, galactic winds, gas cooling and UV-heating, an algorithm to measure the star formation rate and chemical enrichment. The parameters associated with the prescriptions mentioned above were fitted to reproduce relevant observational constraints. Between them are the galaxy stellar mass function, the gas fraction in galaxies, black hole masses and the cosmic star formation rate density. It should be noted that, for the modified gravity simulations, none of these parameters were changed from the original galaxy formation model (TNG). As shown in Arnold et al. (2019) and Hernández-Aguayo et al. (2021), the departure in the relations found in these simulations with respect to the observational data are smaller than the uncertainties in the observations.

The SHYBONE simulation suite consists of 13 simulations for the Hu & Sawicki $f(R)$ -gravity run and 9 simulations for the nDGP model run, with different cosmologies and resolution levels. A summary of the specifications for each $f(R)$ run is presented in Table 5.1. All simulations were performed within cubic periodic boxes, ten with a box-size length $L_{\text{box}}[h^{-1}\text{Mpc}] = 62$ and three with a box-size length $L_{\text{box}}[h^{-1}\text{Mpc}] = 25$. The ten simulations performed in the large box share the same initial conditions, dark matter particle number ($N_{\text{DM}} = 512^3$) and, for the hydrodynamical simulations, (roughly) the same number of gas cells. The large box subset is comprised of three simulations with the full-physics model for ΛCDM , F6 and F5 cosmology, three simulations with a basic non-radiative hydrodynamic model for ΛCDM , F6 and F5 cosmology and four dark matter only simulations for ΛCDM , F6, F5 and F4 cosmology. Additionally, three simulations in a smaller box are available for the full-physics model. These simulations were performed for the ΛCDM , F6 and F5 cosmology, and have roughly 15 times better resolution than the large-box counterpart.

Regarding the SHYBONE-nDGP simulation run, an overview of their properties is shown in Table 5.2. Each set of ΛCDM , N5 and N1 simulations share the same initial conditions. Six simulations were performed with a box-size length $L_{\text{box}}[h^{-1}\text{Mpc}] = 62$ and three with a box-size length $L_{\text{box}}[h^{-1}\text{Mpc}] = 25$. Three simulations were run with the full-physics model considering a ΛCDM , N5 and N1 cosmology. Additionally, three dark matter only simulations for a ΛCDM , N5 and N1 cosmology were ran. All large-box simulations possess 512^3 resolution elements. Finally high-resolution small boxes were run for ΛCDM , N5 and N1 cosmology. Here, each simulation has 2×512^3 resolution elements, including the full-physics galaxy formation model. All simulations share the same cosmological parameters measured by the Planck mission (Planck Collaboration et al., 2016), with $n_s = 0.9667$; $h \equiv H_0/100 \text{ km s}^{-1}\text{Mpc}^{-1}$; $\Omega_\Lambda = 0.6911$; $\Omega_b = 0.0486$; $\Omega_m = 0.3089$ and $\sigma_8 = 0.8159$, where Ω_m , Ω_Λ and Ω_b correspond to the dark energy, baryonic density and matter density respectively; h is the normalized Hubble parameter; σ_8 is the square root of the linear variance of the matter distribution when smoothed with a top-hat filter of radius $8h^{-1}\text{cMpc}$ and n_s is the scalar power-law index of the power spectrum of primordial adiabatic perturbations.

The main products of the simulations were stored in 46 snapshots between $z = 3$ and $z = 0$ for the $f(R)$ -gravity suite, and 99 snapshots between $z = 20$ and $z = 0$ for the nDGP-model. Based on these snapshots, a two steps procedure was performed to find the bound substructures using the SUBFIND algorithm (Springel et al., 2001) (See Section 2.1). In this work we will analyze the full-physics large box simulations of both suites to study the properties of galaxy populations inhabiting dense environments, considering different cosmologies. Our main goal is to understand the effect that different gravities could have on the transformation from star-forming to quenched galaxies as a function of the environment in which they reside. In particular, we will focus on the intermediate-resolution large box run for the $f(R)$ -gravity (GR, F6 and F5) and nDGP (GR, N5 and N1) runs. We define galaxies as all those subhaloes with an stellar content greater than $M_\star \geq 5 \times 10^9 M_\odot$. As a result, we ensure at least a resolution of 100 baryonic elements per object. For the halo selection, we used the M_{200} given by the FoF algorithm to make the environmental separation and the satellite assignment.

5.3 Comparing haloes from different models

As discussed in the previous section, two haloes with the same mass but in different gravitational models will produce different effective potentials acting over the rest of the structures. In the case of galaxy associations, this could translate into different environmental effects exerted by, e.g., a galaxy cluster to its satellites. As a result, the mass assembly history of these largest structures in the Universe could follow different paths, for both the baryonic and the DM components. Within this context, what we define as a galaxy cluster could differ from one gravitational model to another.

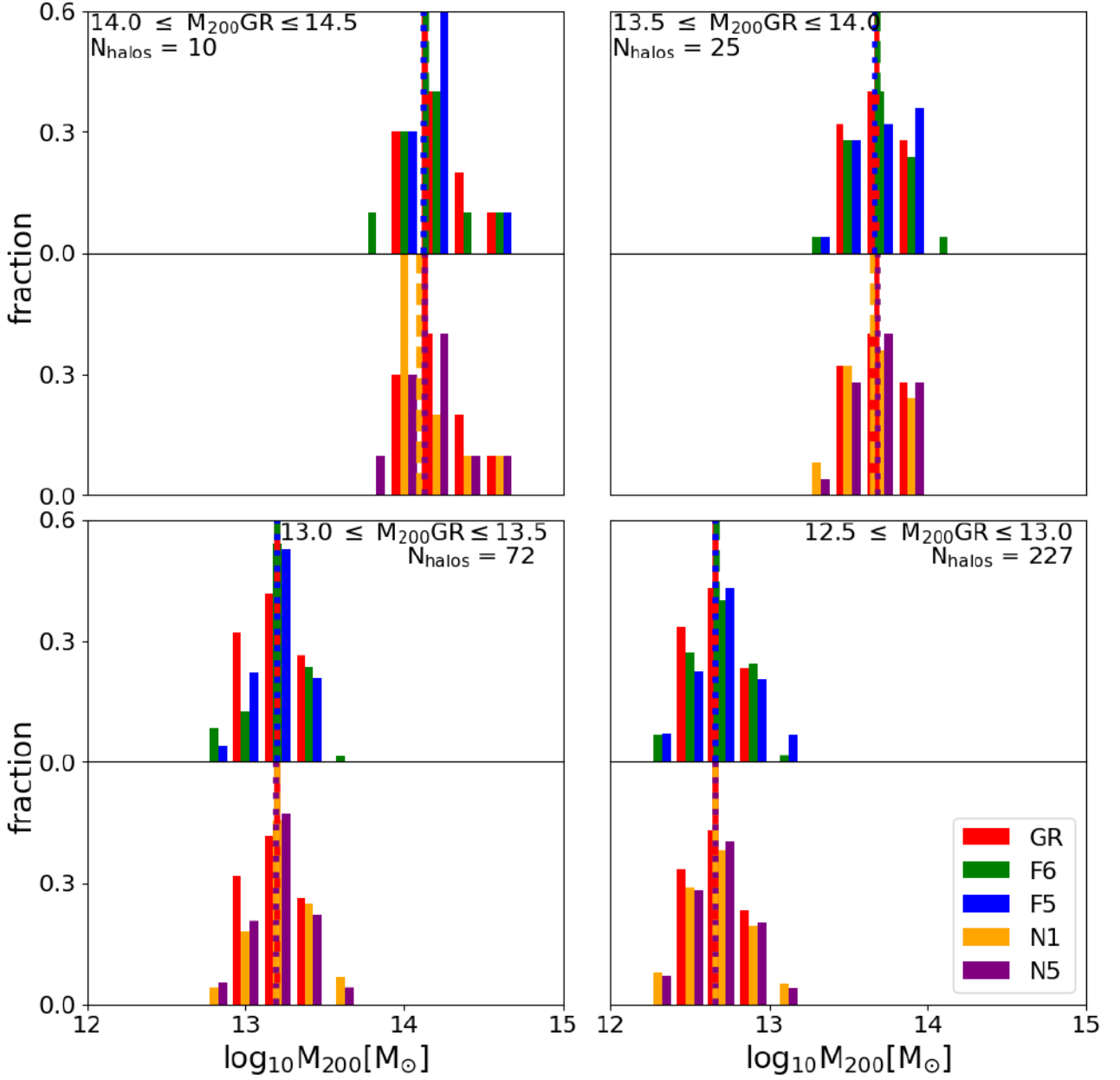


Figure 5.1: Host halo distribution for selected haloes in the MG models, obtain using the M_{200} selection criterion (see text). Red, green, blue, orange and purple bars represent the GR, F6, F5, N1 and N5 distribution, respectively. The corresponding M_{200} mass ranges, as well as the number of selected haloes, are shown on the upper right corner of each panel. Dashed lines correspond to the median M_{200} value obtained from the selected haloes on each model.

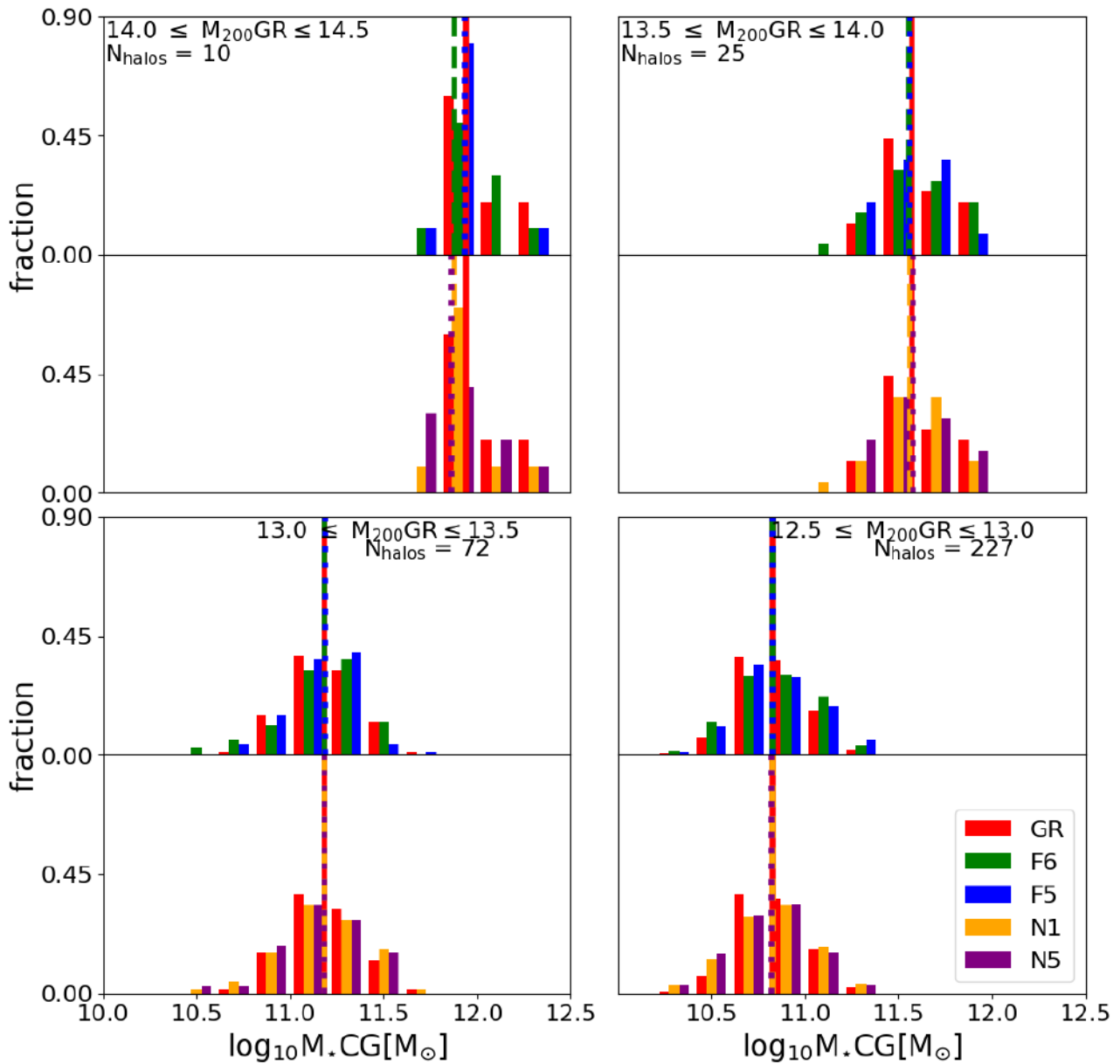


Figure 5.2: As in Figure 5.1, for host halo distributions selected based on the CG M_{*} selection criterion.

To address this potential problem, we used two observationally motivated criteria to compare between haloes in different gravities,

1. To compare clusters based on their M_{200} .
2. To compare cluster based on the stellar mass of the central galaxy (CG) within a certain M_{200} range.

By choosing these observationally measurable properties, we are able to make fair comparisons between models and to characterize differences between their galaxy population. The procedure performed for the selection follows the same steps regardless of the property used to compare. First, we define four halo M_{200} -mass bins in the GR-run to split haloes between galaxy clusters ($\log_{10}M_{200}/M_{\odot} \geq 14$), high-mass groups ($13.5 \geq \log_{10}M_{200}/M_{\odot} \geq 14$), intermediate-mass groups ($13 \geq \log_{10}M_{200}/M_{\odot} \geq 13.5$) and low mass groups ($12.5 \geq \log_{10}M_{200}/M_{\odot} \geq 13$). This sample is defined as the ‘‘control sample’’, and is used as a set of fiducial models. Second, for each MG model, we select sets of candidate haloes for comparison within the M_{200} mass ranges previously discussed. Note that, to make sure sufficient candidates are selected, for the MG models the mass bins are enlarged $\pm 0.3dex$. These candidates are subsequently sorted by mass. Starting from the lowest mass halo on each mass bin, we use a moving window to select a number of objects equal to the number of halos on the GR model. For each of these subsets the median of the desired quantity, i.e. M_{200} or CG M_{\star} , is computed and compared against the corresponding value in the GR simulations. The subset with the closest median in each bin is used for the subsequent analysis.

On Figures 5.1 and 5.2 we show the resulting distributions for selected haloes on each mass bin, using the M_{200} and the CG M_{\star} criteria, respectively. Each box represents a different environment. Boxes are divided into two panels, one for each MG model. The upper and bottom panels show the results for the $f(R)$ -gravity models and the nDGP model, respectively. Red, green, blue, orange and purple bars stand for GR, F6, F5, N1 and N5 models, respectively. From these figures, it can be seen that, although the halo distribution is slightly different between models, the median value remains approximately the same in all mass bins. Small discrepancies in the median can be seen for the galaxy cluster mass bin, but this is expected given the low number of structures in this mass range available in the simulations. Nevertheless, the discrepancies between models median are $< 0.1dex$. A comparison between the samples obtained from both selection criteria shows that the set of MG cluster models, selected based on M_{200} , present broader distributions than the corresponding GR distributions. This is in contrast with the results obtained when selecting models based on the CG M_{\star} , in which the distributions for GR haloes the MG models are similar.

Our goal in this work is to characterize whether different gravity models leave different imprints on the observable properties of satellite galaxies. Thus, it is important to first explore whether the environments where these satellites evolve show different properties. On Figures 5.3 and 5.4 we show the median azimuthally averaged gas density profile from the Intra Group Medium (IGM), $n_{H,IGM}$, for the selected haloes on each model and mass bin. The left and right panels show the gas density distribution for haloes in the $f(R)$ and nDGP gravity models respectively. The shaded area corresponds to 75% percentile for each model. Figure 5.3 focus on the M_{200} halo selection criterion. It is clear that, when using M_{200} to select haloes, GR and F6 shows little to no differences for values of $M_{200} \geq 10^{13}M_{\odot}$. However, the median haloes $n_{H,IGM}$ profiles on the F5 model show significant discrepancies in the inner regions ($r < 0.5r_{200}$), specially for structures with $M_{200}^{GR} \geq 10^{13}M_{\odot}$. For low mass groups, no significant discrepancies between F5, F6 and GR models are observed in the inner regions. However, it can be seen that, at $r \gtrsim 0.2r_{200}$, the F5 and F6 gravity models present a slight

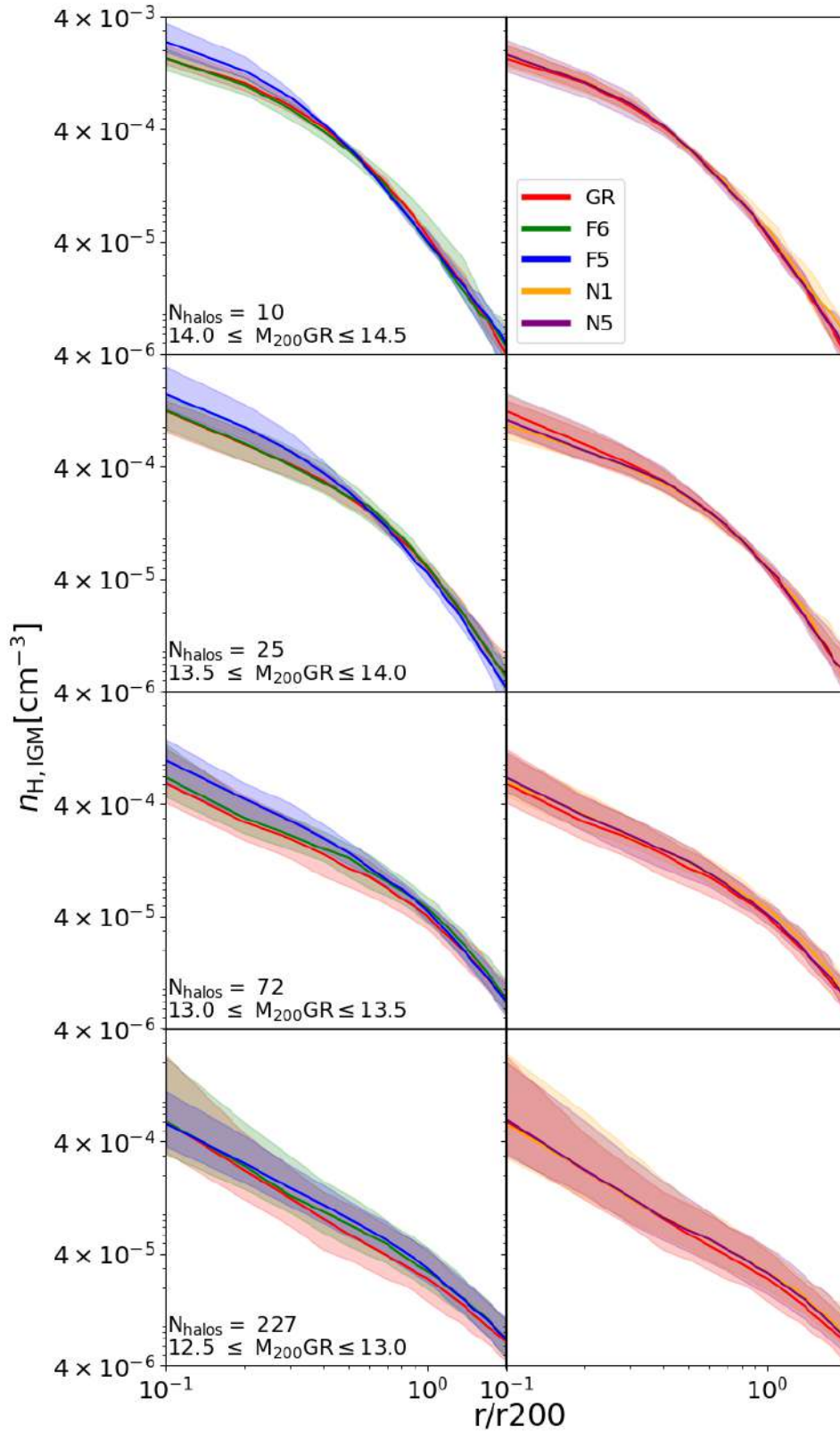


Figure 5.3: Median of all azimuthally averaged gas density profiles for the selected haloes in the $f(R)$ -gravity and nDGP models. Host haloes were selected based on the M_{200} criterion. Red, green and blue lines stand for the GR, F6 and F5 models respectively. The shaded areas indicate the 75 percentile of each distribution. The corresponding M_{200} mass ranges, as well as the number of selected haloes, are shown on the bottom of each panel.

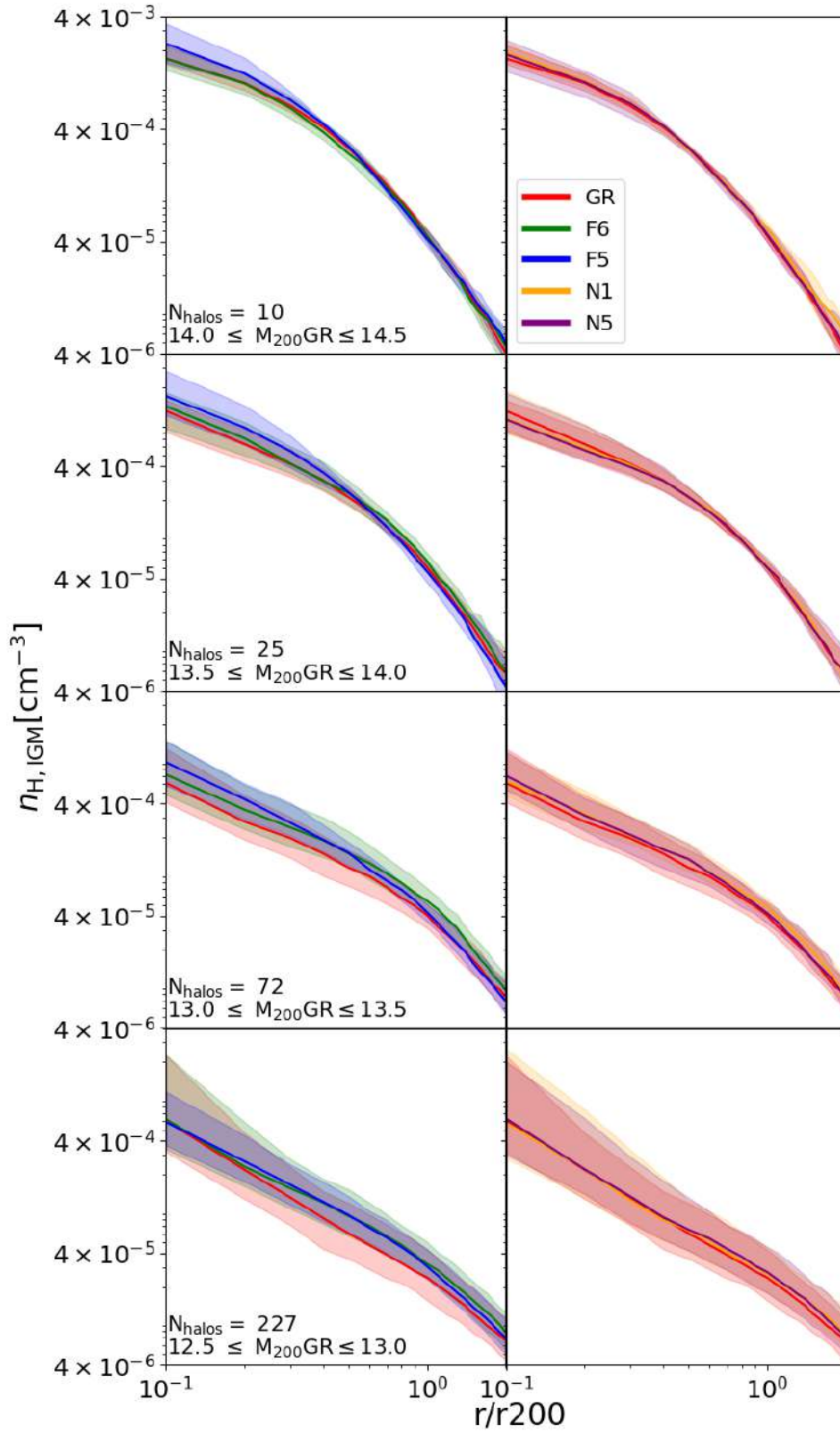


Figure 5.4: As in Figure 5.3, for host halo distributions selected based on the CG M_{\star} selection criterion.

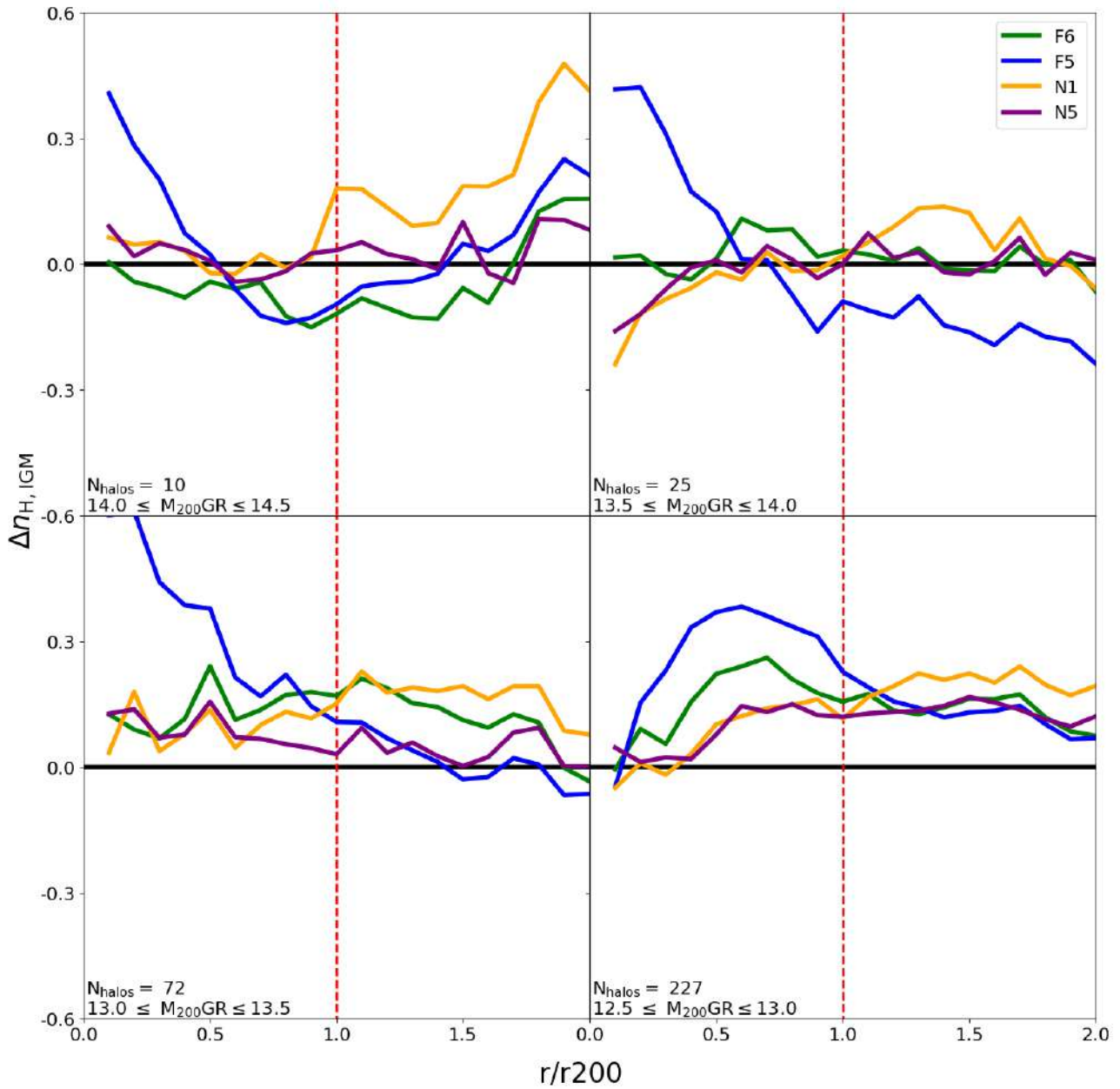


Figure 5.5: Residual gas density profiles for MG haloes with respect to GR, when selecting them by their M_{200} . Positive (negative) values denote an excess (lack) in gas density. The corresponding M_{200} mass ranges, as well as the number of selected haloes, are shown on the bottom of each panel. Red dashed line mark when distance $r = r_{200}$.

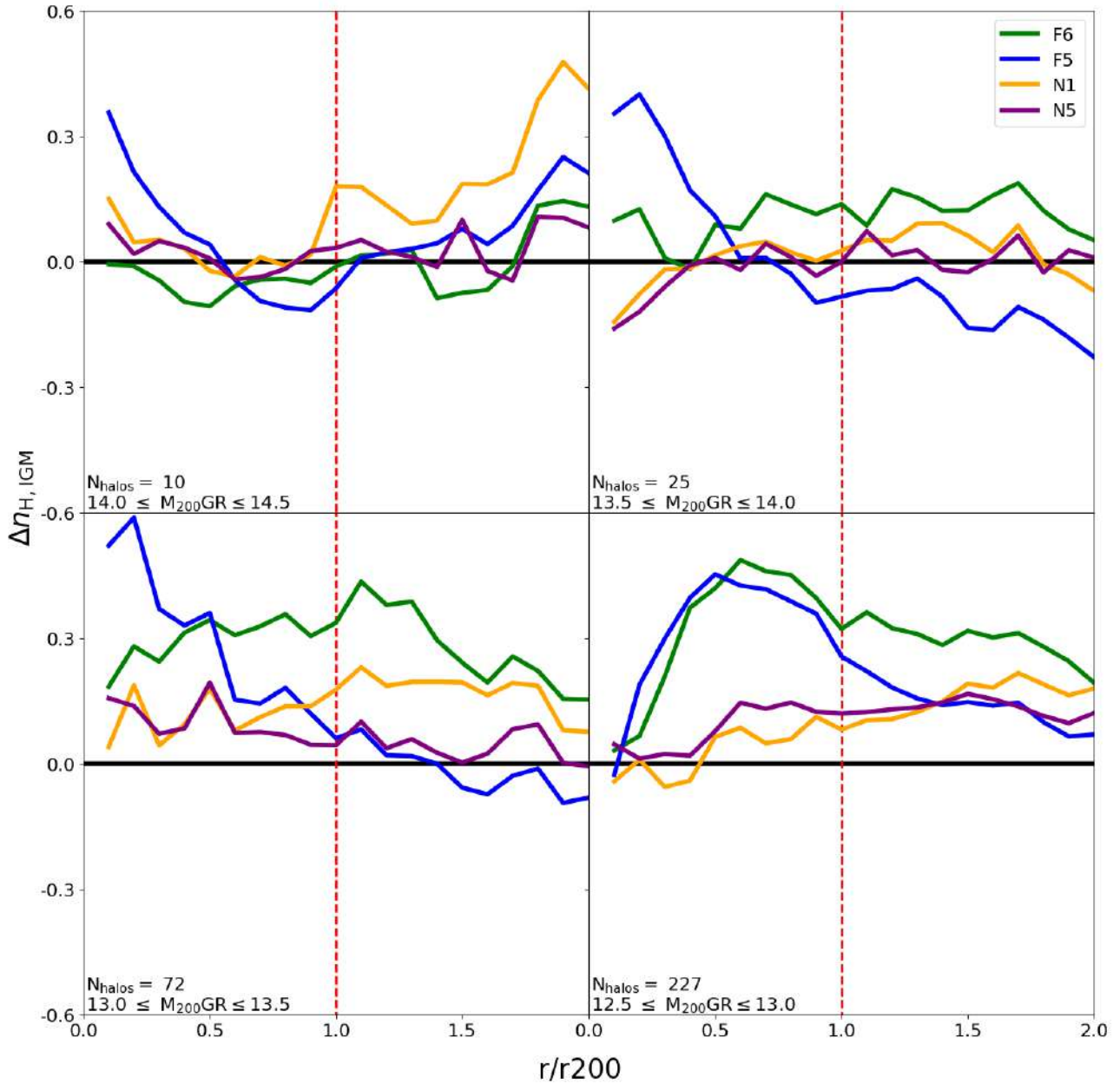


Figure 5.6: As in Figure 5.5, for host halo distributions selected based on the CG M_* selection criterion.

overdensity with respect to GR. Such differences are hardly seen for the nDGP model, where the gas density distribution for both models, in all mass bins, are similar to the distributions obtained in GR. When using the CG M_* as a selection criterion, we find similar results. Discrepancies between the models are more evident for the $f(R)$ model, especially at intermediate masses. In particular, from Figure 5.4 we can see that, while F5 shows differences with respect to GR in all mass bins, for $10^{14} \leq M_{200}^{\text{GR}} \leq 10^{13.5} M_{\odot}$ F6 start to differ from GR and becomes more similar to F5. For $M_{200}^{\text{GR}} \leq 10^{13} M_{\odot}$, F5 and F6 shows very similar behaviour, but both significantly depart from GR. To better visualize the differences between the gas density distributions, in Figures 5.5 and 5.6 we plot residual distributions, i.e.

$$\Delta n_{\text{H,IGM}} = \frac{n_{\text{H,IGM}}^{\text{MG}} - n_{\text{H,IGM}}^{\text{GR}}}{n_{\text{H,IGM}}^{\text{GR}}}. \quad (5.14)$$

Positive (negative) values represent regions with overdense (underdense) regions with respect to GR. The red dashed line indicates a clustercentric distance of $r = r_{200}$. In general, we find that, in low mass haloes (bottom panels) and for $r > 0.3r_{200}$, all MG models are denser than their GR counterparts, regardless of the selection criteria used. For massive groups and clusters, the distribution is much noisier due to the low number of halos. Thus, differences are less clear. As expected, the F5 model is the one that shows the greater discrepancies with respect to GR at any mass bin. Even though the distributions do not significantly change by considering different selection criteria, selecting haloes by their CG M_* leads to slightly denser haloes in all MG models. This is especially clear for the lowest mass haloes in the $f(R)$ -gravity. Regarding the nDGP model, the discrepancies with GR are relatively small compared to $f(R)$ haloes. The strongest differences between these models and GR is seen for the N1 models at the outskirts of galaxy clusters (top left panel).

In these dense environments, the differences shown by the median $n_{\text{H,IGM}}$, obtained in different gravity models, could have an impact on the evolution of their satellite population. In the following section, we will characterize the properties of these galaxy populations.

5.4 Galaxy population on different models

All processes playing a role in galaxy formation and evolution are directly or indirectly linked to gravitational effects. As such, it is interesting to study how galaxies evolve on different cosmological models. This is a topic that, to date, has received little attention. In this section, we characterize some of the key properties that define populations of galaxies, such as passive fractions and colour distributions. Comparisons between models are made by using the selection criteria described in Section 5.3.

5.4.1 Quenched fraction

As we have thoroughly reviewed throughout this Thesis, understanding how galaxies get quenched can provide us important information about their different evolutionary pathway. Within this context, characterizing the fraction of quenched galaxies as a function of their environment can give us a hint about how strongly shaped by the environment galaxies are on different models.

In Figure 5.7 we first show the galaxies quenched fraction, considering all galaxies in the simulations, i.e., independently of the environment in which they reside. Quenched fractions are shown as a function of galaxy stellar mass, M_* . For consistency, we use the same sSFR threshold used in Chapters 3 and 4. Thus, galaxies will be referred to as passive or quenched when they reach an $\text{sSFR} < 10^{-11} \text{yr}^{-1}$. Galaxies in the GR, F6, F5, N1 and N5 models are represented by red, green,

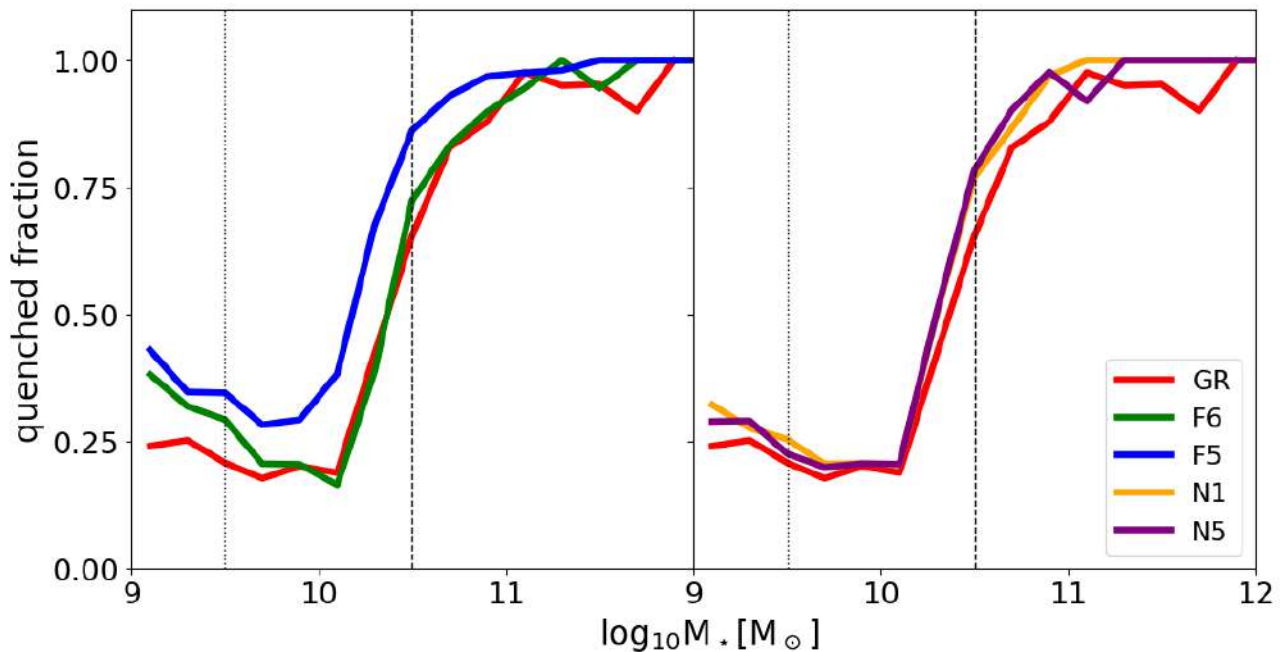


Figure 5.7: Quenched fractions for all galaxies residing in our simulation boxes, independently of the environment where they reside. Black dotted and dashed lines indicate the $m \sim 100$ and ~ 1000 stellar particles resolution thresholds, respectively. The threshold in $sSFR$ used to define galaxies as passive (quenched) is $sSFR < 10^{-11} yr^{-1}$. The left and right panels show the quenched distribution for galaxies in the $f(R)$ and the nDGP model, respectively.

blue, orange and purple lines, respectively. The figure shows that, as expected, for $M_* > 10^{10} M_\odot$, the quenched fractions grows towards higher stellar masses, regardless of the model. However, MG models such as F5, N1 and N6 show larger quenched fractions than GR. In particular, the quenched fractions F5 is $\sim 20\%$ higher than GR at any stellar mass. Conversely, F6 shows a similar quenched fraction distribution to the results found for GR. We note as well the quenched fractions also start to rise for $M_* \lesssim 10^{9.5} M_\odot$. A similar result was already reported by Schaye et al. (2015), although with different simulations. Schaye et al. (2015) shows that, for the EAGLE simulation, the quenched fraction start to rise similarly when galaxies fall below the ~ 100 particles stellar particles resolution limit, likely due to numerical noise effects. Nevertheless, Furlong et al. (2015, 2017) showed that galaxies with > 100 stellar particles reproduce well the stellar to total mass ratio and the evolution of the mass-size relation. The vertical dotted and dashed lines on figure 5.7 indicate the limiting M_* after which galaxies contain more than 100 and 1000 stellar particles, respectively. It should be noted that these are present-day masses and that the number of DM particles per galaxy is typically a couple of order magnitudes greater than their number of stellar particles. In this work, objects with stellar mass resolutions below the one indicated by the dotted lines are discarded from our analysis.

As we are interested in characterizing our results as a function of environment, in Figures 5.8 and 5.9 we show the quenched fractions of galaxies residing within groups and clusters in our five different gravity models. The upper left panel show the quenched fractions for galaxy clusters; the upper right panel is for massive groups, the bottom left shows for intermediate-mass groups and the bottom-right for low mass groups. As before, we find that, regardless of the model and the selection criteria, for $M_* \gtrsim 10^{10} M_\odot$ the quenched fraction grows towards higher stellar masses. In addition, and as expected, we find that this fraction also increases for more massive environments. In Figure 5.8, we

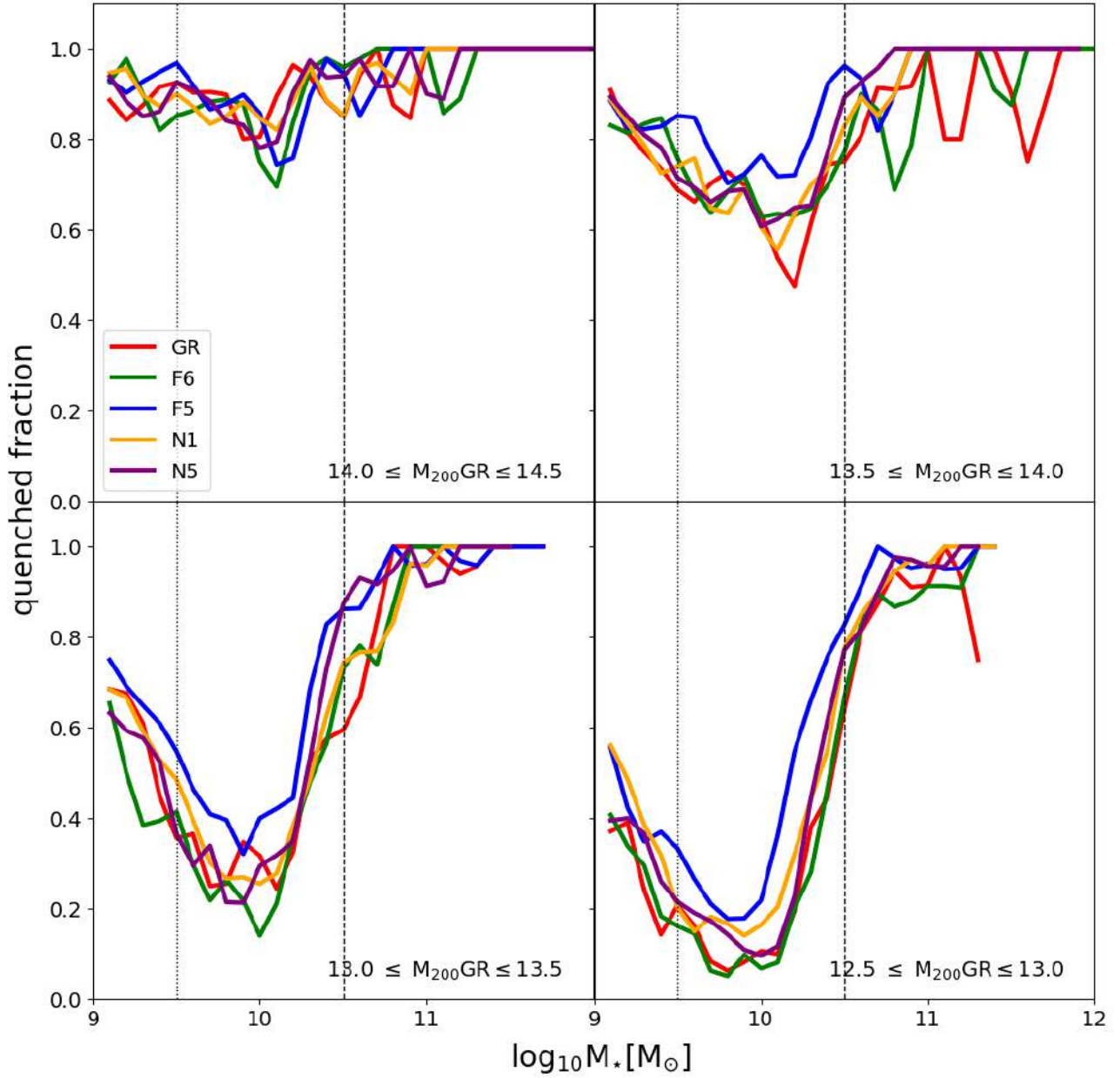


Figure 5.8: Quenched fraction for galaxies as a function of their stellar mass and environments. Host haloes were selected using the M_{200} selection criterion. Black dotted and dashed lines indicate the $m \sim 100$ and ~ 1000 stellar particles resolution thresholds, respectively. The threshold in sSFR used to define galaxies as passive (quenched) is $\text{sSFR} < 10^{-11} \text{yr}^{-1}$. Quenched fractions grow with stellar mass and towards denser environments. Differences between models become more evident at lower host halo masses ($M_{200}^{\text{GR}} < 10^{13.5} M_{\odot}$).

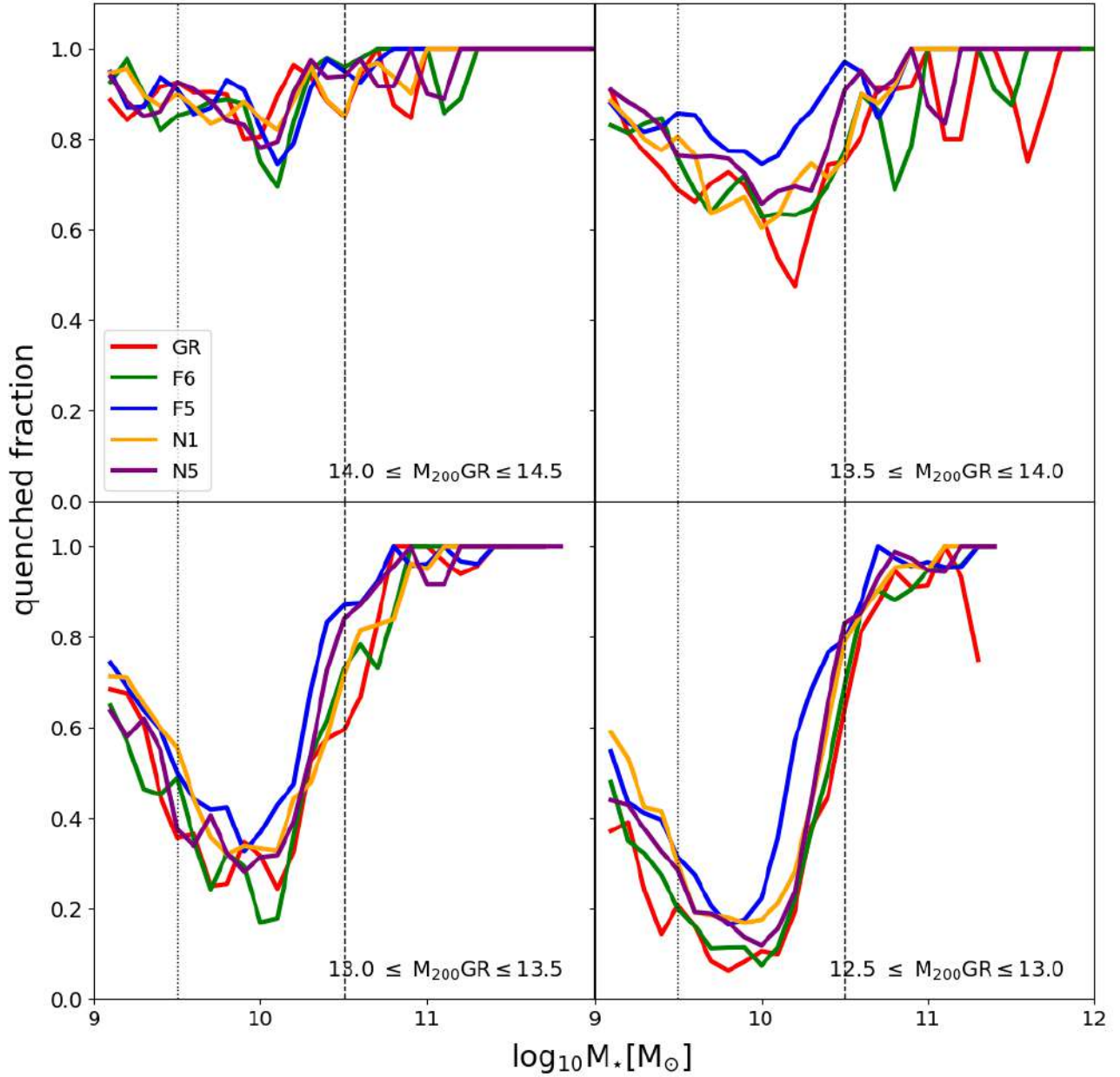


Figure 5.9: As in Figure 5.5, for host halo distributions selected based on the CG M_* selection criterion.

show the results for all our models when host haloes are selected using the M_{200} criterion. Between the 5 models presented, F5 is the one that typically shows the greater quenched fraction at any mass bin. This result is more notorious for the low and intermediate-mass groups (bottom panels). Two important things could be interpreted from this result:

1. Given the enhanced gravity felt by satellites on regions where the fifth force act, environmental effects start to gain relevance at lower halo masses.
2. The enhanced gravity facilitate an early gas consumption. This, for example, could be due to a starburst phase, galaxy mergers or an early AGN activity.

This will be explored in detail once that the merger trees for the galaxies, in all simulations, become available. Differences in the quenched galaxy fraction distributions for the other models N1, N5 are not as clear as in Figure 5.7. Nevertheless, these MG models present a higher quenched fraction than GR for intermediate and low mass groups. This result is less evident for galaxy clusters. This is because, within these more massive galaxy structures, minor differences in the environment are expected to play a less significant role. Recall that, as shown in Chapters 3 and 4 most galaxies are quenched, regardless of their mass, when found within these large clusters. As before, the F6 model shows the most similar distribution to GR.

In Figure 5.9 we show the distributions of quenched galaxy fraction as a function of galaxy mass when environments are selected according to the CG M_* . Contrary to what was found for the host gas density profiles, we find no significant differences when changing the environment selection criteria. The galaxies quenched fractions follow the same trends shown in Figure 5.8, at any host mass bin. As a result, the discrepancies observed in the galaxies quenched fraction can only be associated with the different models, rather than the halo selection. These figures suggest that the criteria used for the host halo selection are more relevant for the structures themselves rather than for the galaxies residing within them, at least for galaxies at $z = 0$.

The main conclusion that can be extracted from these figures is that for models where the gravitational enhancement due to the fifth force at large clustercentric distances, such as N5 and F5, the galaxies quenched fractions are systematically higher with respect to GR. On the other hand, as expected, for models where with gravitational potentials more similar to GR, the overall results in terms of quenched fractions are in much better agreement, regardless of the selection criteria. In the future, we will characterize the evolutionary path followed by galaxies to reach their quenching state in a different model, and how they differ from each other. Our goal will be to study if and how the quenching timescale varies as a function of the gravity model. Having the host's merger trees, we will also be able to study whether the assembly history of the different environments varies with the gravity model and if these differences have an impact on the evolution of their galaxy population.

5.4.2 Colour distribution

As discussed in Section 1.4, the colour of a galaxy reflects its predominant population. Red colours are often associated with galaxies in which an old stellar population dominates, and with little to no star formation. On the other hand, blue galaxies reflect the presence of a significant young population and are usually high star-forming. Within this context, the distribution of galaxies in the Universe has proven to be strongly bimodal (Strateva et al., 2001; Baldry et al., 2006). Interestingly, until now there has been no study exploring how different this distribution could be within Universes evolved under different gravitational models.

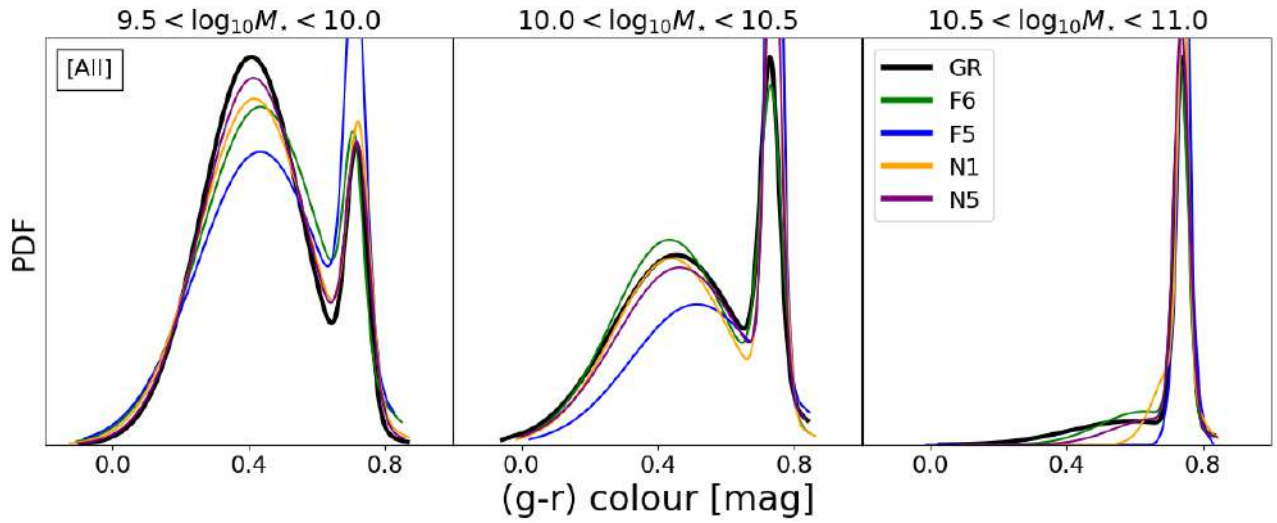


Figure 5.10: Colour distribution for all galaxies residing in our simulation boxes, independently of the environment where they reside. From left to right, the different panels focus on galaxies within different mass ranges. To generate this figure, a double Gaussian distribution was fitted to each galaxy population, as described in the text. Black, green, blue, orange and purple lines represent galaxies belonging to GR, F6, F5, N1 and N5 respectively. Galaxies in MG models show a more predominant red population when compared to GR models. Results are more evident when looking at lower galaxy masses.

In the previous section, we showed that simulated galaxies in models with an enhanced gravity tend to show higher quenched fractions in comparison with the GR model. As a consequence, one would expect that galaxy populations in dense environments for MG models to be redder than in GR. As we go to higher halo masses, where the IGM are dense enough independently of the gravity model, we would expect these discrepancies to vanish. To explore this we follow a procedure similar to what was implemented in Baldry et al. (2004) and further explored in Nelson et al. (2018a), to isolate the red and blue galaxy populations. This is achieved by fitting a double Gaussian distribution to the overall galaxy colour distribution. The following describes the procedure in detail.

1. We select the population of galaxies residing within the desired environment.
2. We split the corresponding galaxies by their stellar mass in three bins 0.5dex wide, ranging from $9.5 < \log_{10} M_{\star} / M_{\odot} < 11$.
3. For each stellar mass bin, we fit a double Gaussian to split between the red and blue galaxy population.
4. Finally, we store the expectation value, maximum and standard deviation of each Gaussian.

As done in Section 5.4.1, we start by exploring the colour distribution of all galaxies in the simulations within the corresponding mass ranges. This is, we consider not just galaxies in the dense environment but galaxies from the field as well. The results are shown on Figure 5.10. Black, green, blue, orange and purple lines represent the colour distribution obtained for GR, F6, F5, N1 and N5 respectively. From left to right, we show the colour distribution of galaxies separated in the three aforementioned stellar mass bins. It is clear that in the MG models galaxies show an overall redder distribution with respect to GR in all mass bins. This is particularly clear for models F5, N1 and N5, but less significant

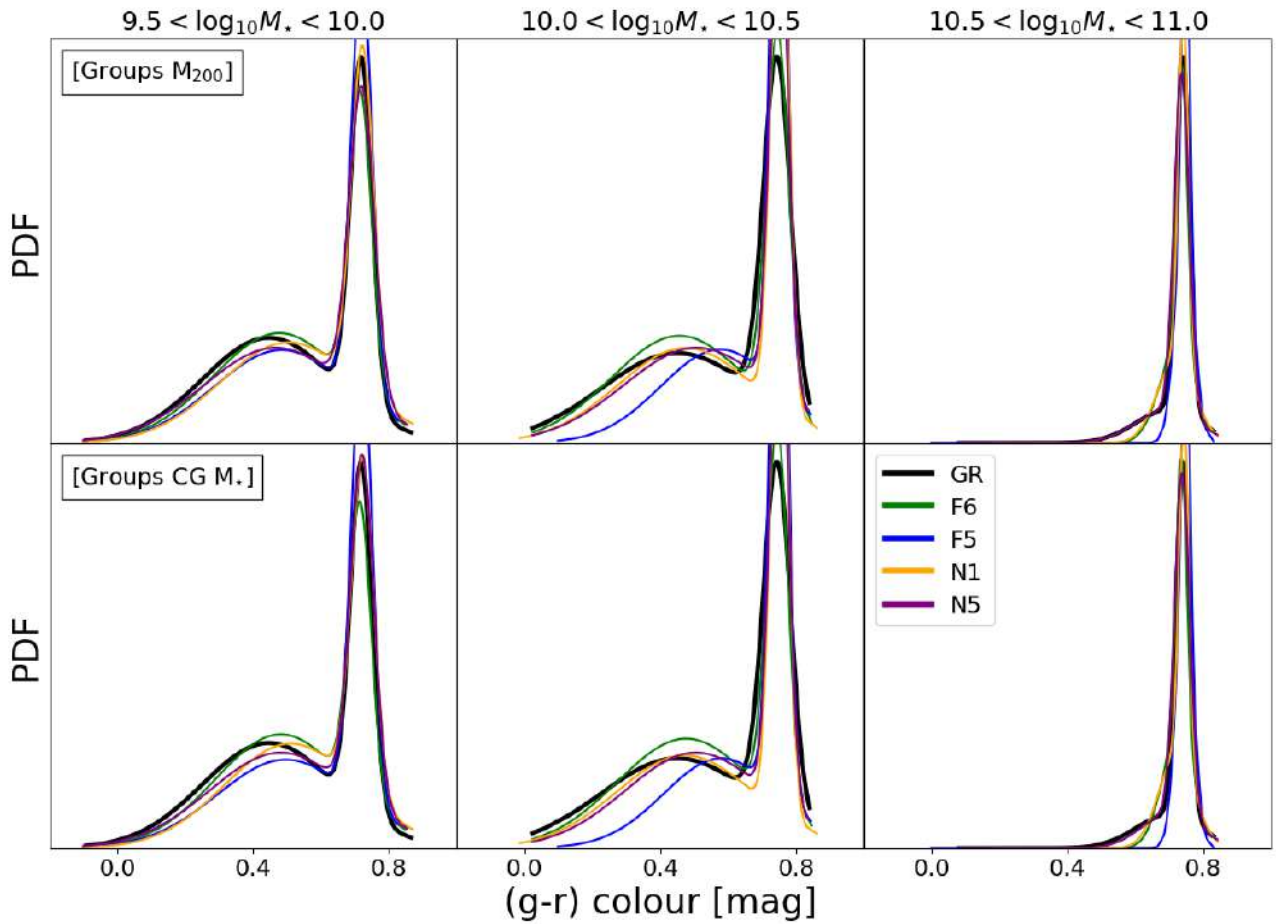


Figure 5.11: The colour distribution of all galaxies that can be found within structures more massive than $M_{200}^{GR} \geq 10^{12.5} [M_{\odot}]$. The top and bottom panels show the results obtained using the M_{200} and the CG M_{\star} selection criteria, respectively. Black, green, blue, orange and purple lines represent galaxies belonging to GR, F6, F5, N1 and N5 respectively. Little to no differences can be seen when using different criteria to select haloes.

for F6. This is consistent with our previous results: i.e. denser IGM and larger quenched fractions for these models.

In Figure 5.11 we show our results, now for galaxies located within dense environments. As before, we select host halos based on their M_{200} and CG M_* . However, to increase the number statistics, we stack all satellites associated with dense environments ($M_{200} > 10^{12.5} M_\odot$) into a single distribution. The top and bottom panels show the results when host halos are selected according to their M_{200} and CG M_* , respectively. In general, and as expected, in these dense environments, the distributions tend to show a more predominant red population with respect to what is shown in Figure 5.10, independently of the gravity model. This is due to the more significant role played by the environment in satellites. As they reach groups and clusters, they rapidly get quenched (see Chapter 4). Because most galaxies in groups and clusters are already quenched, it becomes more difficult to find strong differences between the MG models. A similar result can be seen in Figures 5.8 and 5.9. Nonetheless, the previous tendency towards a more predominant red population in the F5, N1 and N6 with respect to GR is still present and clear. As previously shown, F5 is the model that shows the largest discrepancies with respect to GR. Its overall population, even when looking at low stellar mass galaxies, is significantly more dominated by red galaxies. The bottom panel shows the same results, now for haloes selected according to their CG M_* . The distribution is not affected by our selection criteria, indicating once again that our results are mainly associated with the different MG models.

5.5 Discussion and Future work

In this Chapter we presented the first steps taken towards a comprehensive study to characterize the impact that different gravitational models could have on galaxy evolution. By using state-of-the-art full-physics cosmological hydrodynamical simulations of regions of the universes, constructed with MG models, we have quantified galaxy population key properties as a function of the environment where they reside, such as quenched fractions and colour distributions.

Different MG models could have different impacts on the growth histories of haloes. As a result, it is not possible to select for comparison the same host DM halos in all models. Here we presented two different selection criteria to compare subsets of haloes between simulations. One is based on the host M_{200} and a second is based on the central galaxy stellar mass (CG M_*). Both samples were selected based on median minimization criteria with respect to GR.

When looking at the median density profiles of the Intra Group Medium (IGM) we find that, in general, low- and high-mass groups ($M_{200} < 10^{13} M_\odot$) are typically denser than their GR counterpart, at any distance from their centres. This result suggests that groups and clusters undergo different assembly histories in the different MG models and that this has a significant impact on the $z = 0$ properties of their IGM. These results will be explored in more detail in the following steps of this project. Results based on the different haloes selection criteria show only marginally different results. For example, for the F6 model, when selecting haloes based on their M_{200} , the median gas density profile shows similar behaviour to the one displayed by GR, especially at high and intermediate host masses. However, when selecting haloes by their CG M_* , the median F6 gas density profile shows slightly larger departures from the GR counterpart.

Differences in the IGM properties could have an impact on the populations of galaxies residing within the corresponding environments. Our results also show that, for those models with a more significantly enhanced gravity due to the action of a fifth force, the quenched fractions systematically grow and the galaxy populations become redder in general. Models where the fifth force acts at larger scales (F5 and N5) are the ones that show the greater discrepancies with respect to GR, regardless of the host selection criteria. It is worth recalling that, in Chapter 4, we showed that cluster satellites

reach their quenching state within the first massive group they interact with and that this is due to ram pressure stripping. Thus, the observed differences in IGM density profiles for these MG models are expected to be behind this enhanced quenching process for the satellites.

One of the main goals of this project was to test whether previously known quenching mechanisms on GR affected galaxies MG models with similar efficiencies. To more clearly characterize this effect, it is key to be able to follow the evolutionary history of individual galaxies. Understanding where and when galaxies suffer their transformation from star-forming to passive, their transition from the blue cloud to the red sequence, and the associated time scales will allow us to better constrain the differences between models. Our results will provide important constrain to the observations that will soon become available thanks to big galaxy surveys such as EUCLID (Laureijs et al., 2011), the Legacy Survey of Space and Time (LSST Science Collaboration et al., 2009) and DESI (DESI Collaboration et al., 2016).

Bibliography

- Arnold C., Puchwein E., Springel V., 2014, , 440, 833
- Arnold C., Puchwein E., Springel V., 2015, , 448, 2275
- Arnold C., Springel V., Puchwein E., 2016, , 462, 1530
- Arnold C., Leo M., Li B., 2019, *Nature Astronomy*, 3, 945
- Baldry I. K., Glazebrook K., Brinkmann J., Ivezić Ž., Lupton R. H., Nichol R. C., Szalay A. S., 2004, , 600, 681
- Baldry I. K., Balogh M. L., Bower R. G., Glazebrook K., Nichol R. C., Bamford S. P., Budavari T., 2006, , 373, 469
- Bose S., Li B., Barreira A., He J.-h., Hellwing W. A., Koyama K., Llinares C., Zhao G.-B., 2017, , 2017, 050
- Buchdahl H. A., 1970, , 150, 1
- DESI Collaboration et al., 2016, arXiv e-prints, p. arXiv:1611.00036
- Dvali G., Gabadadze G., Porrati M., 2000, *Physics Letters B*, 485, 208
- Ellewsen T. A. S., Falck B., Mota D. F., 2018, , 615, A134
- Furlong M., et al., 2015, , 450, 4486
- Furlong M., et al., 2017, , 465, 722
- Hammami A., Llinares C., Mota D. F., Winther H. A., 2015, , 449, 3635
- Hernández-Aguayo C., Arnold C., Li B., Baugh C. M., 2021, , 503, 3867
- Hu W., Sawicki I., 2007, , 76, 064004
- LSST Science Collaboration et al., 2009, arXiv e-prints, p. arXiv:0912.0201
- Laureijs R., et al., 2011, arXiv e-prints, p. arXiv:1110.3193
- Llinares C., Mota D. F., 2014, , 89, 084023
- Marinacci F., et al., 2018, , 480, 5113
- Naiman J. P., et al., 2018, , 477, 1206
- Nelson D., et al., 2018a, , 475, 624
- Nelson D., et al., 2018b, , 475, 624
- Pillepich A., et al., 2018a, , 473, 4077
- Pillepich A., et al., 2018b, , 475, 648

Planck Collaboration et al., 2016, , 594, A13

Puchwein E., Baldi M., Springel V., 2013, , 436, 348

Schaye J., et al., 2015, , 446, 521

Springel V., 2010, , 401, 791

Springel V., White S. D. M., Tormen G., Kauffmann G., 2001, , 328, 726

Springel V., et al., 2018, , 475, 676

Strateva I., et al., 2001, , 122, 1861

Terukina A., Lombriser L., Yamamoto K., Bacon D., Koyama K., Nichol R. C., 2014, , 2014, 013

Vogelsberger M., et al., 2014, , 444, 1518

Will C. M., 2014, Living Reviews in Relativity, 17, 4

6 Summary and Conclusions

Galaxy formation and evolution has been a deeply studied topic since the discovery of the first extragalactic sources by Hubble (1926). Galaxies in the Universe can present a wide variety of general properties, exhibiting different morphologies, sizes, masses and colours, among others. They are also found undergoing different processes that play a key role in their subsequent evolution. The development of self-consistent models describing how galaxies form and evolve to reach their present-day distribution and configurations has been extremely challenging. This required the development of a detailed framework that could allow the description of the growth of structure in the Universe, as well as the characterization that the environment has in galaxy evolution. Galaxy clusters, in their condition of most bound virialized structures of the Universe, are an ideal laboratory to study galaxy transformations but, until recently, limited information about these structures was available.

In the last decades, the amount of available astronomical data have exponentially grown. Galaxy surveys such as the Sloan Digital Sky Survey (SDSS; York et al., 2000), have pushed our previous empirical knowledge about galaxy evolution to the limits, and have allowed astronomers to test theories and models. In the upcoming years, the amount of information is only expected to keep growing. The observable Universe will be studied with unprecedented accuracy, at different wavelengths, with deeper observations than ever, thanks to the arrival of new galaxy surveys such as the Legacy Survey of Space and Time (LSST; LSST Science Collaboration et al., 2009), Euclid (Laureijs et al., 2011), the Dark Energy Survey (DES; DES Collaboration et al., 2021) and eROSITA (Predehl et al., 2021). Alongside, the level of sophistication behind galaxy formation models has also greatly improved during the last decades. Hydrodynamical simulations are now able to simulate relatively large volumes of the Universe including, self-consistently, detailed algorithms to model complex baryonic physic processes. New simulations, such as EAGLE (Schaye et al., 2015) and Illustris-TNG (Nelson et al., 2018), have revolutionized the studies of galaxy formation and evolution. From isolated galaxies to massive galaxy clusters, there is now available a great numerical database to study the formation and evolution of galaxies in all kinds of environments.

Even with all these advances, several critical question remain to be answered in the field of galaxy formation and evolution and, in particular, regarding the role played by the environment. To further develop a proper understanding about the most critical processes driving galaxy evolution, observations and simulation must work together. In particular, for this Thesis, we have analyzed fully cosmological hydrodynamical simulations to shed light on an still open subject; what is the path followed by cluster satellite galaxies to cease their star formation activity? To fulfil our objective, we targeted specific questions such as how, when and where galaxies get quenched.

With this in mind, in Chapter 3 we focused our efforts on addressing “where” cluster satellite galaxies get quenched. To this end, we traced back in time the star formation history of every satellite galaxy located within the simulated galaxy clusters from the EAGLE project. We used two different criteria to characterize the moments when a galaxy star formation activity suffered significant changes. The first based on the moment when galaxies show the greatest drop in their star formation activity between two consecutive snapshots (strongest drop in SFR). A second based on the time when galaxies fully cease their star formation (quenching). Our results show that galaxies suffer strong decrements in their star formation prior their infall into galaxy clusters. This process take place within haloes with a broad range in mass, and does not show a clear environmental dependence. The main role of this process in galaxy evolution is to slow down the rapid growth in stellar mass that galaxies typically show until this point. Nevertheless, even after the strongest drop, galaxies keep forming stars but a significantly lower pace.

On the other hand, we find that, in our models, galaxies fully cease their star formation activity

typically once that they reach a dense enough environment, such as those present in massive galaxy groups or galaxy clusters. As reported in previous observational works (Gavazzi et al., 2006; Faber et al., 2007; Peng et al., 2010; Wetzel et al., 2013; Jaffé et al., 2015, eg), the quenched fraction of galaxies in clusters grows with cluster mass, and many of the passive population that we observe in clusters nowadays came as "pre-quenched" objects. The term pre-quenched is often used in the literature to refer to those galaxies that stopped their star formation prior their accretion into the cluster they currently inhabit. In this Thesis we showed that low mass clusters have a small fraction of pre-quenched galaxies, and our results indicates that the importance of pre-quenching grows with cluster mass. This is due to the hierarchical growth of these massive environments; more massive clusters tend to accrete more massive substructures. And, as previously discussed, this more massive accreted objects arrive to their cluster with higher fraction of quenched galaxies. Unfortunately, given the limited box sizes of the available simulations, we were not able to extend the observed pre-quenched galaxy fraction trend for clusters more massive than $5 \times 10^{14} [M_{\odot}]$. A plausible solution for this caveat was to consider another set of simulations, ran with the same subgrid model and resolution but with a sample of galaxy clusters including objects as massive as $2.5 \times 10^{15} [M_{\odot}]$

Within this context, in Chapter 4 we focused in answering "how" and "when" galaxies get quenched. By using the simulations of the CLUSTER-EAGLE project, a set of zoom-in simulations of 30 galaxy clusters ranging from $14 < \log_{10} M_{200} / M_{\odot} < 15$, we investigated which process is the main culprit behind the quenching of the star formation in these numerical models. Regarding the importance of pre-quenching for galaxy clusters, we confirmed that the pre-quenched fraction of satellites grows towards higher cluster masses, reaching an $\sim 80\%$ of pre-quenched galaxy populations for haloes with $M_{200} > 10^{15} [M_{\odot}]$. An interesting result is that, contrary to what was expected, we showed that the most massive clusters play little or no role in ceasing the star formation of their satellites. Even though these massive structures posses ideal conditions to cease their star formation activity, their current satellite population is mainly the result of the accretion of already passive galaxies.

When studying clusters at higher redshift we found that the satellite pre-quenched fraction decreases at any halo mass. For example, galaxy clusters with $M_{200} \sim 4 \times 10^{14} [M_{\odot}]$ at $z = 0$ posses $\sim 40\%$ more pre-quenched galaxies than their counterpart at $z = 0.9$. This result is a direct consequence of the different assembly histories undergone by clusters at different redshifts (McGee et al., 2009). Galaxies at high z typically have not had time to inhabit another massive halo previous to the infall into a massive structure. As a result, the vast majority of satellites observed in high mass structures at high z get quenched within the same halo. This result leads to the following interesting conclusion. If we are interested in galaxies undergoing environmental effects, detailed observations of low mass or high redshift clusters are desired, given that their satellites are currently undergoing their quenching process. On the other hand, if we want to study pre-quenched or pre-processed galaxies, we need to observe at low redshift massive clusters since the majority of their satellites correspond to this type of galaxies.

Regardless of the redshift and the mass of the clusters, our result showed that the main culprit behind the quenching of the satellite's star formation is ram pressure stripping. This result shows that, even though mass quenching mechanisms can play a role in decreasing the star formation of galaxies (see Chapter 3), they are not main mechanism behind the high quenched fractions observed inside galaxy clusters. Moreover, contrary to what was suggested by several authors (eg. Miller, 1986; Moore et al., 1996, 1999; Boselli & Gavazzi, 2006), out of many mechanisms acting inside galaxy clusters, ram pressure stripping stands as the main culprit behind satellite quenching. Nevertheless, it should be mentioned that last observational works, points towards the same result found within this work, that ram pressure stripping is the main culprit behind satellite quenching (eg. Jaffé et al., 2015, 2018; Roberts et al., 2019; Cortese et al., 2021)

We also found that this ram pressure stripping becomes efficient in environment with local density $\rho_{\text{ICM}} \gtrsim 10^{28.3} \text{ gr cm}^{-3}$. This threshold is typically reached at the outskirts of low mass clusters ($r \sim r_{200}$). Briefly after their accretion into these dense structure ($\sim 1\text{Gyr}$), galaxies get their gas reservoir stripped, thus ceasing their star formation activity. Interestingly, this result was already reported by Roberts et al. (2019). Using combined data from SDSS and Chandra, they found a rise in the quenched fraction for low mass galaxies ($M_{\star}/[M_{\odot}] < 10^{9.9}$) when the density of the local environment reached this threshold. The analysis of fully cosmological hydrodynamical simulations allow us to developed physical interpretation of the density threshold observed by Roberts et al. (2019). Once galaxies reach this particular threshold, ram pressure stripping becomes very efficient and galaxies enter a phase of ‘rapid-quenching’. These results highlights the advantages and the importance of simulations and observations working together.

Finally, in Chapter 5, we presented the first results of an effort that aims at characterizing galaxy evolution in the context of universes dominated by non-standard gravities. Our analysis was based on the first suite of fully cosmological hydrodynamical simulations, evolved in modified gravities (MG), including a “full-physics” model of galaxy formation. Our first goal was to characterize observable differences in the main properties of galaxy populations between different gravitational models. The simulations includes two of the most studied gravitational model, being them the $f(R)$ -gravity model introduced by Hu & Sawicki (2007) and the nDGP model introduced in Dvali et al. (2000). Structures in our simulations were subdivided according to different environments, i.e., galaxy clusters, high mass groups, intermediate mass groups and low mass groups. To compare haloes between MG models, we use properties that can be observationally estimated, such as their M_{200} and the stellar mass of the central galaxy. Our results show that massive groups and cluster on the F5 MG model tend to be more concentrated than their GR counterpart. On the other hand, for $f(R)$ models, intermediate and low mass groups tend to be denser than their GR counterpart at nearly all radii. This discrepancies can be as high as 60% for the most extreme cases. When selecting haloes by the CG M_{\star} , intermediate and low mass groups, show the most pronounced discrepancies with respect to GR. As we were interested in characterizing discrepancies between MG models and GR, our first goal was to explore whether discrepancies between the overall galaxy distribution were present, regardless of the environment in which they reside. Quenched fractions and colour distribution are two key properties in the context of galaxy evolution, as they give us insight about the evolutionary path followed by galaxies and the impact that environmental effects had on them throughout their history. Regarding their star formation activity, we found that galaxies MG models show show higher fractions of quenched galaxies at any stellar mass, reaching to values that are $\sim 20\%$ higher than GR in the most extreme case (F5). When splitting our sample by environment, we showed that this result remains for intermediate and low mass groups, but it gets diluted when looking at the most massive structures. As discussed above, when galaxies reach environments that are dense enough, they rapidly get quenched, so little differences between massive cluster in different MG models is found. Nonetheless, regardless the gravity model, the quenched satellite fraction in massive clusters reaches values between $70 \leq q_f \leq 100\%$ at any stellar mass.

On the other hand, when looking at the colour distribution of all the galaxies in our models we find that galaxy populations in MG model show a more predominant red population in comparison to GR. This result is more clear when looking at the intermediate and low stellar mass galaxy population ($9.5 < \log_{10}(M_{\star}/[M_{\odot}]) < 10.5$). Within this mass range, discrepancies between models are stronger, with the F5 model as the one showing the greatest discrepancies with respect to GR. When looking at galaxy groups, discrepancies in the colour distribution between models become less clear. As galaxies in groups are often found in quenched state, regardless the model, colour distribution are widely dominated by a red population. This result suggest that discrepancies based on color distributions

should be more evident when looking at the star forming population of different models. In the future, we will explore whether these discrepancies are still present at higher redshift, and will characterize the origin of the enhanced quenched fractions for the MG models. Our preliminary conclusion is that, even though the different MG models show discrepancies with respect to GR in dense environments, the most striking differences in galaxy population properties can be found in galaxies residing in low density environments such as the field or low mass groups.

6.1 Future Work

The results presented on this Thesis set the path for further development on several topics. In the near future we plan to address some of the questions that remained open. In what follows we describe some of these open questions:

- When galaxies transition from star forming to quenched, other properties besides their star formation are affected as well. For example, their morphology can also be affected by this transition. Depending on the galaxy's global properties at the quenching time, they could switch from spirals to lenticular or even more drastic transformation towards an elliptical morphology. This transitioning of their star formation activity also has an impact on the galaxies mean colour. While in Chapter 4 we were able to characterize the quenching timescale and the main process behind it, we did not review the timescale within which this morphological transformation acts. Similarly, we did not characterize the timescale associated to the satellites transition from the blue region to the red sequence of the galaxies colour magnitude diagram. In the future, we will address these open questions by analyzing and comparing different suites of hydrodynamical simulations with different subgrid models. Due to the relatively short timescales involved, we will particularly focus on those models with high temporal resolution.
- Another interesting aspect to explore aims at defining a selection criteria, based global galaxy properties, to observationally select "pre-quenched" galaxies. With the arrival of the big databases provided by new galaxy surveys, such as LSST, a pre-defined criteria based on observationally measurable properties is key. Properties such as galaxy morphology, colour, metallicity, kinematics and position in the phase-space, or a combination of these properties, can tell us which galaxies are currently undergoing stripping inside a given cluster, and which were accreted by the clusters as pre-quenched objects.
- The level of sophistication reached by numerical models during the last decades is remarkable. We currently count with several different simulation suites, sampling different volumes of the universe, with different implementations of most relevant baryonic processes. This allow us to self consistently track the evolution of the different galactic baryonic components at different scales. However, high mass and time resolution simulations of low mass galaxy cluster and groups are still scarce. As shown in Chapter 4, these structures posses the highest fractions of in-situ quenched galaxies and thus are particularly relevant for studies based on environmental quenching. We are currently designing a new suite of high resolution and high temporal cadence zoom-in simulations of low mass galaxy clusters that will allow to study in detail the quenching process as satellites penetrate into the densest regions of the clusters ICM. With these simulations we will also to characterize the delayed quenching phase, wich begins to affect galaxies previous to their accretion into the clusters.

Bibliography

Boselli A., Gavazzi G., 2006, , 118, 517

Cortese L., Catinella B., Smith R., 2021, , 38, e035

DES Collaboration et al., 2021, arXiv e-prints, p. arXiv:2105.13549

Dvali G., Gabadadze G., Porrati M., 2000, Physics Letters B, 485, 208

Faber S. M., et al., 2007, , 665, 265

Gavazzi G., O'Neil K., Boselli A., van Driel W., 2006, , 449, 929

Hu W., Sawicki I., 2007, , 76, 064004

Hubble E. P., 1926, , 64, 321

Jaffé Y. L., Smith R., Candlish G. N., Poggianti B. M., Sheen Y.-K., Verheijen M. A. W., 2015, , 448, 1715

Jaffé Y. L., et al., 2018, , 476, 4753

LSST Science Collaboration et al., 2009, arXiv e-prints, p. arXiv:0912.0201

Laureijs R., et al., 2011, arXiv e-prints, p. arXiv:1110.3193

McGee S. L., Balogh M. L., Bower R. G., Font A. S., McCarthy I. G., 2009, , 400, 937

Miller R. H., 1986, , 167, 41

Moore B., Katz N., Lake G., Dressler A., Oemler A., 1996, , 379, 613

Moore B., Lake G., Quinn T., Stadel J., 1999, , 304, 465

Nelson D., et al., 2018, , 475, 624

Peng Y.-j., et al., 2010, , 721, 193

Predehl P., et al., 2021, , 647, A1

Roberts I. D., Parker L. C., Brown T., Joshi G. D., Hlavacek-Larrondo J., Wadsley J., 2019, , 873, 42

Schaye J., et al., 2015, , 446, 521

Wetzel A. R., Tinker J. L., Conroy C., van den Bosch F. C., 2013, , 432, 336

York D. G., et al., 2000, , 120, 1579

Acknowledgments

I want to start by thanking my supervisor, Facundo Gómez, whose encouragement, patience, and unconditional support, allowed me to grow as a scientist and as a person. Facu, I know that things don't always go as planned, but every time that I went astray, you helped me get back on track. For trusting in me as a scientist, for letting me run my imagination when we were working, and for asking me what I wanted to do at each step. I'm really lucky to have you as my supervisor, as my friend and as a colleague. I hope that we can still work together for a long long time!

I want to thank Sergio Torres for believing in me since my Bachelor's. Sergio, you were the one that convinced me to make this PhD and I'm extremely grateful for that. You introduced me to Facundo at the beginning and you introduced me to Nelson during my Bachelor's. Without you, this never would have been possible, and honestly, I'm not sure where I would be today. Maybe in engineering, maybe studying music, who knows.

I want to thank Nelson Padilla for his encouragement to work with hydrodynamical simulations since my Bachelor's. Nelson, you taught me the wonders (and the pain) of working with simulations, and once I started I just couldn't stop. Thanks for teaching me that "the imagination is the limit" and to plot everything, nobody knows when something interesting will pop off!

I'm deeply thankful to my professors at the University, Rodolfo Barbá, Julia Arias, Alexandre Roman, Antonela Monachesi, and Hector Cuevas, for their understanding when the times were difficult, and the opportunities that they gave me to learn and fall in love with Astronomy. For always keeping an open door to ask any questions that I had and for the interest shown for me to learn.

I want to thank the Thesis committee, Yara Jaffé, Nelson Padilla, Sergio Torres-Flores and Patricia Tissera for being part of this Thesis. Thanks for all your insightful comments that greatly improved the quality of this manuscript and all the scientific feedback, which will greatly improve my future research. Also, I'm deeply grateful to the Doctoral Advisory Committee, Hector Cuevas and Sergio Torres-Flores, for their comments and suggestions during the development of this Thesis. For always keep an eye on me and the insightful discussions during these 4 years.

I'm deeply grateful to the friends that I made during this process. I'm really grateful to my office mates for the endless music playlists and for allowing me to always have the desktop by the window (I'm not sure if you understand how grateful I am for that). For the coffees in the morning (and afternoon), for the talks in the halls of the University and for all those times that we got a beer after work.

I want to thank the group of formation and evolution of galaxies of the University (FORMEVOL) for the insightful discussions that we had every week. For all the feedback that you gave me during these years, for the interesting questions that were born in each one of the meetings, for the coffees shared at the cafeterias near the University, and for the collaborations that will come!

To my friends in life, for putting up with me all this time. I know that it was not easy and that more than once I was as obnoxious as can be. Jonny, Tomás, Chony, Andrux, Alex, Pablito, Sebi, Vivi, Cami, thank you for not giving up on me, for your friendship during all these years, for your advice when things did not look good, for hearing when I needed to talk, for endless conversations, for the music shared and for always putting a smile on my face. Every time that I needed you, you were there, and for that, I'm as grateful as I can be. You know what they say if a friend lasts more than 7 years, they are for life.

I want to especially thank Daniel (flaco) and Nahir (flaca). You guys are amazing, I don't know what are the odds that my two best friends ended up getting married, but I guess that amazing people attract each other. Even though you two are far away from me right now, I'm always carrying you by my heart. I know that you two will accomplish whatever you want to do, and I hope that in the future we

get to live in the same city again. I miss you guys so much but keep fulfilling your dreams.

To my parents Susana and Carlos, for teaching me what to do and what not to do. For teaching me to be a good person above all, for their unconditional support despite all my bad choices. For always hearing me when I wanted to say something for being friends besides my parents. Viejito, thank you for teaching me the importance of friends in life. I can confidently say that my friends are amazing, and if I got to meet them was thanks to you. For teaching me that things do not always go as planned, but to keep a smile on my face and keep trying. Madre linda, you always put me and my siblings above anything else, even you. I always have admired how hard you worked for us. I just want to be able to pay back what you did for us, even if it is just a fraction of all that you did. You are the strongest woman I've ever met, and I will be forever grateful for all your love and support. Thank you for being my mother and for teaching me what is love.

To my siblings, Maxi and Darla, for being my most precious treasure. I cannot imagine how life would be without you. Enana, you are another extraordinary woman in my life. Like my mom, you are one of the strongest people that I ever met. Keep fighting for your dreams, keep fighting for what you believe. Keep teaching me how to have an open mind and keep being as consequent as you are. You are amazing, I wish I would be half as methodic as you are. I am happy to be your big brother and I will always be there when you need me. You can do anything that you propose, and I know that all your projects will get to a good port. Enano, I'm not sure how to tell you how happy I am for being your older bro. I'm proud of you, for everything that you have done and I'm really happy to share with you my love for science. It will not be easy, but you are one of the smartest people I've ever met. You can accomplish anything as long as you keep trying. Always remember that I'm here for you, and I wish you nothing but the best in the adventures you will have from now on. Being them in science, being them in life, being them in Chile or wherever the tide takes you. I am and will be proud which wherever you choose :)

This thesis was financially supported through the fellowship "Becas Doctorales Institucionales ULS", granted by the "Vicerrectoría de Investigación y Postgrado de la Universidad de La Serena". Additionally, I want to thank the financial support from the Max Planck Society through a Partner Group grant and the European Union's Horizon 2020 Research and Innovation Programme under the Marie Skłodowska-Curie grant agreement number 734374-Project acronym: LACEGAL, which allowed me to travel to the Max Planck Institute and Durham University to develop part of these projects. Finally, I would like to acknowledge financial support from CONICYT through the project FONDECYT Regular No. 1211370.